Establishing Advanced MAS NMR Methods to Investigate Protonation Dynamics in Proteins

Inaugural-Dissertation
to obtain the academic degree
Doctor rerum naturalium (Dr. rer. nat.)

submitted to the Department of Biology, Chemistry and Pharmacy
of Freie Universität Berlin

by
Daniel Friedrich *né* Stöppler
from Filderstadt

2018

The presented research was performed from May 2014 – May 2018 in the 'Department of NMR-supported Structural Biology' under the supervision of Prof. Dr. Hartmut Oschkinat at the *Leibniz-Forschungsinstitut für Molekulare Pharmakologie* (FMP) in Berlin, Germany.

1st reviewer: Prof. Dr. Hartmut Oschkinat
2nd reviewer: Prof. Dr. Bernd Reif

Thesis Defense: December 3, 2018

“Life is travelling to the edge of knowledge, then a leap taken.”

David Herbert Lawrence

ACKNOWLEDGEMENTS

It would not have been possible to accomplish this work without the excellent support of many people. I enjoyed an inspiring scientific environment and I was privileged to collaborate with a large number of interesting and amazing people who made this work possible. It was a great time and interesting experience, and I learned unbelievably many things. I wish all my best to everyone who accompanied me.
In particular, I would like to thank my advisor and mentor Hartmut Oschkinat for his truly outstanding support. I thank Bernd Reif for reviewing this thesis, and Barth-Jan van Rossum and Wing Ying Chow for proof-reading it and teaching me a lot. I also thank Andy Nieuwkoop and Trent Franks, you taught me so much at the spectrometers, and Matthias Herrera Glomm (Hiller), you helped me a lot with all the technical things. And a very big thank you to Anne Diehl, Kristina Rehbein, Natalja Erdmann and Dagmar Michl for preparing many samples. And of course, thanks to Michel-Andreas Geiger and Joren Retel, it was great to get through it together.

Many thanks to all members of the SFB1078 and to all my mentors, collaborators and colleagues, especially to:

Alex Macpherson, Alexandra Chylla, Andrea Steuer, Anil Jagtap, Anja Böckmann, Anja Voreck, Anup Chowdhury, Arndt Wallmann, Beat Meier, Brigitte Schlegel, Chen Song, Christina Lang, Christina Schnick, David Fox III, Eavan Donovan, Elena Matei, Everton d'Andrea, Florian Brünig, Florian Lindemann, Florian Seiter, Frank Eisenmenger, Heidi Petschick, Holger Dau, Ingo Breng, Jeremias Zill, Johanna Münkemer, Jon Hughes, Jonas Protze, Jörg Matysik, Katharina Märker, Katja Stehfest, Kelsey Collier, Kerstin Wagner, Kürşad Turgay, Lilo Handel, Linda Ball, Linus Hopf, Lisa Gerland, Madhu Nagaraj, Mahsheed Sohrabi, Maila Reh, Marcella Orwick-Rydmark, Margrit Michalsky, Maria-Andrea Mroginski, Martin Ballaschk, Martina Leidert, Max Zinke, Miguel Arbesú Andrés, Monika Beerbaum, Nils Cremer, Nestor Kamdem, Nils Trieloff, Pascal Fricke, Peter Hegemann, Peter Hildebrandt, Peter Schmieder, Roland R. Netz, Sara Bruun, Shakeel Ahmad Shahid, Simon Erlendsson, Snorri Sigurdsson, Stephanie Wendt, Susanne Smith-Penzel, Thi Bich Thao Nguyen and Ümit Akbey. Thank you all so much!

And finally – with all my heart – I thank Dhana, this work would not have been imaginable without you, really not at all. I'm very much looking forward to our future, there is a great time ahead of us!

SUMMARY

Structural biology provides fundamental insight into protein function. One underlying mechanistic principle of protein function may be protonation dynamics, that is structural alterations related to changes in protonation states. The interplay between proton exchange processes and biomacromolecular structure, i.e. function, needs to be further established in life sciences. Protonation dynamics can be studied by different theoretical, biophysical and biochemical approaches. Nuclear magnetic resonance (NMR) spectroscopy is a powerful method to detect protons directly and to elucidate structural features related to changes in protonation states. With this work, two advanced solid-state magic angle spinning (MAS) NMR spectroscopy approaches, proton detection and dynamic nuclear polarization (DNP), are applied to study protonation dynamics in large proteins and membrane proteins.

Proton detection combined with fast MAS is employed to obtain spatial information on hydrogen atoms. A case study is presented, proposing a proton-detected solid-state MAS NMR experiment that enables the observation of hydrogen bonds in a model protein, a microcrystalline preparation of the chicken α-spectrin SH3 domain. It is used to elucidate hydrogen bond patterns in secondary structure elements; in a modified version, it may be applied to detect such patterns in amino acid side chains. In a pilot study, chemical exchange of protons is investigated with the light-driven proton pump bacteriorhodopsin as an example. Proton relocation was observed inside the channel at three functionally-relevant key amino acid side chains, which are involved in the proton transport pathway of bacteriorhodopsin. We detect a protonated form of R82 suggesting its involvement in the proton pumping process, and we notice proton delocalization between the carboxylic moieties of both D85 and D96 and water. Furthermore, a study on the soluble extra-cellular domain of the neonatal Fc receptor is presented as a methodologically oriented application of fast MAS NMR. This receptor interacts with Immunoglobulin G in a pH-dependent manner and thus via changes in protonatable amino acid side chains. Hence, protonation dynamics is fundamentally involved in this protein-protein interaction. The study aims to develop a small molecule and characterize its binding structurally to explore possibilities for inhibition of the interaction with Immunoglobulin G. The application of NMR at 100 kHz MAS to the sedimented, fully protonated receptor was crucial to obtain

chemical shift perturbations upon binding of the identified ligand as a prerequisite for optimization of the compound. This study introduces an innovative approach to investigate soluble proteins expressed in mammalian cells by proton-detected MAS NMR without the need for deuteration, making a variety of protein classes accessible to NMR studies.

As demonstrated in this thesis, structural features related to protonation dynamics can be difficult to observe by conventional NMR techniques due to low sensitivity. Furthermore, halting exchange processes by freezing samples may facilitate protonation dynamics investigations. The DNP technology is therefore further developed in two studies using proline standard samples and the SH3 domain. We present a high-temperature approach employing deuterated biradicals and introduce a novel highly water-soluble biradical, called bcTol. The use of deuterated TOTAPOL isotopologues resulted in a 15-fold increase in sensitivity at 200 K, thereby facilitating the acquisition of multidimensional spectra with improved resolution at this temperature. The new biradical bcTol is demonstrated to be a promising and efficient polarizing agent in biomolecular investigations, easy-to-handle and showing an improved performance compared to other known biradicals. These methodological achievements enabled studies of protonation dynamics in complex protein systems. In this context, structure-related features in the chromophores of channelrhodopsin and the phytochrome photoreceptor Cph1 are investigated via the utilization of DNP. The enhancement in sensitivity helped to elucidate the retinal configuration to be all-*trans* in dark-adapted channelrhodopsin, which is an important feature of the photocycle. It allowed us to discuss the chromophore structural changes enabling proton conductance across the membrane. In Cph1, the application of DNP was critical to obtain chemical shift assignments of the phycocyanobilin chromophore nitrogens. This provided insight into the water molecule distribution in the chromophore binding pocket and the localization of the positive charge in phycocyanobilin. These findings help to understand the chromophore changes and possible proton exchange pathways during molecular action of phytochrome photoreceptors.

ZUSAMMENFASSUNG

Die Strukturbiologie ermöglicht grundlegende Einblicke in die Funktion von Proteinen. Ein grundsätzliches mechanistisches Prinzip für die Regulierung von Proteinfunktion könnte die Protonierungsdynamik sein. Diese umfasst strukturelle Variationen in Proteinen aufgrund von Änderungen in Protonierungszuständen. Das Zusammenspiel von Protonenaustauschprozessen und biomakromolekularer Struktur, das heißt Funktion, muss in den Lebenswissenschaften noch weiter verstanden und etabliert werden. Protonierungsdynamik kann mit verschiedenen theoretischen, biophysikalischen und biochemischen Ansätzen untersucht werden. Die Kernspinresonanzspektroskopie (*nuclear magnetic resonance*, NMR) ist eine geeignete Methode um Protonen direkt zu detektieren und um strukturelle Eigenschaften, die im Zusammenhang mit Änderungen in Protonierungszuständen stehen, zu untersuchen. Um solche Studien zu ermöglichen, werden in dieser Arbeit zwei moderne Methoden der Festkörper-*magic angle spinning* (MAS) NMR Spektroskopie, die Dynamische Kernpolarisation (*dynamic nuclear polarization*, DNP) und die Protonendetektion, genutzt. Beide Methoden werden in Untersuchungen von Aspekten der Protonierungsdynamik in großen Proteinen und in Membranproteinen angewendet.

Zunächst wird die Protonendetektion in Kombination mit schnellem MAS zur Gewinnung räumlicher Information über Wasserstoffatome verwendet. In einer methodischen Studie wird ein protonendetektiertes Festkörper-MAS NMR Experiment vorgestellt, mit dessen Hilfe Wasserstoffbrücken in einem Modellprotein, der mikrokristallinen α-spectrin SH3 Domäne, detektiert werden können. Es wird zur Analyse von Wasserstoffbrückenmustern in Sekundärstrukturelementen verwendet. In einer modifizierten Version kann es zukünftig auch für die Untersuchung solcher Muster zwischen Aminosäureseitenketten eingesetzt werden. In einer weiteren Studie wird der chemische Austausch von Protonen in der lichtgetriebenen Protonenpumpe Bakteriorhodopsin untersucht. Dadurch konnte die Verteilung von Protonen an drei im Kanal lokalisierten funktional relevanten Aminosäureseitenketten, die an dem Protonentransport von Bakteriorhodopsin involviert sind, detektiert werden. Eine protonierte Form von R82 konnte gemessen werden, was eine Beteiligung von R82 in dem Protonentransportprozess nahelegt, und eine Protonendelokalisierung zwischen

den Carboxylgruppen von D85 und D96 mit Wasser konnte gezeigt werden. Darüber hinaus wird eine Studie der löslichen extrazellulären Domäne des neonatalen Fc Rezeptors als eine methodisch orientierte Anwendung von schnellem MAS vorgestellt. Dieser Rezeptor wechselwirkt mit Immunoglobulin G pH-abhängig über protonierbare Aminosäureseitenketten. Folglich ist die Protonierungsdynamik grundlegend an dieser Protein-Protein-Wechselwirkung beteiligt. Das Ziel dieser Studie ist die Entwicklung eines Moleküls und die strukturelle Charakterisierung seiner Bindung an den Rezeptor um Möglichkeiten für die Inhibierung der Wechselwirkung mit Immunoglobulin G auszuloten. Die Verwendung von NMR bei 100 kHz MAS war entscheidend um Veränderungen von chemischen Verschiebungen durch Ligandenbindung des sedimentierten, vollständig protonierten Rezeptors zu messen. Die beobachteten Veränderungen deuten auf die Möglichkeit hin, nach weiterer Optimierung des Liganden eine allosterische Inhibition zu erzielen. Diese Studie stellt einen innovativen Ansatz vor lösliche Proteine, die in Säugetierzellen hergestellt werden müssen und nicht deuteriert werden können, mit protonendetekierter MAS NMR zu untersuchen. Dies eröffnet neue Möglichkeiten eine Vielzahl von verschiedenen Proteinklassen mit NMR zu messen.

Als weiteren experimentellen Ansatz wird DNP zur Sensitivitätssteigerung in Festkörper-NMR genutzt. Wie in dieser Arbeit gezeigt wird kann es aufgrund von geringer Sensitivität schwierig sein, strukturelle Merkmale von Protonierungsdynamik mit konventionellen NMR Methoden zu untersuchen. Um zukünftige NMR Studien von Protonierungsdynamik zu ermöglichen, wird DNP in dieser Arbeit mit Prolinstandardproben und der SH3 Domäne weiterentwickelt. Ein experimenteller Ansatz zur Messung bei höheren Temperaturen mit deuterierten Biradikalen und ein neues hochwasserlösliches Biradikal, genannt bcTol, werden vorgestellt. Der Einsatz deuterierter TOTAPOL Isotopologe resultierte in einer 15-fachen erhöhten Sensitivität bei 200 K im Vergleich zu konventionellen solid-state MAS NMR Messungen, was die Aufnahme von multidimensionalen Spektren mit verbesserter Auflösung bei dieser Temperatur ermöglichte. Wie gezeigt werden kann, ist das neue Biradikal bcTol ein vielversprechendes und effizientes Polarisierungsmittel für biomolekulare Studien, da es einfach in der Handhabung ist und eine verbesserte Leistung im Vergleich zu anderen bekannten Biradikalen aufweist. Wie in zwei Anwendungen gezeigt wird, ermöglichen diese methodischen Ergebnisse Studien von Protonierungsdynamik in

komplexen Proteinen. DNP-verstärkte Festkörper-MAS NMR wird zur Untersuchung von strukturellen Merkmalen der Protonierungsdynamik in den Chromophoren von Channelrhodopsin und dem Phytochrom-Photorezeptor Cph1 verwendet. Die Anwendung von DNP war zur Bestimmung der all-*trans* Retinalkonfiguration, einem wichtigen Merkmal des Photozyklus, in dunkel-adaptiertem Channelrhodopsin entscheidend. Dies erlaubte Schlussfolgerungen auf die strukturellen Änderungen, die die Protonenleitfähigkeit über die Membran ermöglichen. In Cph1, war die Verwendung von DNP mit bcTol entscheidend um Zuordnungen von chemischen Verschiebungen der Phycocyanobilin Chromophor-Stickstoffe durchführen zu können. Dies lieferte Einblicke in die Verteilung von Wassermolekülen in der Chromophorbindetasche und in die Lokalisierung der positiven Ladung in Phycocyanobilin. Die Ergebnisse fördern ein besseres Verständnis der strukturellen Änderungen des Chromophores und möglicher Protonenaustauschprozesse während des Photozyklus von Phytochrom-Photorezeptoren.

LIST OF MANUSCRIPTS ENCLOSED IN THIS THESIS

CHAPTER 2

Andrew J. Nieuwkoop,[#] **Daniel Friedrich**,[#] and Hartmut Oschkinat:
'Exploring Long-range Contacts and Hydrogen Bonds in Proteins by Proton-detected Solid-state Magic-Angle-Spinning NMR', *manuscript in preparation*
[#] ***Equal contribution***

CHAPTER 3

Daniel Friedrich, Andrew J. Nieuwkoop, Florian Brünig, Roland R. Netz, Peter Hegemann, and Hartmut Oschkinat:
'Direct Observation of Proton Exchange in a Proton Pump', *manuscript in preparation*

CHAPTER 4

Daniel Stöppler,[#] Alex Macpherson,[#] Susanne Smith-Penzel, Nicolas Basse, Fabien Lecomte, Hervé Deboves, Richard D. Taylor, Tim Norman, John Porter, Lorna C. Waters, Marta Westwood, Ben Cossins, Katharine Cain, James White, Robert Griffin, Christine Prosser, Sebastian Kelm, Amy H. Sullivan, David Fox III, Mark D. Carr, Alistair Henry, Richard Taylor, Beat H. Meier, Hartmut Oschkinat, and Alastair Lawson:
'Insight into Small Molecule Binding to the Neonatal Fc Receptor by X-ray Crystallography and 100 kHz Magic-Angle-Spinning NMR', *PLOS Biology*, 2018, (16):5, e2006192
[#] ***Equal contribution***

CHAPTER 5

Michel-Andreas Geiger,[#] Marcella Orwick-Rydmark,[#] Katharina Märker, W. Trent Franks, Dmitry Akhmetzyanov, **Daniel Stöppler**, Maximilian Zinke, Edgar Specker, Marc Nazaré, Anne Diehl, Barth-Jan van Rossum, Fabien Aussenac, Thomas Prisner, Ümit Akbey, and Hartmut Oschkinat:

'Temperature dependence of cross-effect dynamic nuclear polarization in rotating solids: advantages of elevated temperatures', *Physical Chemistry Chemical Physics*, 2016, 18, pp 30696–30704

[#] ***Equal contribution***

CHAPTER 6

Sara Bruun,[#] **Daniel Stoeppler**,[#] Anke Keidel, Uwe Kuhlmann, Meike Luck, Anne Diehl, Michel-Andreas Geiger, David Woodmansee, Dirk Trauner, Peter Hegemann, Hartmut Oschkinat, Peter Hildebrandt, and Katja Stehfest:

'Light−Dark Adaptation of Channelrhodopsin Involves Photoconversion between the all-*trans* and 13-*cis* Retinal Isomers', *Biochemistry*, 2015, 54 (35), pp 5389–5400

[#] ***Equal contribution***

CHAPTER 7

Anil P. Jagtap, Michel-Andreas Geiger, **Daniel Stöppler**, Marcella Orwick-Rydmark, Hartmut Oschkinat, and Snorri Th. Sigurdsson:

'bcTol: a highly water-soluble biradical for efficient dynamic nuclear polarization of biomolecules', *Chemical Communications*, 2016, 52, pp 7020–7023

CHAPTER 8

Daniel Stöppler, Chen Song, Barth-Jan van Rossum, Michel-Andreas Geiger, Christina Lang, Maria-Andrea Mroginski, Anil P. Jagtap, Snorri Th. Sigurdsson, Jörg Matysik, Jon Hughes, and Hartmut Oschkinat:

'Dynamic Nuclear Polarization Provides New Insights into Chromophore Structure in Phytochrome Photoreceptors', *Angewandte Chemie International Edition*, 2016, 55 (52), pp 16017–16020

TABLE OF CONTENTS

ACKNOWLEDGEMENTS IV

SUMMARY VI

ZUSAMMENFASSUNG VIII

LIST OF MANUSCRIPTS ENCLOSED IN THIS THESIS XI

TABLE OF CONTENTS XIII

LIST OF FIGURES XV

LIST OF ABBREVIATIONS XVI

1. GENERAL INTRODUCTION 1

1.1 Structural Biology and Protonation Dynamics in Protein Function 2

1.2 Advanced Solid-state NMR: Dynamic Nuclear Polarization and Proton Detection using fast Magic Angle Spinning 11

1.3 Scope of the Thesis 29

2. EXPLORING LONG-RANGE CONTACTS AND HYDROGEN BONDS IN PROTEINS BY PROTON-DETECTED SOLID-STATE MAGIC-ANGLE-SPINNING NMR 31

2.1 Synopsis 32

2.2 Personal contribution 33

2.3 Manuscript in Preparation 33

3. DIRECT OBSERVATION OF PROTON EXCHANGE IN A PROTON PUMP 53

3.1 Synopsis 54

3.2 Personal contribution 55

3.3 Manuscript in Preparation 55

4. INSIGHT INTO SMALL MOLECULE BINDING TO THE NEONATAL FC RECEPTOR BY X-RAY CRYSTALLOGRAPHY AND 100 KHZ MAGIC-ANGLE-SPINNING NMR 85

4.1 Synopsis 87

4.2 Personal contribution 88

4.3 Original Publication 89

5. Temperature Dependence of Cross-Effect Dynamic Nuclear Polarization in Rotating Solids: Advantages of Elevated Temperatures 117
5.1 Synopsis 118
5.2 Personal contribution 119
5.3 Original Publication and Supplementary Information 119

6. Light–Dark Adaptation of Channelrhodopsin Involves Photoconversion between the all-trans and 13-cis Retinal Isomers 155
6.1 Synopsis 156
6.2 Personal contribution 157
6.3 Original Publication and Supplementary Information 157

7. bcTol: A Highly Water-Soluble Biradical for Efficient Dynamic Nuclear Polarization of Biomolecules 179
7.1 Synopsis 180
7.2 Personal contribution 181
7.3 Original Publication and Supplementary Information 181

8. Dynamic Nuclear Polarization Provides New Insights into Chromophore Structure in Phytochrome Photoreceptors 195
8.1 Synopsis 196
8.2 Personal contribution 197
8.3 Original Publication and Supplementary Information 197

9. General Discussion and Conclusion 213
9.1 Discussion and Conclusion 214
9.2 Future Perspectives 219

Bibliography 224
Curriculum Vitae 242
List of Publications 246
Declaration 248

LIST OF FIGURES

Figure 1.1. Classic examples of protonation dynamics in proteins 5

Figure 1.2. The concept of magic angle spinning (MAS) 17

Figure 1.3. The principle of cross polarization (CP) 18

Figure 1.4. DNP-enhanced solid-state MAS NMR 20

Figure 1.5. Proton-detected solid-state NMR profits from deuteration of proteins and high MAS frequencies using small rotors 23

Figure 1.6. Magnetization transfer schemes of two- and three-dimensional solid-state MAS NMR spectra for resonance assignments 26

List of Abbreviations

Å	Ångström
ATP	adenosine triphosphate
BR	bacteriorhodopsin
C1C2	channelrhodopsin chimera of channelrhodopsins 1 and 2
ChR	channelrhodopsin
CP	cross polarization
Cph1Δ2	photosensory module of cyanobacterial phytochrome 1
cryo-EM	cryogenic electron microscopy
DARR	dipolar assisted rotational resonance
DNA	deoxyribonucleic acid
DNP	dynamic nuclear polarization
EPR	electron paramagnetic resonance spectroscopy
FcRn	neonatal Fc receptor
$FcRn_{ECD}$	extra-cellular domain of the neonatal Fc receptor
FTIR	Fourier-transform infrared spectroscopy
GTP	guanosine triphosphate
HSA	human serum albumin
IgG	Immunoglobulin G
MAS	magic angle spinning
MD	molecular dynamics
NMR	nuclear magnetic resonance spectroscopy
PDB	protein data bank, *rcsb.org*
PDSD	proton driven spin diffusion
PCB	phycocyanobilin
PTM	post-translational modification
RSB	retinal Schiff base
RNA	ribonucleic acid
RR	resonance Raman spectroscopy
S/N	signal-to-noise ratio

1

GENERAL INTRODUCTION

1.1 Structural Biology and Protonation Dynamics in Protein Function

Proteins are key to biological processes and cellular function. To understand the underlying principles, it is fundamental to analyze the structure and molecular action of proteins in detail. As an interdisciplinary science, structural biology not only provides insight into the architecture and function of proteins, but also allows the identification of possible therapeutic approaches. Established techniques such as x-ray crystallography, cryogenic electron microscopy (cryo-EM) and nuclear magnetic resonance (NMR) spectroscopy are applied for this purpose (1-7). Each of these methods has its own specific advantages, and in particular combined they can contribute in an integrative approach to gain detailed knowledge how biological macromolecules function (2, 5, 7). X-ray crystallography was used to solve the first three-dimensional structure of a protein (myoglobin in 1958, (6)), and more than 140,000 biological macromolecular structures have been deposited in the protein data bank up to now (PDB, *rcsb.org,* in May 2018). Despite considerable progress in structural biology in solving static structures of biomacromolecules at atomic resolution, it is clear that their structural plasticity and dynamic aspects are crucial for a complete understanding of macromolecular function in biology (7, 8-11). Dynamic properties of proteins have been underrated in life sciences as at least equally important as structure itself. These are critical in small proteins, large macromolecular assemblies, populations of different physical phases, intrinsically disordered proteins, and conformational heterogeneity leading to invisible, but functional states (8, 10, 12-17). Most importantly, it is essential to further develop approaches towards biophysical studies with atomic resolution in native or native-like conditions, in the best case employing the cellular environment itself (18, 19).

Even though its focus is predominantly on biomolecular structure, the field of structural biology made fundamental contributions to understand biomolecular function in life sciences (20-25). These contributions include, for example, insights into protein-ligand interactions, which have been studied extensively for many decades. This yielded a detailed characterization of substrate binding and the induced-fit or key-and-lock mechanisms (26-29). Similarly, protein-protein interactions and the interplay of proteins with other biological macromolecules such as DNA, RNA and lipids have been subject to intense structural biology investigations (30-34). These

studies enabled understanding of important cellular processes, e.g. protein biosynthesis and signaling events through cytosolic and membrane proteins. Also the process of protein folding is studied by structural biology methods (35). New insights in how chemical energy is used to enable protein action help to understand regulation of protein function; a textbook example for such a process is actin and myosin, acting as molecular motors (36). As another example for regulation of biomolecular function studied by structural biology, post-translational modifications (PTMs) of proteins should be mentioned, reviewed for example by Prabakaran et al. (37). In many cases, PTMs provide a basis for cellular function through proteins, especially in signaling pathways and subcellular organization.

The dynamic behavior of protons may be one underlying mechanistic principle of protein function. In proteins, functionally-relevant protons usually participate in hydrogen bonds. However, a variety of non-covalent interactions contributes to the stability of the protein structure (38). These involve groups with both polar/charged and non-polar character. Non-polar interactions, on the one hand, include for example Van der Waals forces – a subset of electrostatic interactions –, π-effects and the hydrophobic effect. On the other hand, interactions between polar/charged groups comprise for example the attraction of ions with full permanent charges of opposite signs, and hydrogen bonds. The latter are strong non-covalent interactions, and can be defined as the dipole-dipole attraction between a partially positive hydrogen atom and an electronegative, partially negative atom – in proteins usually oxygen, nitrogen or sulfur. Hydrogen bonds provide an important basis for secondary structure elements in proteins and interactions between amino acid side chains (39). In addition, they are often involved in binding of proteins to ligands or other biological macromolecules such as DNA or RNA. Hydrogen bonds are susceptible to being perturbed and can be considered as a flexible interaction that may contribute to structural plasticity and conformational heterogeneity. In biomolecules, they can vary in strength (usually 4 – 40 kcal/mol) and are about 2.2 – 4.0 Å in length (40). For a long time, it has been well known that the dynamic behavior of exchangeable hydrogen atoms is an important feature in many biological processes, e.g. in protein-protein and protein-ligand interactions, or in enzymatic reactions (41, 42). Therefore, the principle of protonation dynamics may be established as an additional basic concept of how protein function is mediated. The work presented in this thesis is embedded in the

Collaborative Research Center 1078 (CRC1078, *Sonderforschungsbereich* 1078) funded by the *Deutsche Forschungsgemeinschaft*, entitled 'Protonation Dynamics in Protein Function'. In this framework, this issue is addressed in an encompassing approach using different theoretical, biophysical and biochemical methods (*sfb1078.de*). The definition considers not only the spatio–temporal variation of exchangeable hydrogen atoms over many orders of magnitude in both time and space, but especially also structural consequences and features in proteins related to the dynamic behavior of protons.

According to the CRC1078, the definition of protonation dynamics includes

(1) the relocation of protons by less than 1 Å between neighboring groups (shift of a proton in a hydrogen bond),
(2) the delocalization of protons within clusters of water molecules and protonatable amino acid side chains, potentially involving Zundel ions,
(3) long-distance transfers along chains of water molecules (e.g. via the Grotthuss mechanism) and side chains, whereby motions have to be taken into account,
(4) rearrangements of extended hydrogen-bond networks in the protein interior and at the protein-water interface, including side chain rotations, changes in protonation states and position of water molecules,
(5) global conformational changes in the protein backbone, including rearrangements of secondary structure elements (e.g. β-sheet → α-helix),
(6) long-range electrostatic interactions between remote sites that may induce changes of protonation states.

Examples of these characteristic protonation dynamics features are given by the classic model proteins bacteriorhodopsin (BR), phytochrome photoreceptors and photosystem II (Figure 1.1.) (43-47).

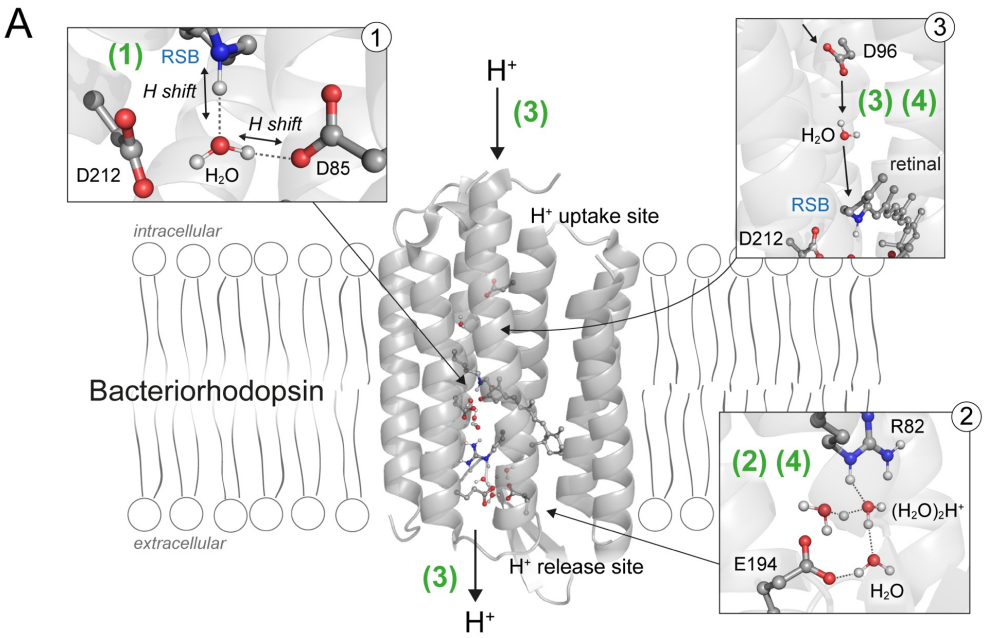
A
(1) RSB
H shift
H shift
D212
H2O
D85
1
H+
(3)
H+ uptake site
intracellular
Bacteriorhodopsin
extracellular
(3)
H+ release site
H+
3
D96
(3) (4)
H2O
retinal
RSB
D212
2
R82
(2) (4)
(H2O)2H+
E194
H2O

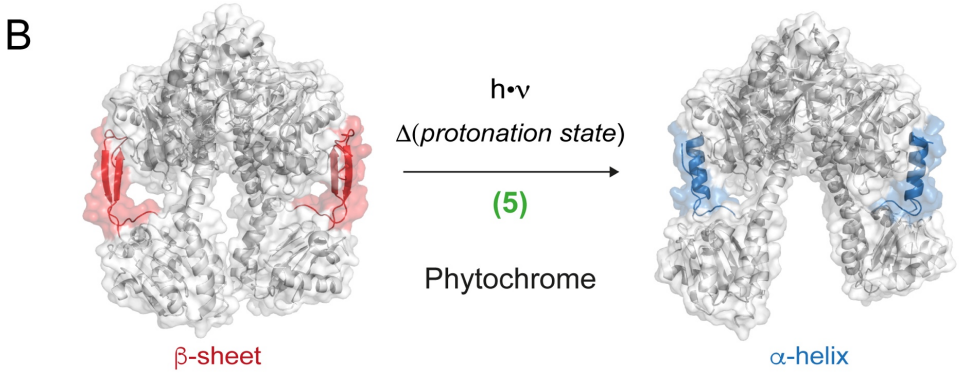
B
h•ν
Δ(protonation state)
(5)
Phytochrome
β-sheet
α-helix

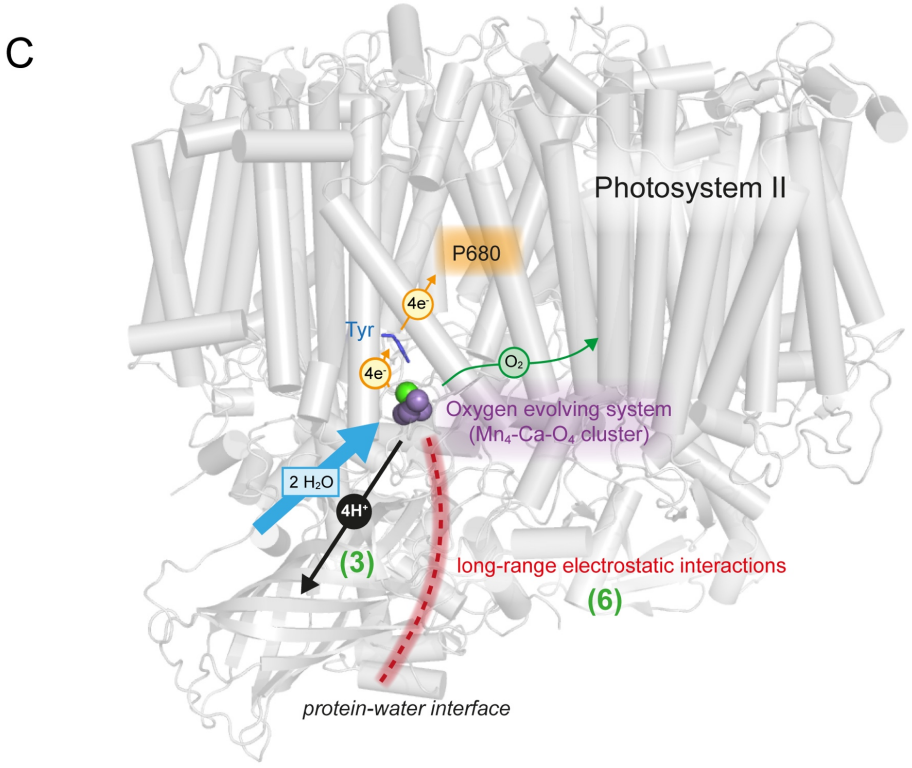
C
Photosystem II
P680
4e-
Tyr
4e-
O2
Oxygen evolving system
(Mn4-Ca-O4 cluster)
2 H2O
4H+
(3)
long-range electrostatic interactions
(6)
protein-water interface

Figure 1.1. Classic examples of protonation dynamics in proteins. *The defined features are indicated by green numbers.*
A *The proton pump bacteriorhodopsin (PDB code 1C3W) relocates protons across the cellular membrane. The protonation dynamics characteristics* ***(1)–(4)*** *can be illustrated in this process. The insets are described in the main text, RSB = retinal Schiff base.*
B *The bacteriophytochrome from Deinococcus radiodurans (PDB codes 4O0P and 4O01) shows a light-dependent change in protonation state between the photostates Pr (left) and Pfr (right) in its chromophore. This change is coupled to a rearrangement of a secondary structure element distant from the chromophore* ***(5)****.*
C *In photosystem II (PDB code 2AXT), both long-range electrostatic interactions* ***(6)*** *and long-distance proton transfer* ***(3)*** *are essential in water photolysis and oxygen evolution during photosynthesis.*

The archaeal light-driven proton pump BR has been studied for many decades, and it can be seen as the model system to investigate protonation dynamics since it exhibits several features of the basic definition above (illustrated in Figure 1.1.A) (48-59). The relocation of a hydrogen atom by less than 1 Å (definition **(1)**) – often referred to as a shifting proton within a hydrogen bond – can be seen for example in the hydrogen bonded cluster involving the protonated retinal Schiff base (RSB), the carboxylic moieties of D85 and D212, and a water molecule in BR dark-state (Figure 1.1.A *inset 1*) (60). In the so-called proton release group of BR, close to the extracellular proton release site, a hydrogen-bonded cluster of water molecules and the protonatable amino acid side chains R82 and E194 exists (definition **(2)**, Figure 1.1.A *inset 2*) (53, 61). In this cluster, an excess proton is delocalized leading to a partial existence of a Zundel ion ($(H_2O)_2H^+$) in the dark-state. In addition, this cluster represents an extended hydrogen bond network, which is rearranged during the BR photocycle and the proton transport process (definition **(4)**) (43, 61, 62). It is important to note that such a rearrangement is a dynamic mechanism, occupying different conformational states in a temporal order. Thus, it includes also side chain rotations of R82 and other amino acids, repositioning of water molecules and changes in the protonation states of the chemical moieties involved in the molecular action of BR (56, 63). During one photocycle, BR relocates one proton across the cellular membrane out of the

Halobacterium salinarum cell. This long-distance proton transfer (definition **(3)**), bridging more than 45 Å between the intra- and extracellular compartments, involves chains of water molecules, amino acid side chains and the RSB of the chromophore. It is only possible through conformational changes and repositioning of water molecules. Such a long-distance proton transfer can be specifically visualized at D96 close to the proton uptake site (Figure 1.1.A *inset 3*). During the BR photocycle, a transient water chain is formed between D96 and RSB, making a Grotthuss-like proton transfer across the respective distance of more than 10 Å possible (definitions **(3)** and **(4)**) (64). Again, a conformational change is required; in this case the isomerization of the retinal chromophore.

The bacteriophytochrome from *Deinococcus radiodurans* is a good example of a functional change in secondary structure (Figure 1.1.B, definition **(5)**). During the light-dependent Pr → Pfr transition, it has been shown by x-ray crystallography that the β-sheet (Pr-state) in the so-called tongue-region of phytochrome photoreceptors changes to an α-helical secondary structure (Pfr-state) (45). This rearrangement could be linked to a change in protonation state in the bilin chromophore as investigated by resonance Raman spectroscopy (RR), Fourier-transform infrared spectroscopy (FTIR), NMR spectroscopy and molecular dynamics (MD) simulations in several phytochromes (44, 46, 65-71). The underlying mechanism, however, still needs to be elucidated. The chromophore is indeed located in proximity to the tongue-region, but the change of protonation state in the chromophore must still be mediated through amino acid side chains providing an extended hydrogen bond network from the chromophore to the tongue-region.

Changes in protonation states may be induced by or coupled to remote electrostatic interactions (definition **(6)**); such an effect occurs in photosystem II (Figure 1.1.C) (72, 73). The coupling of protonation state changes to such interactions can control the pKa values of amino acid side chains and modulate dielectric dynamics at the protein-water interface. During photosynthesis, the long-distance transport of four protons from the oxygen evolving Mn_4-Ca-O_4 cluster is required (definition **(3)**) (74). This is coupled to the photolysis of four water molecules, yielding O_2 and four electrons per reaction. The latter induce long-range electrostatic interactions, leading to a modulation of protonation states at the protein-water interface. The electrons are further transported via a tyrosine residue to the P680 reaction center.

The central hypothesis of the CRC1078 is that protonation dynamics controls protein function. To establish the significance of protonation dynamics as a general and basic principle, further investigations are required. Through the work within the CRC1078 and by many other groups, key amino acids, sequences of events, proton pathways, water clusters, and domain movements related to protonation dynamics have been identified and characterized in different proteins (43, 44, 55, 63, 72, 75-83). In recent years, however, these studies have been mainly performed using photosensitive proteins as model systems. The main reason is that such proteins can be controlled by light during sample preparation or during biophysical and biochemical studies, hence they can be stalled in specific photointermediates or protonation states. This allows a precise elucidation of conformational intermediates through spectroscopic techniques such as FTIR, RR, electron paramagnetic resonance (EPR) and NMR spectroscopy, as well as gaining insights at atomic resolution by using x-ray crystallography and NMR spectroscopy.

The accessibility of defined and functional conformational sub-states in a protein that are stable during the time of an experiment facilitates studies of protonation dynamics. Therefore, focus has been on such intermediates of photosensitive proteins for identifying general principles of protonation dynamics. However, to establish the wide-spread importance of protonation dynamics as a fundamental key principle in protein function, it should be identified and characterized in an as broad spectrum of protein classes as possible. For instance, potentially interesting systems to investigate could be enzymes or proteins using chemical energy in the form of ATP or GTP. In such proteins, defined conformational states can be studied using non-hydrolyzable ATP- or GTP-analogues (84, 85). In particular, structural biology can contribute to their characterization (86). Large methodological progress has been achieved in the last decades in the three main methods used in this field.

When it comes to determining the three-dimensional structure of biological macromolecules, x-ray crystallography has been by far the most successful method accounting for about 89.5 % of all structures deposited in the PDB (in May 2018). The method has been developed into a very routine and robust procedure. As a prerequisite, it demands well-diffracting crystals of the molecule of interest. In addition to its success in the past, recent progress allows the determination of dynamic changes in conformation by time-resolved serial femtosecond crystallography using x-ray free

electron lasers (87). Due to such advances and its well-established availability, crystallography is expected to continue to have great impact in structural biology. In 2017, the number of structures solved per year by x-ray crystallography reached the 10,000 milestone for the first time (7).

In the past five years, substantial progress has been made in improving the resolution in electron microscopy. The use of single-particle cryo-techniques combined with optimized direct-electron detectors and the development of optimized drift compensation in images made structure determination with EM at atomic resolution possible for the first time (88, 89). In 2017, the Nobel Prize in Chemistry was awarded to Jacques Dubochet, Joachim Frank and Richard Henderson for 'developing cryo-electron microscopy for the high-resolution structure determination of biomolecules in solution' (90). The number of deposited structures in the PDB (more than 2,100 in May 2018) will likely grow rapidly, and their fraction of 1.5 % is expected to increase in the coming years. Already in October 2017, the number of structures deposited in the PDB per year by cryo-EM has surpassed the number of new deposits by NMR (7). Hence, cryo-EM is a promising technique that will most likely accelerate the process of structure determination. Together with x-ray crystallography, it will be the method of choice to solve biomolecular structures at atomic resolution in the future.

Solution-state NMR spectroscopy is responsible for more than 12,100 entries in the PDB (about 8.6 % in May 2018), but the number of deposited structures per year is not increasing anymore (7). However, NMR has a number of advantages for studies of structure-related questions in biomolecules. Firstly, it is a spectroscopic technique yielding information at atomic resolution. Secondly, it can be used as a quantitative method since individual spins are detected and it gives access to the chemical environment of the most important atoms that are present in biomolecules – ^{1}H, ^{13}C, ^{15}N, ^{17}O and ^{31}P (91). Thirdly, NMR spectroscopy is a non-destructive method and can be used in complex environments such as cellular extracts or directly inside the cell (18, 19, 92-94). Fourthly, and maybe most importantly, it allows the detection of dynamic properties of conformational changes and chemical reactions at physiologic conditions. This makes it a powerful method to study for example protein folding, enzymatic reactions, PTMs, exchange processes, intrinsically disordered regions or functional conformational states in biomolecules that are undetectable by other techniques (95-103). Advances in solution-state NMR spectroscopy such as methyl

labeling techniques or progress in hardware and in pulse sequences have extended the applicability to a wide range of biomolecules – covering proteins that range from small intrinsic disordered proteins to high molecular weight complexes (close to 1 MDa), as well as RNA, DNA and their complexes with proteins (8, 104-117). Solid-state magic angle spinning (MAS) NMR spectroscopy has recently been applied to solve protein structures as well, but so far, its contribution is moderately small – around 100 deposited in the PDB (less than 0.1 % in May 2018). The strength of MAS NMR may more be found in elucidation of detailed structural and dynamic features, mainly of its classic targets: membrane proteins, microcrystalline preparations, supramolecular assemblies and fibrillar states of proteins (118-122). In particular, it is useful to study proteins in its native environment, e.g. membrane proteins in lipid bilayers or native membranes. It is anticipated that in prospective structural biology ventures, an integrative approach making use of the diverse advantages of x-ray crystallography, cryo-EM and NMR spectroscopy will provide insight into biomolecular function that is required to understand the underlying complex mechanisms comprehensively.

In the past 15 years, two different advanced solid-state MAS NMR methods have experienced strong progress towards their application in structural biology: dynamic nuclear polarization (DNP) and proton detection combined with fast MAS (123-128). This thesis aims to apply these two advanced MAS NMR methods to investigate protonation dynamics in proteins. In the following sections, the theoretical background of the methods is introduced briefly.

1.2 Advanced Solid-state NMR: Dynamic Nuclear Polarization and Proton Detection using fast Magic Angle Spinning

The following chapter is focused on introducing the basic principles of NMR, DNP, proton detection and resonance assignments briefly. For a comprehensive and detailed description of the fundamentals of NMR spectroscopy, it is recommended to read some of the excellent available educational books, e.g. “Spin Dynamics: Basics of Nuclear Magnetic Resonance” by Malcolm H. Levitt, “Understanding NMR Spectroscopy” by James Keeler and “Introduction to Solid-state NMR Spectroscopy” by Melinda Duer (129-131). The basics of solid-state NMR are also reviewed comprehensively by David D. Laws, Hans-Marcus L. Bitter and Alexej Jerschow (132). In the following sections, a brief overview of the theoretical background of NMR should be sufficient to follow the investigations presented in this thesis.

Basics of nuclear magnetic resonance

Central in the study of molecules using NMR is the magnetic moment $\vec{\mu}$ of the atomic nucleus (1.1). Only those nuclei with odd mass and atomic numbers have a magnetic moment, which is related to the nuclear spin $\vec{S}$:

$$\vec{\mu} = g\frac{q}{2m}\vec{S} \qquad (1.1)$$

with the gyromagnetic factor g (Landé factor), the charge q and mass m of the nucleus. The relation between magnetic moment and spin is given by the gyromagnetic ratio (γ), which is specific for each type of nucleus (1.2):

$$\vec{\mu} = \gamma\vec{S} \qquad (1.2)$$

Only nuclei with a spin quantum number unequal to zero have the quantum mechanical property of a spin. In NMR, changes of overall orientation of an ensemble of spins (magnetization) are measured, therefore only such nuclei are detectable. The most

commonly used nuclei in biomolecular NMR are ^{1}H, ^{13}C, ^{15}N and ^{31}P. To circumvent the low natural abundance of ^{13}C and ^{15}N, samples need to be isotopically enriched. If an external magnetic field is applied, the magnetic moment adopts preferred orientations with discrete measurable energy and the spins populate two or more energy levels. This splitting of energy levels is known as the Zeeman effect. The number of possible energetic states depends on the spin quantum number I and can be calculated by $2I + 1$. Consequently, a nucleus with $I = ½$ has two different energetic states (Zeeman levels) called parallel (α-state) and antiparallel (β-state), which is usually visualized as their orientation with respect to the external magnetic field B_0. The α-state is of lower energy and the energy difference (ΔE) between the two states is proportional to the external magnetic field B_0 (1.3):

$$\Delta E = \frac{\gamma h B_0}{2\pi} \qquad (1.3)$$

with h being the Planck constant. The distribution of the occupation numbers (N) of the two different energy levels α and β is determined by calculating the Boltzmann distribution which applies in the case of thermodynamic equilibrium (1.4). It depends on the temperature (T) and the Boltzmann constant (k):

$$\frac{N_\beta}{N_\alpha} = e^{-\frac{\Delta E}{kT}} \qquad (1.4)$$

The difference in occupancy of two states in NMR is generally very small, for example it is only 0.01 % for ^{1}H at room temperature at a magnetic field strength of 20 T. As the signal intensity is proportional to the difference in occupation, in this case only one out of every 10,000 spins will give rise to an NMR-detectable signal. This is the main reason why NMR is a very insensitive method. A possibility to solve this problem is the application of hyperpolarization methods such as DNP that is further described below on page 19. The population difference between the two levels leads to a net magnetization along the external B_0-field, which is conventionally defined as parallel to the z-axis and the magnetization is termed longitudinal. In a magnetic field, the magnetization precesses with its Larmor frequency (υ) around the z-axis. The Larmor

frequency is proportional to B_0 and the gyromagnetic ratio; for example, it is 800 MHz for ^{1}H at 18.8 T. It is directly related to the energy difference between α- and β-state:

$$\Delta E = h\upsilon \qquad (1.5)$$

In an NMR experiment, the spin populations of the different levels follow a Boltzmann distribution in equilibrium, which can be perturbed by irradiation with an electromagnetic wave pulse at radiofrequency (RF). In case of magnetic resonance, the frequency of the RF pulse is very close to the Larmor frequency and the magnetic component of the wave interacts with the spins and the energy can be absorbed. This can lead to a change in distribution of the Zeeman levels and can result in the creation of transverse magnetization with appropriate length and strength of the RF irradiation. After the perturbation, the thermodynamic equilibrium of the spins in the magnetic field is restored, i.e. they return to the Boltzmann distribution through longitudinal relaxation. This process can be described with the relaxation time T_1 and limits how fast experiments can be repeated. The transversal relaxation is described with the relaxation time T_2 and limits the spectral resolution. The precessing transversal magnetization induces an oscillating current in the receiver coil surrounding the sample which is measured as the NMR signal, the so-called free induction decay (FID). The FID decreases over time due to the two relaxation processes.

In order to obtain a frequency spectrum from the time-dependent changes in the FID, the signal has to be Fourier-transformed. The FID contains information about the atomic nuclei and their chemical environment. The electrons surrounding the nucleus lead to a local shielding of the B_0-field. The result is a variability in frequencies of different spins, depending on the amount of shielding and hence on the specific chemical environment. This dispersion upon chemical environment leads to the chemical shift, in reference to a standard sample. The chemical shift is a very important and sensitive measurement parameter in NMR; spins that are less shielded will appear at larger chemical shifts, whereas nuclei that are more shielded have smaller chemical shifts in NMR spectra.

Even though the chemical shift leads to a dispersion of the NMR signals, in many cases severe spectral overlap can occur in biomolecular NMR. In order to achieve an improvement in spectral resolution allowing resonance assignments, Jean Jeener

proposed two-dimensional NMR at the AMPERE Summer School in Basko Polje, Yugoslavia in 1971; the experiment was then published in 1976 by Aue et al. (133). One-dimensional pulse sequences with so-called preparation and detection periods are extended to two dimensions with evolution and mixing periods. These are implemented in between the preparation and detection, whereby during evolution a variable time (t_1-period) is incremented. The variable length of the t_1-period probes the evolution of coherences of different frequencies. During mixing, spins are allowed to interact with each other. This means that, in addition to being modulated by their different frequencies, i.e. chemical shifts, an exchange of magnetization between different spins occurs, depending on the mixing scheme applied. This approach has been extended to three-, four- and even higher dimensional spectra.

The multidimensional NMR spectrum is obtained after Fourier-transformation of the direct and indirect dimensions. The direct dimension is obtained during the detection period by recording the FID, the indirect during the evolution period by incrementation. This spectrum contains both the information about the chemical shifts, and the exchange processes that are induced during the mixing period. The latter can be based both on chemical exchange of the nuclei involved and on exchange of magnetization between the respective spins. In both cases the interaction can be identified as cross peaks in the spectrum, which are signal intensities at defined positions in the multidimensional spectrum connecting the chemical shifts of the nuclei involved.

In solution-state NMR, the rotational correlation time (τ_c) of biomolecules must not exceed a certain upper limit, depending on the particular experiment performed. The reason is that the relaxation processes depend on τ_c, especially the transversal relaxation (T_2) resulting from variation in local magnetic fields. The main advantage of solid-state NMR is that the rotational correlation time that in solution-state NMR is dependent on the natural isotropic tumbling of the molecules is not the limiting factor. The relaxation processes rather rely on an external, collective motional averaging of the molecules introduced by the MAS. Therefore, solid-state MAS NMR is in principle not size-limited and can be applied to any biomolecule as long as sufficient narrow linewidths are achieved and spectral crowding can be handled, e.g. through appropriate labeling strategies. A prerequisite, however, is that the sample can be immobilized in some way. This may be achieved for example through micro-crystallization,

precipitation, embedding in lipid bilayers for membrane proteins, sedimentation, freezing of the sample, or fibril formation. It is very important to ensure native-like conditions of the sample, e.g. by monitoring the folding state during the experiment. The limited mobility of the molecule under investigation, even under MAS conditions, requires that anisotropic influences on spins have to be taken into account. The Hamiltonian describing the energies of a spin under solid-state conditions is:

$$\hat{H} = \hat{H}_Z + \hat{H}_{RF} + \hat{H}_{CS} + \hat{H}_D + \hat{H}_J + \hat{H}_Q \qquad (1.6)$$

The Hamiltonian $\hat{H}_Z$ describes the Zeeman interaction of the spin with the external magnetic field B_0, $\hat{H}_{RF}$ the interaction with the oscillating field B_1 when radiofrequency pulses are applied. The chemical shielding of the external magnetic field by electrons is taken into account by $\hat{H}_{CS}$. The electron density is generally not completely symmetrically distributed and the chemical shielding contains both an isotropic (δ_{iso}) and an anisotropic (δ_{aniso}, chemical shift anisotropy) part:

$$\hat{H}_{CS} = \gamma B_0 \hat{I}_Z \left[\delta_{iso} + \frac{1}{2}\delta_{aniso}(3\cos^2\theta - 1)\right] \qquad (1.7)$$

with $\hat{I}_Z$ describing the z-part of the spin operator of a nucleus with the gyromagnetic ratio γ and the angle θ between the vector of the anisotropic interaction and the magnetic field B_0. This consideration of $\hat{H}_{CS}$ is valid for an ellipsoidal distribution of the electron density and their localization along bond axes or non-bonding orbitals.
In addition to the chemical shift, spins interact with each other through dipolar couplings; the corresponding Hamiltonian $\hat{H}_D$ has an anisotropic part as well.

$$\hat{H}_D = \upsilon_D \left[\hat{I}_1 \hat{I}_2 - \left(\frac{(\hat{I}_2 r_{12})(\hat{I}_1 r_{12})}{r_{12}^2}\right)\right] \qquad (1.8)$$

It describes the coupling between the magnetic moments of two spins through space with its strength defined by the coupling constant υ_D. This constant depends on the permeability of vacuum (μ_0), the reduced Planck constant ($\hbar = \frac{h}{2\pi}$) and the gyromagnetic ratios γ_1 and γ_2 of the coupled spins, and the distance (r) between them:

$$\upsilon_{\mathrm{D}} = \frac{\mu_0 \gamma_1 \gamma_2 \hbar^2}{4\pi r_{12}^3} \qquad (1.9)$$

The distance dependency of the dipolar coupling therefore contains information about the three-dimensional structure of the molecules under investigation. It is around 21 kHz for the spins of directly bonded ^{1}H and ^{13}C atoms, and approximately 120 kHz for two ^{1}H spins with a distance of 1 Å from each other. Since the dipolar coupling only has an anisotropic part, its effect is averaged to zero by the rapid reorientation of molecules in solution and it is therefore not visible in solution-state NMR. If one uses the polar coordinates and the spin-raising- and spin-lowering-operators, $\hat{I}_+$ and $\hat{I}_-$, respectively, instead of the cartesian operator elements $\hat{I}_\mathrm{x}$ and $\hat{I}_\mathrm{y}$, the Hamiltonians for the homo- and heteronuclear dipolar coupling between spins *I* and *S* can be written as follows:

homo: $$\hat{H}_{\mathrm{D}}^{II} = \frac{\mu_0 \gamma_I^2 \hbar^2}{4\pi r_{II}^3} (3\cos^2\theta_{II} - 1)\left[\hat{I}_{\mathrm{z}1}\hat{I}_{\mathrm{z}2} - \frac{1}{4}\left(\hat{I}_{+1}\hat{I}_{-2} + \hat{I}_{-1}\hat{I}_{+2}\right)\right] \qquad (1.10)$$

hetero: $$\hat{H}_{\mathrm{D}}^{IS} = -\frac{\mu_0 \gamma_I \gamma_S \hbar^2}{4\pi r_{IS}^3} (3\cos^2\theta_{IS} - 1)\hat{I}_{\mathrm{z}}\hat{S}_{\mathrm{z}} \qquad (1.11)$$

with θ being the angle between a vector describing the dipolar coupling of the spins *I* and *S* and the B_0-field.

In addition to the dipolar coupling, the Hamiltonian $\hat{H}_{\mathrm{J}}$ for the scalar or J-coupling has to be considered in equation (1.6). It is mediated by the bonding electrons between nuclei. Its influence on NMR linewidths in solid-state NMR is rather small, because it is much weaker than the dipolar coupling. For example, the two spins in a ^{1}H–^{13}C bond have a scalar coupling constant of $^1J_{\mathrm{HC}}$ = 140 Hz. In solution-state NMR, the scalar coupling results in line splitting into multipletts. In solid-state NMR, this splitting is usually hidden by other line-broadening interactions, like dipolar couplings or heterogeneity in chemical environment. Therefore, the scalar coupling is often of minor importance in solid-state NMR.

Nuclei with spin quantum number $I > ½$ also exhibit quadrupolar interactions. They are described by the Hamiltonian $\hat{H}_{\mathrm{Q}}$ which also contains anisotropic parts; these interactions result from aspherical charge distributions in the atomic nucleus.

In summary, the Hamiltonian $\hat{H}$ of a spin contains anisotropic parts in the dipolar coupling and the chemical shift. In nuclei with quadrupolar moment, the anisotropy of the quadrupolar coupling has to be considered in addition. All anisotropic interactions have terms, which depend on $3\cos^2\theta - 1$ (see equations (1.7), (1.10) and (1.11)), whereby θ is the angle between a vector describing the anisotropic interaction and the external magnetic field B_0. In solution-state NMR, these anisotropic interactions are averaged out through the rotational tumbling motion of a molecule. Small molecules have a short rotational correlation time (fast tumbling motion), which leads to a more efficient averaging of these interactions. In solid-state, however, these anisotropic interactions remain and have to be eliminated experimentally. Therefore, the sample is filled into a cylindrical rotor that is spun around its z-axis at an angle of 54.74° with respect to the magnetic field B_0, which is called magic angle spinning (Figure 1.2.A). Generally, the angle θ (between the vector connecting the spins and the z-axis) of an arbitrary dipolar coupled spin pair does not match the magic angle. However, the vector rotates around a cone with an axis inclined at the magic angle with respect to the magnetic field because of the spinning. This leads to an oscillation of the strength of the anisotropic interaction around zero (Figure 1.2.B). In equations (1.7), (1.10) and (1.11), $3\cos^2\theta - 1$ becomes zero if θ is averaged to $\theta = 54.74°$, and all anisotropic interactions are minimized when the rotor rotates sufficiently fast (with frequency in the kHz regime) around the magic angle.

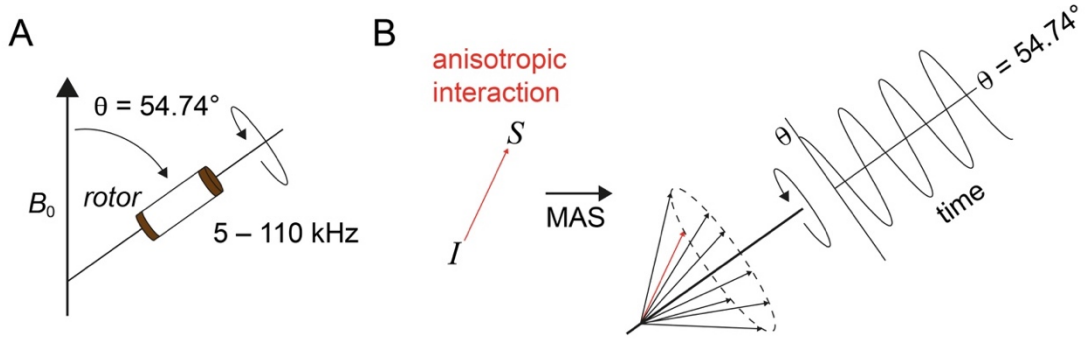

Figure 1.2. The concept of magic angle spinning (MAS).
A *The cylindrical rotor containing the sample is oriented at the magic angle of 54.74° with respect to the magnetic field B_0 and usually rotated between 5 – 110 kHz.*
B *Anisotropic interactions of arbitrary orientation between two spins (I and S) are minimized through MAS.*

In solid-state NMR, a very common technique to increase the sensitivity is cross polarization (CP) (134). During CP, the magnetization is transferred from a nucleus with high gyromagnetic ratio (e.g. ^{1}H) to a less sensitive nucleus (e.g. ^{13}C or ^{15}N) (Figure 1.3.A). This transfer of polarization is possible under fulfillment of the Hartmann-Hahn condition (Figure 1.3.B) (135). During a "normal" pulse, the RF-field is applied perpendicular to the orientation of the magnetization. In contrast, during CP, the RF-field is oriented parallel to the magnetization which is known as a spin-lock pulse. In order to fulfill the Hartmann-Hahn condition, the difference in RF strength (expressed in Hz) of the applied spin-lock-fields on the two types of nuclei has to be an integer multiple (with $n = 1$ or $n = 2$) of the MAS frequency. The polarization of the high-γ nucleus is transferred through the dipolar heteronuclear coupling to the low-γ nucleus resulting in an increase in sensitivity.

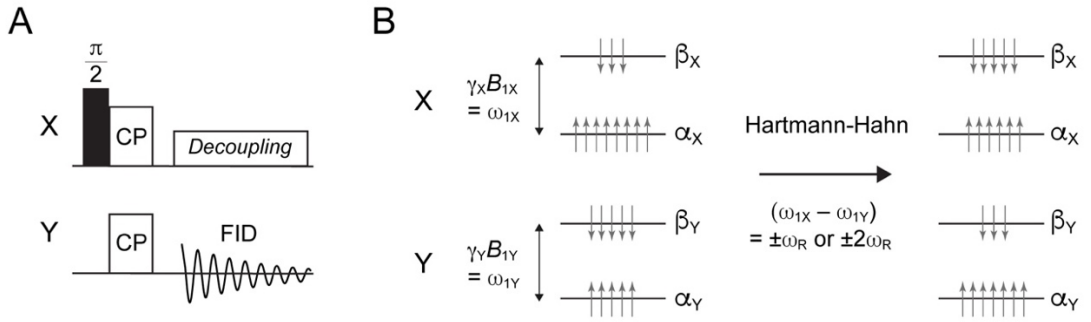

Figure 1.3. The principle of cross polarization (CP) between two different nuclei X and Y.

A *In a pulse sequence using CP, the magnetization is transferred between two nuclei by applying spin-lock fields for a certain contact time after initial excitation by a π/2-pulse. During detection of the FID, decoupling can be used in order to increase the spectral resolution through removal of couplings.*

B *Excitation of the X nuclei leads to spin polarization, whereas none exists in Y nuclei before the CP. The fulfillment of the Hartmann-Hahn matching condition during CP by applying the appropriate spin-lock-fields B_{1X} and B_{1Y} allows transfer of spin polarization to the Y nuclei. The difference in spin-lock-field frequencies ω_{1X} and ω_{1Y} has to be an integer multiple of the MAS frequency ω_R (with n = 1 or n = 2).*

In biomolecular NMR, the most commonly detected nuclei are ^{1}H, ^{13}C and ^{15}N. The latter two have a low natural abundance (^{13}C 1.1 %, ^{15}N 0.37 %); therefore, samples have to be isotopically enriched for biomolecular NMR experiments. For proteins, this can be achieved during recombinant protein expression using minimal media and ^{13}C-labeled carbon sources (e.g. ^{13}C-glucose or ^{13}C-methanol) and ^{15}N-labeled nitrogen sources (e.g. ^{15}N-ammonium sulfate), respectively. Alternatively, the use of selective labeling approaches can be helpful to reduce spectral crowding and increase the spectral resolution (120, 136-139). Selective amino acid labeling or the use of [1,3-^{13}C]- and [2-^{13}C]-glycerol may be useful to facilitate resonance assignments.

Dynamic nuclear polarization (DNP)

In the last decades, strong efforts have been undertaken to improve the sensitivity in biological solid-state MAS NMR by further developing DNP. In 1952, Albert Overhauser proposed the possibility to transfer the larger polarization of electrons to nuclear spins for hyperpolarization purposes, yielding an increase in sensitivity (140). Shortly after, Thomas Carver and Charles P. Slichter demonstrated experimentally that such an NMR signal enhancement can be achieved (141). In the context of biological applications, a fundamental breakthrough was the design and construction of a high-power generator of electromagnetic waves, a so-called gyrotron. For DNP-enhanced solid-state MAS NMR, this has been pioneered by the group of Robert G. Griffin at the Francis Bitter Magnet Laboratory, Massachusetts Institute of Technology (142-144). In 2009, the first gyrotron set-ups for biological DNP-enhanced solid-state MAS NMR became commercially available (Figure 1.4.A). This lead to the emergence of specialized and promising investigations within the NMR field intended to further developing this method and applying it to questions in structural biology (145-151). It may be even applicable to NMR studies at natural isotopic abundance (152). A detailed description of the history and theoretical background of DNP is reviewed for example by Charles P. Slichter or by Thankamony et al. (140, 153).

There are different mechanisms of microwave-driven DNP: the solid-effect (SE), the Overhauser effect, thermal mixing and the cross-effect (CE). The latter is applied in this thesis; this mechanism requires two unpaired electrons that are used as the source

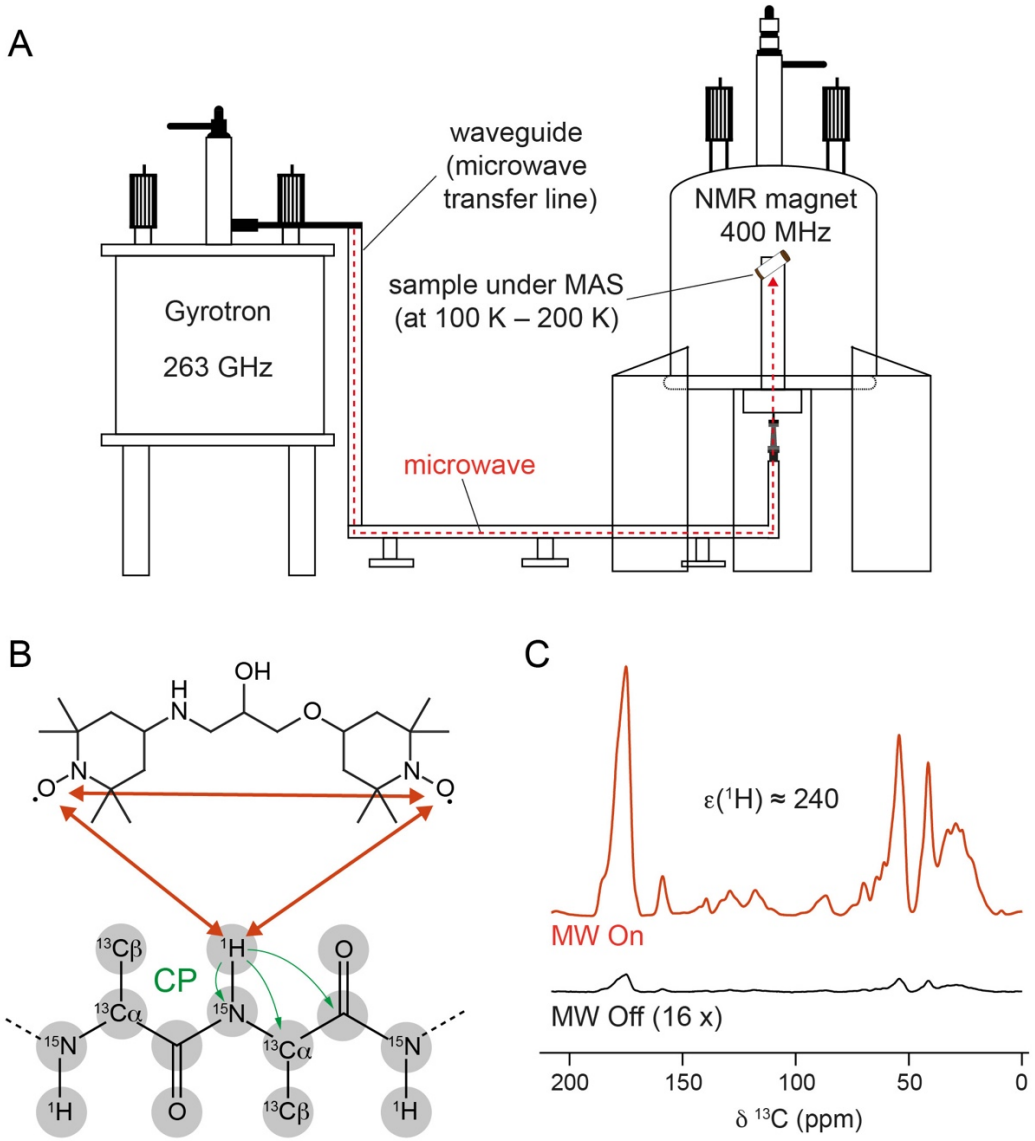

Figure 1.4. DNP-enhanced solid-state MAS NMR.

A *The experimental set-up comprises a gyrotron, a waveguide and an NMR spectrometer. At a magnetic field of 9.4 T (400 MHz), the corresponding gyrotron frequency is 263 GHz. The sample can be cooled during MAS in a range of 100 K – 290 K by a cooling cabinet with a low-temperature-MAS unit supplied with liquid N_2 (not shown).*

B *A biradical with two unpaired, dipolar coupled electrons can be used to hyperpolarize nuclear spins under microwave irradiation using the cross-effect. The high polarization can be further transferred from ^{1}H spins to heteronuclei using cross polarization (CP).*

C *The enhancement effect ($\varepsilon(^{1}H) \approx 240$) on ^{1}H polarization is measured by comparing one-dimensional ^{1}H-^{13}C CP spectra without (MW Off, black, scaled by a factor of 16) and with (MW On, red) microwave irradiation recorded at 100 K on a standard protein using the biradical bcTol (see chapter 7).*

of high polarization, and one nuclear spin (Figure 1.4.B). Therefore, the sample is doped with a stable biradical with two free electrons. Different versions of such molecules have been designed, e.g. TOTAPOL or AMUPol, and they are further developed to optimize the DNP efficiency (154, 155). The cross effect occurs when the two electrons are dipolar coupled to each other, and their resonance frequency is separated by the Larmor frequency of the nuclear spin. Under MAS and continuous microwave irradiation, the polarization is transferred from the electron spins to the nuclear spin when the Double or Zero Quantum transitions in this three-spin system are excited. This happens in a rotor-period dependent manner and can lead to a theoretical enhancement (ε) of the NMR signal of about 660 for ^{1}H resulting in a reduction of measurement time by a factor of 660^2 = 435,600 (153). In practice, the enhancement factors are usually in the order of 10 – 250 for protein samples in DNP solid-state MAS NMR (Figure 1.4.C), see also chapters 5, 6, 7 and 8 (76, 156). This means that a NMR spectrum that would require a measurement time of one week (= 168 hours) using standard solid-state MAS NMR, can be acquired within ~15 s with DNP (ε = 200). Consequently, DNP has a great potential for acquiring NMR spectra of systems with otherwise low sensitivity, especially when using very low sample amounts. It is important to keep in mind that depolarization can lead to a decrease of overall gain in sensitivity, e.g. through effects of paramagnetic relaxation enhancement (PRE) or MAS (153, 157, 158).

The advantage of signal enhancement, however, comes at a price. The main challenge in biological DNP-enhanced solid-state MAS NMR is a severe reduction in spectral resolution, caused by both homogeneous and inhomogeneous line broadening (153, 159). In DNP, the efficiency of the enhancement depends on the temperature – the lower the temperature, the higher the gain in sensitivity (153, 160). The strongest effect on the linewidths is due to the low experimental temperatures leading to heterogeneously and inhomogeneously broadened lines (161). At the commonly used temperature of 100 K, motional processes in the protein are decelerated, leading to freezing of different conformers and thus to broader lines. Therefore, it is not uncommon practice to perform DNP measurements at elevated temperatures. However, it is then necessary to ensure a sufficient DNP enhancement, especially above the 190 K – 200 K limit at which the glassy matrix usually melts. This matrix is commonly provided by a mixture of glycerol and water, and it is required to optimize

an even distribution of the analyte, biradical and the polarization throughout the sample, see also chapters 5 and 7 (123, 148, 162).

Proton detection combined with fast magic angle spinning

In NMR of proteins, the most important nuclei are ^{13}C, ^{15}N and ^{1}H. Because of their large gyromagnetic ratio, protons are the most sensitive. Detecting ^{13}C and ^{15}N is less sensitive, because their gyromagnetic ratios are about $^{1}/_{4}$ and $^{1}/_{10}$, respectively, of $\gamma(^{1}H)$. For sensitivity reasons, it is therefore desirable to detect ^{1}H in biological NMR. Due to the averaging of anisotropic interactions between nuclear spins through tumbling motions of the biomolecule, protons can be easily detected in solution-state NMR. In solid-state NMR, however, proton detection is not as trivial. The gyromagnetic ratio contributes itself squared to the Hamiltonian describing the homonuclear dipolar coupling (see equations (1.8), (1.9) and (1.10), pages 15 and 16). Therefore, protons form a strongly coupled dipolar network and exhibit usually drastically broadened lines in solid-state NMR under MAS at moderate frequencies (10 – 20 kHz). This leads to lack of spectral resolution that is required for the analysis of biomolecules, even when applying ^{1}H–^{1}H decoupling approaches such as CRAMPS or Lee-Goldburg derived pulse sequences (163).

In the past 15 years, this issue has been addressed by two important technical developments in the field. Firstly, preparing the protein in a deuterated form leads to a dilution of the proton spin bath and thus to a reduction of the network of strong dipolar couplings. After reintroduction of protons at exchangeable sites, e.g. at the amide positions in the protein backbone, a selected set of protons becomes available for detection with sufficient spectral resolution (Figure 1.5.A) (163-165). Secondly, this approach has been combined with strong efforts in hardware development to make higher MAS frequencies available (163, 166-168). With fast MAS, the net dipolar couplings between ^{1}H spins are further averaged out and reduced. In favorable cases, combining moderate MAS frequencies with protein deuteration can already lead to fully resolved proton-detected heteronuclear correlation spectra (165, 169). Proton-detected solid-state NMR spectra at 40 kHz and 60 kHz MAS have been recorded of

A

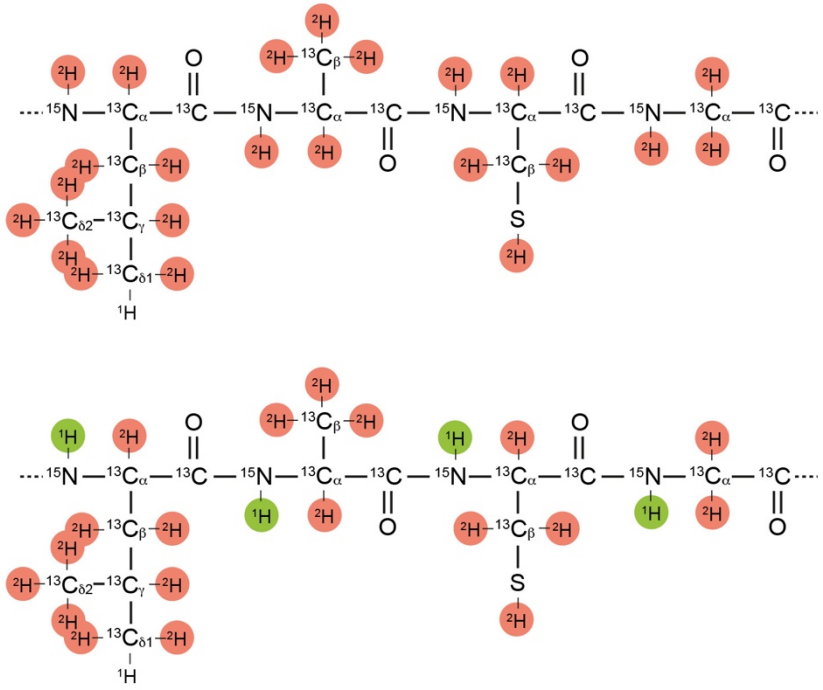

B

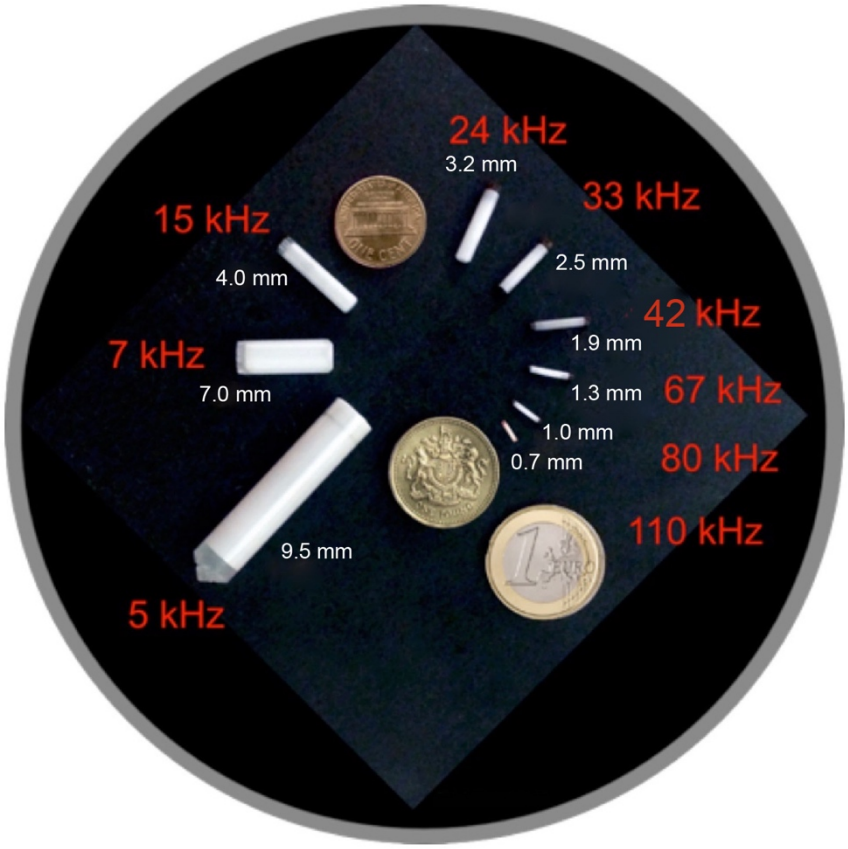
24 kHz
3.2 mm
33 kHz
2.5 mm
42 kHz
1.9 mm
67 kHz
1.3 mm
80 kHz
1.0 mm
110 kHz
0.7 mm
15 kHz
4.0 mm
7 kHz
7.0 mm
5 kHz
9.5 mm

Figure 1.5. Proton-detected solid-state NMR profits from deuteration of proteins and high MAS frequencies using small rotors.
A *In order to reduce the strong dipolar couplings between ^{1}H spins, proteins are usually prepared in deuterated form (top). After $^{1}H/^{2}H$-backexchange, protons are reintroduced at exchangeable sites, e.g. at the amide positions in the protein backbone yielding a diluted ^{1}H spin bath (bottom). These protons can be detected at fast MAS with sufficient spectral resolution.*
B *To further minimize dipolar couplings between ^{1}H spins, high MAS frequencies up to 110 kHz are applied leading to improved ^{1}H linewidths. Therefore, different rotor sizes are available. The smallest rotor with a diameter of 0.7 mm allows the highest MAS frequency making proton-detected solid-state NMR on fully-protonated proteins feasible. Modified from warwick.ac.uk, © Józef Lewandowski.*

a large variety of deuterated proteins that are $^{1}H/^{2}H$ back-exchanged (170-175). Most recently, probes enabling MAS up to 110 kHz became available (126, 176). At such high spinning frequencies, reasonable ^{1}H linewidths can be obtained for some proteins even without deuteration, which is of great advantage for the sample preparation, see also chapter 4 (176-178). The speed of sound poses the upper limit for the MAS frequency. The smaller the rotor, the higher MAS frequencies can be applied (Figure 1.5.B). Even though this leads to some challenges in sample handling and preparation, the smaller rotors have the advantage of requiring less sample. The volume of a 0.7 mm MAS rotor, for example, is 0.59 µL. Therefore, protein amounts in the order of 200 µg to 400 µg are sufficient to obtain a maximum in signal-to-noise ratio (S/N) with a 0.7 mm rotor that can be used at 110 kHz MAS (126, 179-181).

Another general advantage of proton detection is the gain in sensitivity compared to ^{13}C- or ^{15}N-detection. Based on the relative gyromagnetic ratios, the gain in S/N of ^{1}H-detection compared to ^{13}C-detection is (1.12):

$$\left(\frac{\gamma(^{1}H)}{\gamma(^{13}C)}\right)^{3/2} = \left(\frac{1}{0.25}\right)^{3/2} = 8 \qquad (1.12)$$

In the case of ^{15}N, this improvement is even larger (a factor of 40). The gain in sensitivity is one of the advantages of ^{1}H detection. In addition, the resolution of protons as a result of the fast spinning can be further exploited by including ^{1}H as additional dimension in multidimensional NMR spectra. This enables the acquisition of proton-detected triple-resonance experiments such as (H)CONH or (H)CANH in analogy to solution-state NMR (167, 170). In solid-state MAS NMR, the employed magnetization transfers in these experiments can be based on dipolar couplings using CP, or on scalar couplings by applying for example the 'insensitive nuclei enhanced by polarization transfer (INEPT)'-scheme (179, 182, 183). This approach facilitates the assignment procedure of the NMR signals compared to the traditional assignment concept based on ^{13}C-detected experiments (170, 184, 185).

In summary, the methodological development in proton-detected solid-state MAS NMR provides the possibility to study proteins of any size by the full repertoire of NMR spectroscopy. This includes triple-resonance experiments, whereby protein amounts below 1 mg are sufficient and deuteration is no longer required (176-178, 180). Combined with applying sedimentation of soluble proteins or biomolecular complexes, this method has the potential to study all protein classes independent of the expression system – even using mammalian cells, making structural studies of proteins with native glycosylation patterns conceivable.

Resonance assignment procedures

In basically all NMR-supported structural biology studies, the unambiguous identification of the signals, i.e. resonances, is a crucial step. Each nucleus has to be unequivocally connected to its corresponding resonance in a procedure called resonance assignment. An option to assign resonances is the use of mutations. This approach, however, is not practical if a full assignment of the protein is necessary because it may require a large number of samples causing very high costs. In unfavorable cases, it also may not lead to unequivocal assignments.

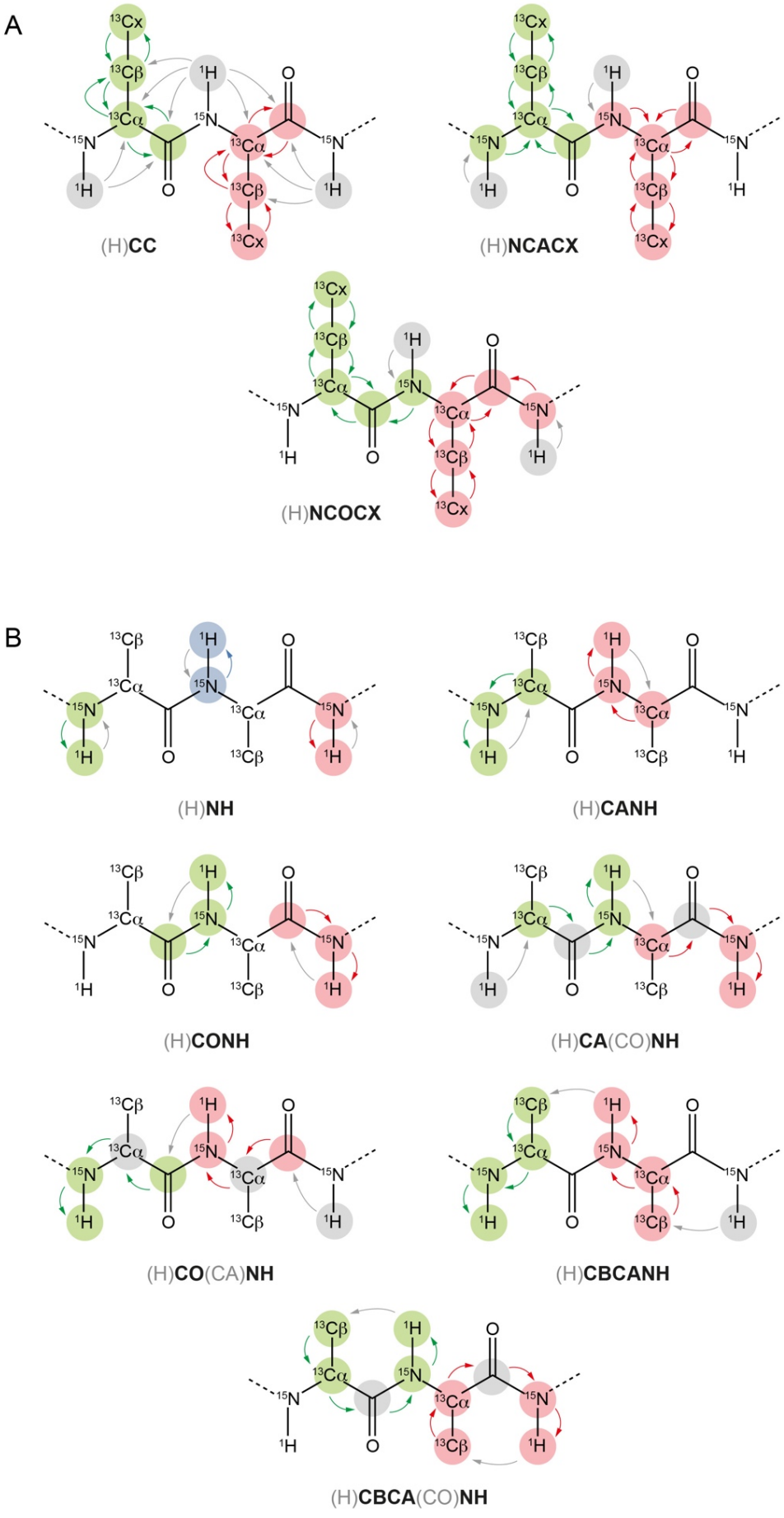
A
(H)CC
(H)NCACX
(H)NCOCX
B
(H)NH
(H)CANH
(H)CONH
(H)CA(CO)NH
(H)CO(CA)NH
(H)CBCANH
(H)CBCA(CO)NH

Figure 1.6. Magnetization transfer schemes of two- and three-dimensional solid-state MAS NMR spectra for resonance assignments. *Arrows indicate a transfer of magnetization, whereas grey arrows show the initial CP transfer from ^{1}H. All nuclei that are used during the experiment are labeled with circles, but a spectral dimension is evolved only for colored nuclei (grey nuclei are excited, but not evolved, which is indicated by brackets in the name of the experiment). The different colors (green, red and blue) indicate atoms that can be correlated with each other in the respective spectrum.*

A *The basis set of ^{13}C-detected experiments for resonance assignments is composed of a two-dimensional (H)CC and the three-dimensional experiments (H)NCACX and (H)NCOCX.*

B *In proton-detected solid-state MAS NMR, amides in the protein backbone can be identified in a two-dimensional (H)NH experiment. The ^{1}H, ^{15}N, $^{13}C'$, $^{13}C\alpha$ and $^{13}C\beta$ chemical shifts can be assigned with the three-dimensional (H)CANH, (H)CONH, (H)CA(CO)NH, (H)CO(CA)NH, (H)CBCANH and (H)CBCA(CO)NH spectra. In these experiments, magnetization transfers can be based on CP or INEPT, depending on the MAS frequency and the length of the obtained T_2 coherences.*

It is desirable to assign spectroscopically all resonances in the native form of the protein. Traditionally, the resonance assignment in solid-state NMR of proteins is based on ^{13}C-detected experiments. Initially, rather low or moderate MAS frequencies (< 40 kHz) have been available in solid-state NMR. Therefore, an assignment protocol has been established employing two- and three-dimensional experiments such as (H)CC, (H)NCACX and (H)NCOCX (Figure 1.6.A) (139, 186-188). Proton driven spin diffusion (PDSD) or dipolar assisted rotational resonance (DARR) mixing schemes are usually used for transfer of magnetization between the carbon spins (189, 190, 191). Using two-dimensional (H)CC spectra, the resonances of individual amino acids can be identified based on their characteristic cross peak patterns. In a following step, they can be sequentially connected according to the amino acid sequence with the three-dimensional experiments (H)NCACX and (H)NCOCX. This approach, however, is not straightforward to apply in many cases, e.g. for large proteins. For larger proteins, the carbon-carbon mixing can lead to crowded spectra, making amino acid typing difficult (3, 192). Using sparsely labeled samples, either amino acid

selective or prepared with a more general labeling scheme, for example by using [1,3-^{13}C]- and [2-^{13}C]-glycerol, these difficulties can be resolved to some degree and facilitate the resonance assignment (139, 187). For very large proteins, however, this approach might not be sufficient to achieve a complete assignment (3, 118).

The advent of proton detection in solid-state NMR enabled a new assignment strategy (167, 170, 185). In principle, the assignment procedure using proton-detected solid-state MAS NMR spectra is very similar to that in solution-state NMR. To ensure a sufficient S/N in all experiments, ^{1}H linewidths should be narrow and the effective T_2-relaxation times of the nuclear spins used in the pulse sequence should be long enough. In a first step, a two-dimensional (H)NH correlation is recorded, to correlate amide protons to their nitrogens in the protein backbone (Figure 1.6.B) (167, 185). Subsequently, these pairs are connected to the neighboring Cα and C' atoms using (H)CANH and (H)CONH spectra, respectively. Using a second set of three-dimensional experiments, (H)CA(CO)NH and (H)CO(CA)NH, a sequential backbone walk can be performed (170). To facilitate amino acid identification, three-dimensional (H)CBCANH and (H)CBCA(CO)NH experiments might prove informative. This set of spectra allows a full assignment of the Cα, Cβ, C', N and H atoms in the protein. With the help of very fast MAS (110 kHz), the amino acid side chains can be assigned, by making use of a proton-detected three-dimensional (H)CCH spectrum recorded on a fully-protonated sample. In addition, ^{1}H-^{1}H correlations can be used to validate assignments or for distance restraint collection (176, 193, 194). The dataset might be complemented by two-dimensional ^{13}C-detected (H)CC spectra recorded with different mixing schemes at moderate MAS frequency on a fully-protonated sample, to assign and correlate the carbon atoms of the amino acid side chains (118).

1.3 Scope of the Thesis

Protonation dynamics may be one of the fundamental mechanistic principles determining the molecular function of proteins. NMR spectroscopy is a powerful method for investigating it, as it allows to detect protons directly. In addition, structural features can be studied in a large temperature range and native-like protein environments. However, solution-state NMR is not applicable to all proteins due to its size-limitations and the requirement of solubilization. In addition, not all functionally-relevant protons in proteins may be detectable by solution-state NMR, e.g. for entropic reasons. Therefore, it is desirable to make additional structural biology methods available to protonation dynamics investigations. In this work, proton detection and DNP are applied as two advanced solid-state MAS NMR methods to study protonation dynamics.

Some time ago, proton-detected solid-state NMR at fast MAS has been developed and established in structural biology. In this thesis, it is used to study protonation dynamics in complex proteins. To make use of its advantages, proton detection is tested for observation of hydrogen bonds. In particular, it is applied to address proton delocalization site-specifically with atomic resolution. This question is studied in bacteriorhodopsin, measured in its native membrane. The detection of the involved protons is anticipated to resolve their exchange at key amino acid side chains of this proton pump. To test its applicability to fully protonated proteins, proton-detected NMR at 100 kHz MAS is employed to study the extra-cellular domain of the neonatal Fc receptor. In the context of a druggability study, an innovative methodology is presented to detect protons in such large, soluble proteins that cannot be deuterated. The aim is to develop a small molecule that can be used after optimization as an inhibitor of a protein-protein interaction based on protonation dynamics. With this approach, only small sample quantities are required, and the protein under investigation can be produced in any expression system.

Cross-effect DNP is explored as an approach to investigate structural features related to protonation dynamics that are difficult to observe by other methods. So far, DNP has limitations in spectral resolution between 100 K and 200 K and in efficiency above 200 K. Therefore, it is further improved in two development studies. The first one is intended to achieve higher DNP enhancements at temperatures towards 200 K by

examining the influence of biradical-deuteration on the increase in S/N. In the second investigation, the performance of bcTol as a new biradical with increased water-solubility is characterized. To demonstrate the value of DNP-enhanced solid-state MAS NMR in protonation dynamics studies, it is subsequently applied to channelrhodopsin (ChR) and the phytochrome photoreceptor Cph1. ChR is studied in lipid bilayers, addressing the retinal chromophore structure in dark-adapted samples. The retinal structure is an important feature related to protonation dynamics in this light-sensitive membrane protein. In the field of optogenetics, ChRs are widely used to investigate neuronal networks through light control (195-200). Phytochrome photoreceptors show characteristic features of protonation dynamics during the photocycle, as introduced in chapter 1. In recent years, the chromophore structure and the binding pocket have been investigated by solution-state and conventional solid-state NMR (65, 67, 201-207). In these previous studies, however, an unequivocal assignment of the nitrogen resonances in the chromophore was not possible due to low sensitivity. As the nitrogens are key players in the events of protonation dynamics during molecular action of phytochromes, it is highly desirable to study their role using NMR. Profiting from the high water-solubility of bcTol, we addressed this issue by applying DNP to the soluble Cph1 protein, measured in frozen solution.

Almost all projects have been performed in collaborations, mainly within the CRC1078 with the groups of Peter Hegemann (Humboldt University of Berlin), Peter Hildebrandt (Technical University of Berlin), Jon Hughes (University of Gießen) and Roland R. Netz (Free University of Berlin). Other key collaborations for the studies presented in this work have been with the groups of Marc Nazaré (FMP Berlin), Thomas Prisner (University of Frankfurt), Jörg Matysik (University of Leipzig), Snorri Th. Sigurdsson (University of Iceland), Beat H. Meier (ETH Zürich) and the company UCB Pharma.

2

EXPLORING LONG-RANGE CONTACTS AND HYDROGEN BONDS IN PROTEINS BY PROTON-DETECTED SOLID-STATE MAGIC-ANGLE-SPINNING NMR

2.1 Synopsis

In protonation dynamics studies, direct proton detection combined with fast MAS is a promising technique to study functionally-relevant protons in membrane proteins and large proteins. Therefore, it is used in this work to address protonation dynamics questions in such complex proteins.

As described in chapter 1, proton detection benefits from increased sensitivity compared to ^{13}C- and ^{15}N-detection. In addition, it introduces another spectral dimension making triple-resonance spectroscopy possible, thereby improving spectral resolution. These spectroscopic reasons are certainly a methodological advantage of proton detection. In addition, it allows detection of protonation states of different chemical moieties in the context of protonation dynamics studies. As these experiments can be performed at room temperature, it also gives access to kinetic information such as chemical exchange of protons between different sites, e.g. water and functional amino acid side chains.

In the current chapter, we propose a proton-detected solid-state MAS NMR experiment that can be used to investigate hydrogen bonds. These are important non-covalent interactions to stabilize protein structure and are involved in various molecular mechanisms enabling protein function. Therefore, it is desirable to identify them and to provide the possibility to investigate changes in hydrogen bonding networks between different conformational states of proteins. With the presented experiment, such hydrogen bonds can be detected. As we show, it can be used to distinguish secondary structure elements. In α-helices, hydrogen bonds between CO_i and H^N_{i+4} exist, whereas in β-sheets different patterns occur in the parallel (hydrogen bonds between every other CO_i and H^N_{j+1}) and antiparallel (hydrogen bonds between every other CO_i and H^N_j) case. We test the experiment with the model protein SH3 using 40 kHz MAS at room temperature.

This study may serve as a basis to further investigate the role of hydrogen bonds and their changes between transitions of different conformational states. Such studies, however, require a possibility to stabilize conformational states selectively. Depending on the protein under investigation, this could be accomplished by using mutants or light-irradiation combined with low temperatures. The latter, however, would require the availability of a fast MAS probe with very efficient cooling capacities.

2.2 Personal contribution

I recorded NMR spectra of SH3, analyzed data and was involved in writing the manuscript. The protein was expressed and purified by Anne Diehl and Kristina Rehbein.

Andrew J. Nieuwkoop, Daniel Friedrich and Hartmut Oschkinat designed the study; Andrew J. Nieuwkoop and Daniel Friedrich performed research; Andrew J. Nieuwkoop and Daniel Friedrich analyzed data; Andrew J. Nieuwkoop and Daniel Friedrich wrote the manuscript.

2.3 Manuscript in Preparation

Andrew J. Nieuwkoop,[#] **Daniel Friedrich**,[#] and Hartmut Oschkinat:
'Exploring Long-range Contacts and Hydrogen Bonds in Proteins by Proton-detected Solid-state Magic-Angle-Spinning NMR', *manuscript in preparation*
[#] ***Equal contribution***

Exploring Long-range Contacts and Hydrogen Bonds in Proteins by Proton-detected Solid-state Magic-Angle-Spinning NMR

Andrew J. Nieuwkoop[1,‡,#], Daniel Friedrich[1,2,#], and Hartmut Oschkinat[1,2,*]

[1] Leibniz-Forschungsinstitut für Molekulare Pharmakologie (FMP), Robert-Rössle-Str. 10, 13125 Berlin, Germany

[2] Freie Universität Berlin, Institut für Chemie und Biochemie, 14195 Berlin, Germany

[‡] present address: Rutgers University, Department of Chemistry and Chemical Biology, 610 Taylor Road, Piscataway, NJ 08854, USA

# These authors share first authorship.

* Correspondence should be addressed to oschkinat@fmp-berlin.de

Abstract

Protons play an essential role in both formation of structure and modulation of function in proteins. In particular, probing hydrogen bonds provides detailed insight into protein structure and their mechanisms in molecular function. In addition, collecting distance restraints of protons to heteronuclei such as carbonyl- and α-carbons in the protein backbone allows to identify secondary structure elements. Here, we report a proton-detected fast magic-angle-spinning (MAS) solid-state NMR experiment that is particularly useful for detecting hydrogen bonds. Our results contain information about secondary structure as tested on the microcrystalline protein SH3. The presented experiment can be used to validate assignments in solid-state MAS NMR spectra and provides a basis to distinguish parallel and antiparallel β-sheets in proteins. Our approach shows the value of fast MAS and opens new routes in probing both secondary structure and the role of functionally-relevant protons in all targets of solid-state MAS NMR.

Introduction

One of the primary driving forces behind the folding of proteins is the formation of hydrogen bonds in secondary structure elements (Dobson, 2003; Jeffrey, 1997; Pace et al., 2014). The ubiquitous presence of β-sheets and α-helices in protein structures is a direct result of these two elements maximizing the number of hydrogen bonds available. In addition, hydrogen bonds are essential in coordinating functionally-relevant water molecules and modulating interactions between biomolecules and their interactions with proteins, lipids, nucleic acids, and small molecules (Baker and Hubbard, 1984; Gonen et al., 2005; Jones and Thornton, 1996; Poornima and Dean, 1995; Steitz, 1990). Considering the methodological repertoire in structural biology, NMR spectroscopy is particularly well-suited to study protons and their interactions with heteroatoms such as nitrogen and carbon at atomic resolution (Andreas et al., 2015; Hong et al., 2012; Zhou et al., 2012).

Magic-angle-spinning (MAS) solid-state NMR is rapidly becoming a reliable technique for structural investigations of insoluble proteins, such as fibrils, functional aggregates, and membrane proteins (Castellani et al., 2002; Loquet et al., 2013; Lu et al., 2013; Shahid et al., 2012; Tuttle et al., 2016; Wasmer et al., 2008). The large increase in sensitivity gained from proton-detection compared to ^{13}C- and ^{15}N-detection means that larger and more complex systems can be addressed with smaller amounts of material. Crucial to the success of proton-detection has been the combination of high MAS frequencies (> 40 kHz) with protein deuteration while some work on fully protonated samples has been promising, especially at the highest MAS frequencies routinely available (Andreas et al., 2016; Lewandowski et al., 2011; Nieuwkoop et al., 2015; Reif, 2012; Struppe et al., 2017). For larger systems

deuteration followed by back-exchange at the labile sites has proved extremely effective at sharpening proton linewidths by limiting the number of protons in the core of the protein (Akbey et al., 2010; Chevelkov et al., 2006). This minimal bath of protons has additional benefits useful in acquiring structural restraints which we have designed an experiment to take advantage of. Since hydrogen atoms attached to nitrogen atoms which are involved in hydrogen bonds are the same present in back-exchanged samples, the situation seems ideal for determining which of these bonds are present in protein structure.

An added reason to be optimistic about the prospects of detecting hydrogen bonds and long-range contacts between protons and Cα-atoms in proton-detected experiments is the continued success of proton-carbon cross polarization (CP) in deuterated samples. CP has long been used in solid-state NMR to gain sensitivity by utilizing the higher initial polarization and shorter relaxation times of ^{1}H relative to ^{13}C or ^{15}N (Pines, 1972). While transfers to directly bonded nuclei are most efficient, CP is a dipolar process, which means it should be useful for detecting through space interactions in addition to increasing initial polarization in experiments. In the sparsely protonated context of a back-exchanged sample, this is especially the case. It has been demonstrated that protons in hydrogen bonds and hydroxyl protons can be detected by solid-state MAS NMR using CP (Agarwal, 2010).

To demonstrate this idea, we acquired a 2D (H)COH experiment on the SH3 domain of chicken α-spectrin (Figure 1A). This experiment consists of two ^{1}H-^{13}C CP transfers, both of which were set to a longer contact time (4 ms) than is traditionally used. This results in each carbonyl being correlated to multiple protons. For example, the carbonyl resonance of G51 correlates to amide protons of residues in close proximity (V44, F52, V53, Q50 and V23) (Figure 1A and 1B).

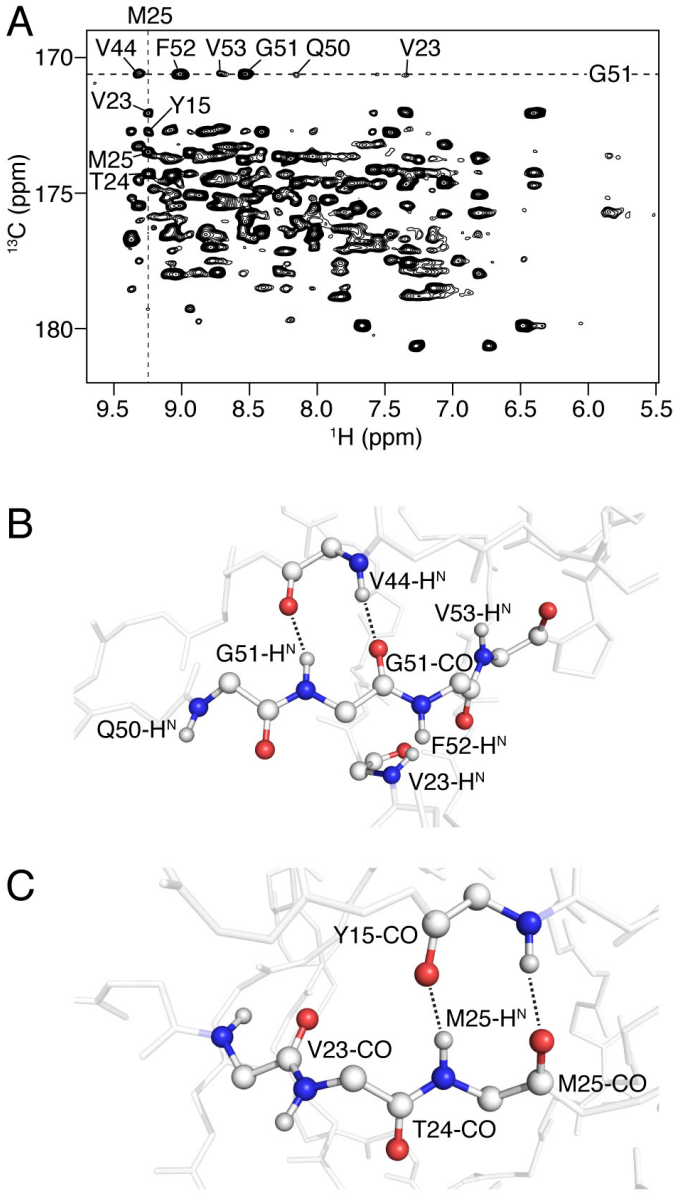

Figure 1. Correlations between amide protons and carbonyls in SH3. (A) Solid-state (H)COH 2D spectrum at 40 kHz MAS with long contact times for both CP-transfer steps. Dashed lines indicate cross peaks of G51 and M25. **(B)** Structural view of amide protons correlating to the carbonyl of G51 in the (H)CH 2D spectrum. Dashed lines indicate hydrogen bonds. **(C)** Carbonyls of residues close to the amide proton of M25, hydrogen bonds are indicated by dashed lines.

The strong signal involving V44-H^N corresponds to an amide proton that is hydrogen bonded with the CO of G51. The M25-H^N shows correlations to carbonyl signals of

sequential residues (M25, T24 and V23), but also to Y15-CO which is involved in a hydrogen bond (Figure 1A and 1C). Overall, this spectrum shows the promise of using long CP mixing times in deuterated samples to detect hydrogen bonds. Correlating each carbon to many protons, however, results in crowded 2D spectra, even for the relatively small protein SH3. Therefore, we set out to design a 3D experiment which will be useful in larger systems.

In this study, we present a proton-detected 3D solid-state MAS NMR experiment that can be used to resolve long-range correlations observed in crowded (H)CH 2D spectra employing long CP contact times. We introduce a ^{15}N-dimension resulting in a sensitive 3D experiment, which can be used for detecting through-space contacts between protons and both Cα and CO nuclei. It can be applied to detect hydrogen bonds, as we show for a microcrystalline preparation of the α-spectrin SH3 domain. We test the experiment on a ^{2}H,^{15}N,^{13}C-labeled sample at 40 kHz MAS, but the experiment can be used at higher MAS frequencies as well. In favorable cases, fully-protonated samples may be studied at 100 kHz MAS if well-resolved spectra can be obtained. Long-range contacts between Cα and H^N are observed, as well as characteristic cross-peak patterns reflecting the expected hydrogen bonds in antiparallel β-sheets. In addition, the CO of prolines can be observed and correlated to H^N resonances of residues close in space.

Results and Discussion

The essential unit of the proposed experiment is a long mixing ^{13}CO-^{1}H CP step of about 4–6 ms. The most straightforward implementation of an appropriate 3D experiment would be to evolve the first ^{1}H dimension to achieve an HCH 3D. This approach would have limitations however, as the chemical shift dispersion of both ^{1}H and ^{13}CO are not particularly large. If, however, we introduced a ^{15}N dimension, we could gain additional spectral resolution. One method for doing this would be to frequency-label the initial ^{1}H site at the beginning of the traditional (H)CONH type experiment. While the HCONH type 4D experiment may have promise, if we want to limit ourselves to 3D an H(CO)NH type experiment has the disadvantage of placing the hydrogen-bonded ^{1}H in the indirect dimension. This cannot be as well digitized and as such would be less efficiently resolved. By exchanging the ^{13}C and ^{15}N dimensions, we could instead measure the hydrogen-bonded proton in the direct dimension, via an HN(CO)H type 3D. This experiment would label an HN plane to identify the CO site, and then utilize the direct dimension to identify the amide proton nearby. This transfer pathway could be used further to acquire an (H)NCOH 3D, which uses a NCO plane to identify the CO site (Figure 2). Depending on the resolution achieved in the HN or NCO planes, either could prove useful.

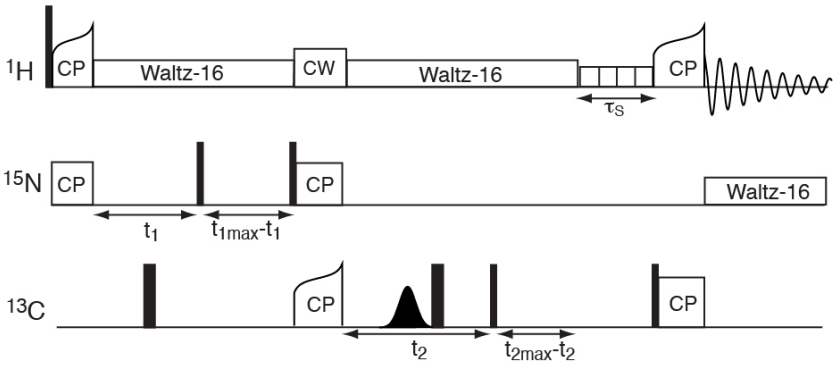

160

161 **Figure 2. Pulse sequence for detecting hydrogen bonds.** The ^{15}N dimension is
162 introduced to gain spectral resolution. To probe the H-CO interaction, a long mixing
163 time in the last CP step from ^{13}CO to ^{1}H is applied. Both the acquisition of (H)NCOH
164 and HN(CO)H can be used to investigate hydrogen bonds between carbonyls and
165 amides. The experiment can be easily modified to collect a (H)NCAH spectrum.
166

167

168 To observe correlations involving the ^{13}Cα resonances, this experiment can be
169 modified by utilizing a selective CP transfer from nitrogen to ^{13}Cα followed by
170 evolution of the ^{13}Cα frequencies. This version should be acquired as an (H)NCAH
171 3D to make benefit of the dispersion of the ^{13}Cα resonances. Similar to the experiment
172 involving CO, it is important to apply a long CP contact time (about 4–6 ms) for the
173 transfer from carbon to protons before acquisition to probe long-range contacts of the
174 frequency-labeled NCA pair to protons nearby.
175 We tested both the (H)NCOH and the (H)NCAH experiments on a microcrystalline
176 sample of the α-spectrin SH3 domain to evaluate observed signals towards their long-
177 range correlations. A characteristic example is the cross peaks involving the residues
178 Y15 and M25 (Figure 3A). In the (H)NCAH experiment, correlations of the NCA pair
179 of M25 to multiple proton sites can be detected (grey spectrum and grey lines). The
180 strongest signals result from the amide protons of M25 and the neighboring residues

K26 and T24. Structurally more relevant are correlations to amino acids in the next β-strand involving the amide protons of D14, Y15, Q16 and E17. They appear to be much weaker as the M25 and K26 signals due to the longer distances. Based on the (H)NCOH spectrum, signals reflecting amide protons near the Y15-CO can be observed (red spectrum and red lines). These include trivial correlations to the amide proton of Y15 and the sequentially connected residues Q16 and E17. The cross peak to the amide proton of M25 reflects a hydrogen bond between the amide group of M25 and the Y15-carbonyl. This shows the great value of the proposed experiment to detect hydrogen bonds in proteins. In addition, a weak long-range correlation to the amide proton of K26 can be detected.

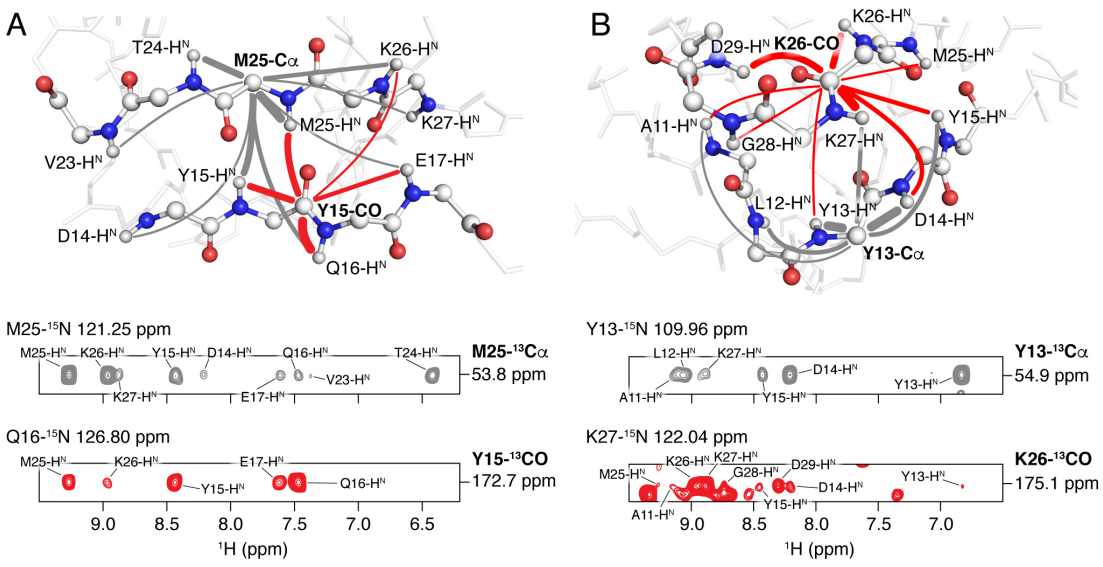

Figure 3. Hydrogen bond and long-range contact patterns detected in secondary structure elements. (A) β-sheet and **(B)** turn-like secondary structure in microcrystalline SH3. The (H)NCAH and (H)NCOH correlations are shown in grey and red, respectively. Nitrogen atoms are shown as blue, oxygen as red, hydrogen atoms as small white and carbon atoms as big white spheres. The lines in the structural illustration indicate observed interactions and their thickness reflects the corresponding signal intensity.

The situation is different in a turn-like secondary structure (Figure 3B). Here, contacts between Y13-Cα and amide protons of A11, L12, Y13, D14 and Y15 can be observed (grey spectrum and grey lines). K27-H^N is the only amide proton of a residue that is not close in sequence but still yielding a cross peak to Y13-Cα. The carbonyl of K26, however, shows multiple long-range interactions to amide protons of A11, Y13, D14, Y15, M25, K26, K27, G28 and D29 which are close in space (red spectrum and red lines). But, in contrast to the β-sheet, none of these reflects a hydrogen bond due to the less defined secondary structure. This shows how the proposed experiment can be used to identify secondary structure elements.

Another value of the long CP contact time employed in the experiments presented here is the possibility to correlate the CO of a proline to amide protons close in space (Figure 4). This has a great advantage since prolines are often not visible in proton-detected NMR experiments due to their tertiary amine nature of the nitrogen. The ability to correlate a proline CO to amide protons close in sequence or in space facilitates their assignment, and allows the detection of hydrogen-bonded proline carbonyls.

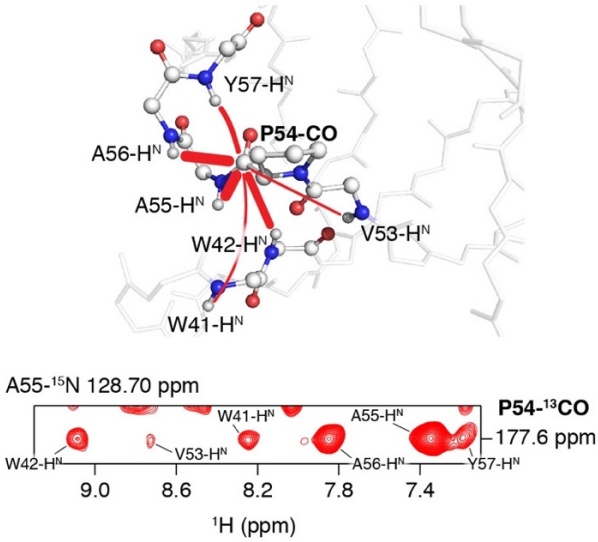

Figure 4. Detection of CO of a proline in SH3. The H^N of amino acids close in space can be used as probes to observe the CO of prolines. Again, the lines in the structural illustration indicate the observed interactions and their thickness reflects the cross peak intensity.

The determination of intermolecular hydrogen bonds at atomic resolution can provide further insight into binding mechanisms and interactions of biomolecules and therefore into their function (Janin et al., 2008). In contrast, different structural elements in proteins can be investigated based on intramolecular hydrogen-bonding patterns. For both purposes, the presented solid-state MAS NMR experiments may be useful.

In the intramolecular case, the presence of β-sheet, random coil or α-helix as secondary structure elements leads to different closest amide protons to carbonyls. While the cross peak of the CO to the amide proton of one amino acid and the signals correlating the CO_i and H^N_{i+1} are trivial, different signal patterns can be observed for β-sheet, random coil and α-helix. The latter typically contains hydrogen bonds between CO_i and H^N_{i+4} (Figure 5A), whereas β-sheets show hydrogen bond patterns between amino acids further apart in the protein sequence. Especially analyzing which

amino acids have hydrogen bonds to each other can provide insight if parallel (hydrogen bonds between every other CO_i and H^N_{j+1}) or antiparallel (hydrogen bonds between every other CO_i and H^N_j) β-sheets exist (Figure 5B). This can be used as structural constraints to identify secondary structural elements.

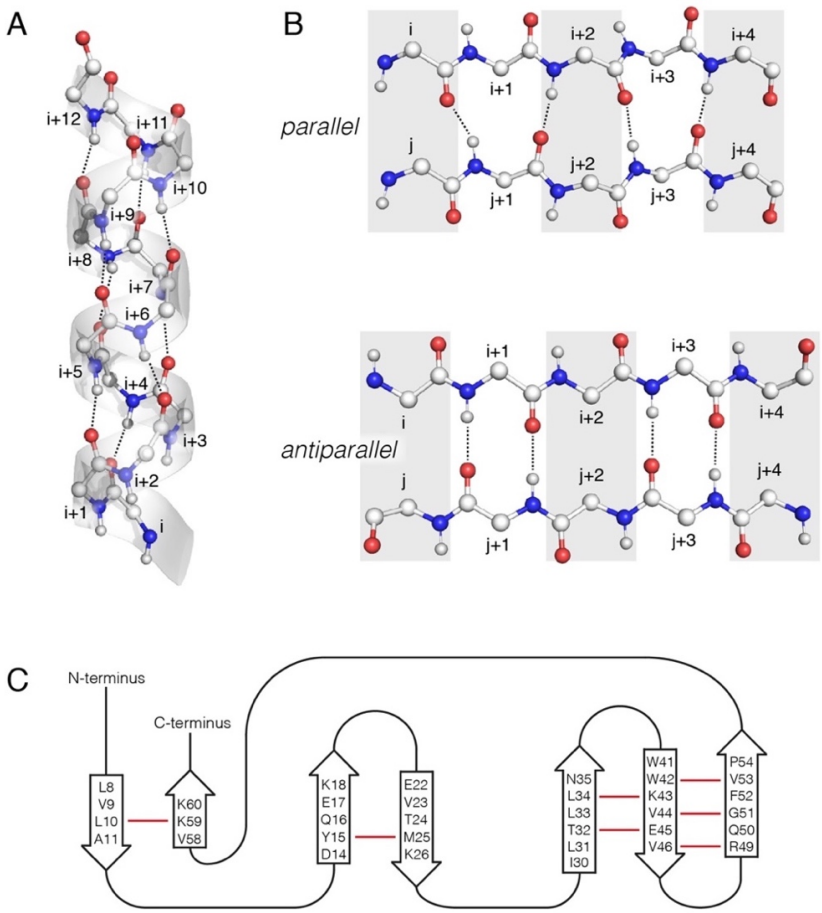

Figure 5. Characteristic hydrogen bond patterns in secondary structure elements. (A) In an ideal α-helix (PDB code 4U1H (Kløverpris et al., 2015)), hydrogen bonds are formed between CO_i and H^N_{i+4}. **(B)** Different hydrogen bonding patterns are expected in idealized parallel (every other CO_i and H^N_{j+1}) and antiparallel (every other CO_i and H^N_j) β-sheets (PDB codes 2LBU and 2LNQ, respectively (Qiang et al., 2012; Schütz et al., 2011)). Nitrogen atoms are shown as blue, oxygen as red, hydrogen atoms as small white and carbon atoms as big white spheres. **(C)** Secondary structure of SH3 (based on PDB 1U06 (Chevelkov et al., 2005)) and hydrogen bonds in the antiparallel β-sheets (red lines).

In the SH3 domain, three antiparallel β-sheets exist, consisting of seven β-strands in total (Figure 5C). In the three-dimensional (H)NCOH spectrum, cross peaks can be observed for a number of amino acids that form hydrogen bonds. These include, for example, L10–K59 with the expected correlations between L10-CO and K59-H^N, and L10-H^N and K59-CO. Such a cross peak pattern corresponds to the hydrogen bonds formed in an antiparallel β-sheet (Figure 5B). The same is observed for the second β-sheet, for which signals reflecting the two hydrogen bonds between Y15 and M25 are detected. This β-sheet is slightly twisted, therefore the CO and H^N of E17 and V23 do not form hydrogen bonds and thus signals cannot be observed. The third β-sheet that is formed by three β-strands shows hydrogen bonding between the CO and H^N atoms of 10 amino acids. Two hydrogen bonds are found between the first two strands (T32–E45 and L34–K43), and three between the second and third strands (W42–V53, V44–G51 and V46–R49). In this β-sheet, the characteristic hydrogen bonding pattern for the antiparallel case is observed.

Conclusion

In summary, we present a three-dimensional proton-detected solid-state MAS NMR experiment that resolves through-space contacts of protons to carbons. As a (H)NCOH, it can be used to explore hydrogen bonds to identify secondary structure elements. This is especially useful to distinguish parallel and antiparallel β-sheets through the respective hydrogen bonding patterns. As we show, the expected hydrogen bonds for the antiparallel β-sheets in the model protein SH3 can be detected. The experiment gives also access to the chemical shift of proline carbonyls, which is not the case in conventional proton-detected solid-state MAS NMR experiments.

In future studies, the experiment may also be useful to investigate hydrogen bonds between amino acid side chains such as aspartate/glutamate and other residues, for example arginine side chains. In such cases, however, the experiment needs to be modified since it features a ^{15}N-filter that does not allow to observe signals of ^{13}Cγ/δ in aspartate and glutamate, respectively. Similarly, the ^{13}CO-filter prevents magnetization transfer involving the guanidinium group of arginine and thus the observation of this moiety as hydrogen bonding partner. By adding a ^{13}C-^{13}C mixing step, such correlations could be collected in a (H)CCOH-type experiment. Alternatively, it could be extended to an (H)N(H)COH experiment to still make use of the ^{15}N chemical shift. In addition to investigating hydrogen bonds, the experiment can be used to collect long-range contacts by recording it as a (H)NCAH spectrum.

Materials and Methods

All experiments were recorded on a 900 MHz Avance III Bruker NMR spectrometer equipped with a 1.9 mm four-channel (HCND) MAS solid-state probe using a microcrystalline $^{2}H,^{13}C,^{15}N$-labeled SH3 sample (70 % reprotonated at exchangeable sites). The variable temperature was set to 240 K and the MAS frequency to 40 kHz for all experiments, and $\pi/2$ pulses of 100 kHz for ^{1}H, 50 kHz for ^{13}C and 41.67 kHz for ^{15}N were used. MISSISSIPPI water suppression with 35 ms pulses before the last CP transfer and WALTZ-16 ^{1}H decoupling during indirect evolution periods was applied in all experiments. The protein was expressed and purified as described in Akbey et al. and Nieuwkoop et al., and the proton level was adjusted using a $^{1}H_2O/^{2}H_2O$ mixture of 70% $^{1}H_2O$ (Akbey et al., 2010; Nieuwkoop et al., 2015).

For the (H)COH 2D experiment, a contact time of 4 ms was used for both CP steps. Linear ramps of 100% – 75% and 80% – 100% were applied on ^{1}H during the first and second CP transfers, respectively. The carrier was set to 174.6 ppm on ^{13}C during the experiment. Both CP steps were optimized around 60 kHz for ^{1}H and 20 kHz for ^{13}C to fulfill the n=1 Hartmann-Hahn condition. 4096 data points at a sweep width of 50 kHz and a maximum acquisition time of 41 ms were acquired in the direct ^{1}H dimension. 256 T_2 increments at a sweep width of 6.67 kHz were collected in the indirect ^{13}C dimension, corresponding to a maximum acquisition time of 19.2 ms. An interscan delay of 1 s was used, and 4 scans per slice were acquired.

For the (H)NCOH 3D experiment, a contact time of 1.5 ms for the ^{1}H-^{15}N CP transfer was applied, optimized around 60 kHz for ^{1}H with a linear 100% – 80% ramp and 20 kHz for ^{15}N. A contact time of 10 ms was used for the ^{15}N-^{13}CO CP, optimized around 30 kHz for ^{15}N with a tangential 40% – 60% shape and 10 kHz for ^{13}CO. The

^{13}CO-^{1}H CP transfer was the same as in the (H)COH 2D experiment. 4 scans with an interscan delay of 1 s were recorded. The ^{13}C carrier was set to 174.6 ppm and for ^{15}N to 115.7 ppm. 96 increments were collected in both the ^{15}N dimension (sweep width 3.33 kHz, 14.4 ms acquisition time) and the ^{13}C dimension (sweep width 5 kHz, acquisition time of 9.6 ms). 4096 data points with a sweep width of 50 kHz and 41 ms acquisition time were recorded in the direct ^{1}H dimension.

The (H)NCAH experiment was acquired with the same experimental conditions, except for using specific ^{15}N-^{13}CA and ^{13}CA-^{1}H CP transfers with the ^{13}C carrier set to 55.2 ppm. In this experiment, 192 slices were collected for ^{13}C at a sweep width of 10 kHz, yielding a maximum acquisition time of 9.5 ms in the carbon dimension.

Acknowledgment

We thank Anne Diehl and Kristina Rehbein for the preparation of the microcrystalline ^{2}H,^{13}C,^{15}N-labeled SH3 sample. Funding through the Deutsche Forschungsgemeinschaft (Sonderforschungsbereich 1078 B1) to Hartmut Oschkinat is kindly acknowledged.

References

Agarwal, V., Linser, R., Fink, U., Faelber, K., and Reif, B. (2010). Identification of hydroxyl protons, determination of their exchange dynamics, and characterization of hydrogen bonding in a microcrystalline protein. J. Am. Chem. Soc. *132*, 3187–3195.

Akbey, U., Lange, S., Trent Franks, W., Linser, R., Rehbein, K., Diehl, A., van Rossum, B.-J., Reif, B., and Oschkinat, H. (2010). Optimum levels of exchangeable protons in perdeuterated proteins for proton detection in MAS solid-state NMR spectroscopy. J Biomol NMR *46*, 67–73.

Andreas, L.B., Jaudzems, K., Stanek, J., Lalli, D., Bertarello, A., Le Marchand, T., Cala-De Paepe, D., Kotelovica, S., Akopjana, I., Knott, B., et al. (2016). Structure of fully protonated proteins by proton-detected magic-angle spinning NMR. Proceedings of the National Academy of Sciences *113*, 9187–9192.

Andreas, L.B., Le Marchand, T., Jaudzems, K., and Pintacuda, G. (2015). High-resolution proton-detected NMR of proteins at very fast MAS. Journal of Magnetic Resonance *253*, 36–49.

Baker, E.N., and Hubbard, R.E. (1984). Hydrogen bonding in globular proteins. Progress in Biophysics and Molecular Biology *44*, 97–179.

Castellani, F., van Rossum, B., Diehl, A., Schubert, M., Rehbein, K., and Oschkinat, H. (2002). Structure of a protein determined by solid-state magic-angle-spinning NMR spectroscopy. Nature *420*, 98–102.

Chevelkov, V., Faelber, K., Diehl, A., Heinemann, U., Oschkinat, H., and Reif, B. (2005). Detection of dynamic water molecules in a microcrystalline sample of the SH3 domain of α-spectrin by MAS solid-state NMR. J Biomol NMR *31*, 295–310.

Chevelkov, V., Rehbein, K., Diehl, A., Reif, B. (2006). Ultrahigh resolution in proton solid-state NMR spectroscopy at high levels of deuteration. Angew Chem Int Ed Engl *45*, 3878–3881.

Dobson, C.M. (2003). Protein folding and misfolding. Nature *426*, 884.

Gonen, T., Cheng, Y., Sliz, P., Hiroaki, Y., Fujiyoshi, Y., Harrison, S.C., and Walz, T. (2005). Lipid–protein interactions in double-layered two-dimensional AQP0 crystals. Nature *438*, 633–638.

Hong, M., Fritzsching, K.J., and Williams, J.K. (2012). Hydrogen-Bonding Partner of the Proton-Conducting Histidine in the Influenza M2 Proton Channel Revealed From 1H Chemical Shifts. J. Am. Chem. Soc. *134*, 14753–14755.

Janin, J., Bahadur, R.P., and Chakrabarti, P. (2008). Protein–protein interaction and quaternary structure. Quart. Rev. Biophys. *41*, 133–180.

Jeffrey, G.A. (1997). An Introduction to Hydrogen Bonding.

Jones, S., and Thornton, J.M. (1996). Principles of protein-protein interactions. Proc Natl Acad Sci USA *93*, 13.

Kløverpris, H.N., Cole, D.K., Fuller, A., Carlson, J., Beck, K., Schauenburg, A.J., Rizkallah, P.J., Buus, S., Sewell, A.K., and Goulder, P. (2015). A molecular switch in immunodominant HIV-1-specific CD8 T-cell epitopes shapes differential HLA-restricted escape. Retrovirology *12*, 20.

Lewandowski, J.R., Dumez, J.-N., Akbey, U., Lange, S., Emsley, L., and Oschkinat, H. (2011). Enhanced Resolution and Coherence Lifetimes in the Solid-State NMR Spectroscopy of Perdeuterated Proteins under Ultrafast Magic-Angle Spinning. J. Phys. Chem. Lett. *2*, 2205–2211.

Loquet, A., Sgourakis, N.G., Gupta, R., Giller, K., Riedel, D., Goosmann, C., Griesinger, C., Kolbe, M., Baker, D., Becker, S., et al. (2013). Atomic model of the type III secretion system needle. Nature *486*, 276–279.

Lu, J.-X., Qiang, W., Yau, W.-M., Schwieters, C.D., Meredith, S.C., and Tycko, R. (2013). Molecular structure of β-amyloid fibrils in Alzheimer's disease brain tissue. Cell *154*, 1257–1268.

Nieuwkoop, A.J., Franks, W.T., Rehbein, K., Diehl, A., Akbey, U., Engelke, F., Emsley, L., Pintacuda, G., and Oschkinat, H. (2015). Sensitivity and resolution of proton detected spectra of a deuterated protein at 40 and 60 kHz magic-angle-spinning. J Biomol NMR *61*, 161–171.

Pace, C.N., Fu, H., Lee Fryar, K., Landua, J., Trevino, S.R., Schell, D., Thurlkill, R.L., Imura, S., Scholtz, J.M., Gajiwala, K., et al. (2014). Contribution of hydrogen bonds to protein stability. Protein Science *23*, 652–661.

Pines, A. (1972). Proton-Enhanced Nuclear Induction Spectroscopy. A Method for High Resolution NMR of Dilute Spins in Solids. J. Chem. Phys. *56*, 1776.

Poornima, C.S., and Dean, P.M. (1995). Hydration in drug design. 1. Multiple hydrogen-bonding features of water molecules in mediating protein-ligand interactions. Journal of Computer-Aided Molecular Design *9*, 500–512.

Qiang, W., Yau, W.-M., Luo, Y., Mattson, M.P., and Tycko, R. (2012). Antiparallel β-sheet architecture in Iowa-mutant β-amyloid fibrils. Proc Natl Acad Sci USA *109*, 4443.

Reif, B. (2012). Ultra-high resolution in MAS solid-state NMR of perdeuterated proteins: Implications for structure and dynamics. Journal of Magnetic Resonance *216*, 1–12.

Schütz, A.K., Soragni, A., Hornemann, S., Aguzzi, A., Ernst, M., Böckmann, A., and Meier, B.H. (2011). The Amyloid-Congo Red Interface at Atomic Resolution. Angew. Chem. Int. Ed. *50*, 5956–5960.

Shahid, S.A., Bardiaux, B., Franks, W.T., Krabben, L., Habeck, M., van Rossum, B.-J., and Linke, D. (2012). Membrane-protein structure determination by solid-state NMR spectroscopy of microcrystals. Nat. Methods *9*, 1212–1217.

Steitz, T.A. (1990). Structural studies of protein–nucleic acid interaction: the sources of sequence-specific binding. Quart. Rev. Biophys. *23*, 205–280.

Struppe, J., Quinn, C.M., Lu, M., Wang, M., Hou, G., Lu, X., Kraus, J., Andreas, L.B., Stanek, J., Lalli, D., et al. (2017). Expanding the horizons for structural analysis of fully protonated protein assemblies by NMR spectroscopy at MAS frequencies above 100 kHz. Solid State Nuclear Magnetic Resonance *87*, 117–125.

Tuttle, M.D., Comellas, G., Nieuwkoop, A.J., Covell, D.J., Berthold, D.A., Kloepper, K.D., Courtney, J.M., Kim, J.K., Barclay, A.M., Kendall, A., et al. (2016). Solid-state NMR structure of a pathogenic fibril of full-length human α-synuclein. Nat. Struct. Mol. Biol. *23*, 409–415.

Wasmer, C., Lange, A., Van Melckebeke, H., Siemer, A.B., Riek, R., and Meier, B.H. (2008). Amyloid fibrils of the HET-s(218-289) prion form a beta solenoid with a triangular hydrophobic core. Science *319*, 1523–1526.

Zhou, D.H., Nieuwkoop, A.J., Berthold, D.A., Comellas, G., Sperling, L.J., Tang, M., Shah, G.J., Brea, E.J., Lemkau, L.R., and Rienstra, C.M. (2012). Solid-state NMR analysis of membrane proteins and protein aggregates by proton detected spectroscopy. J Biomol NMR *54*, 291–305.

3

DIRECT OBSERVATION OF PROTON EXCHANGE IN A PROTON PUMP

3.1 Synopsis

Detecting protons by NMR not only gives access to spatial information at atomic resolution, but also potentially allows to study their dynamic behavior, i.e. chemical exchange processes of protons. Such dynamics can be assessed using exchange spectroscopy in which chemical exchange is detected as cross peaks in multidimensional NMR spectra. Under solid-state MAS conditions, however, cross peaks can be also due to spin diffusion processes in such exchange spectra. In addition to reasons of improving spectral resolution, it is therefore important to apply high MAS frequencies and deuteration when observing exchangeable protons.

In the current chapter, a study of proton exchange processes in the pore of the light-driven proton pump bacteriorhodopsin (BR) is presented. The protein is studied in the purple membrane, its native environment. BR is an ideal model system to investigate such processes as it relocates protons across the membrane out of the *Halobacterium* cell. During this process, several amino acid side chains and the Schiff base of the retinal chromophore change their protonation states. To investigate proton exchange processes at the key residues D85, D96 and R82, proton detected ^{1}H–^{1}H exchange spectroscopy is applied. Since a number of water molecules are involved in the proton transport, we use a water suppression method that preserves the water proton magnetization. This allowed us to investigate proton exchange between the carboxyl and guanidinium groups of theses residues and water. For D96, we find a proton exchange with water. Interestingly, in the crystal structure solved at 100 K the next water molecule is about 5 Å distant from the D96 carboxyl group, making a proton exchange very unlikely. Therefore, we conclude that either this water molecule is highly dynamic at room temperature or additional water molecules provide the possibility for a long-range Grotthuss-type proton exchange pathway at this site. We also studied D85 and R82, for which we observe proton delocalization with water molecules. Even though D85 is deprotonated in the BR ground-state, a proton is delocalized between its carboxyl group and water. In addition, a proton exchange is observed between this site and the guanidinium moiety of R82 via water molecules. This suggests the involvement of R82 in the proton transport during the BR photocycle.

The current chapter highlights the great potential of proton-detected solid-state NMR combined with fast MAS in protonation dynamics studies. It allows to investigate protonation states and their dynamic changes, and it can be applied to a large variety of proteins including membrane proteins.

3.2 Personal contribution

I recorded NMR spectra of BR-wildtype, BR-D96N, BR-D85T and BR-R82Q, analyzed the data and was involved in writing the manuscript. All BR samples were expressed and purified by Thi Bich Thao Nguyen.

Daniel Friedrich, Peter Hegemann and Hartmut Oschkinat designed the study; Daniel Friedrich, Andrew J. Nieuwkoop and Florian Brünig performed research; Daniel Friedrich, Florian Brünig, Roland R. Netz and Hartmut Oschkinat analyzed data; Daniel Friedrich wrote the manuscript with contributions from Florian Brünig, Roland R. Netz, Peter Hegemann and Hartmut Oschkinat.

3.3 Manuscript in Preparation

Daniel Friedrich, Andrew J. Nieuwkoop, Florian Brünig, Roland R. Netz, Peter Hegemann, and Hartmut Oschkinat:
'Direct Observation of Proton Exchange in a Proton Pump', *manuscript in preparation*

Direct Observation of Proton Exchange in a Proton Pump

Daniel Friedrich[1,2], Andrew J. Nieuwkoop[1,‡], Florian Brünig[3], Roland R. Netz[3], Peter Hegemann[4], and Hartmut Oschkinat[1,2,*]

[1] Leibniz-Forschungsinstitut für Molekulare Pharmakologie, Robert-Rössle-Str. 10, 13125 Berlin, Germany

[2] Freie Universität Berlin, Institut für Chemie und Biochemie, 14195 Berlin, Germany

[3] Freie Universität Berlin, Fachbereich Physik, 14195 Berlin, Germany

[4] Humboldt-Universität zu Berlin, Institut für Biologie, Invalidenstr. 42, 10115 Berlin, Germany

[‡] present address: Rutgers University, Department of Chemistry and Chemical Biology, 610 Taylor Road, Piscataway, NJ 08854, USA

* Correspondence should be addressed to oschkinat@fmp-berlin.de

Abstract

A variety of membrane proteins translocate protons, let them pass selectively or are driven by translocating protons, such as ATPases, ion channels, or rhodopsin-like proton pumps. Their inherent protonation dynamics plays an essential role in this process but it is difficult to observe by common structural methods. Since NMR detects protons directly, we introduce solid-state magic-angle-spinning (MAS) NMR as an attractive method for studying exchangeable protons and their dynamics, investigating key sites within the archaeal light-driven proton pump bacteriorhodopsin (BR) as an example. They comprise the Schiff base, D96, D85, R82, and close water molecules within its pore. We detect protons attached to the head groups of these three residues and study their exchange characteristics. Three mutants used for resonance assignment showed different protonation dynamics patterns, in accordance with alterations in their kinetics. The combination with *ab-initio* molecular dynamics simulations reveals proton delocalization between D85 and H_2O in the BR dark-state. The protonated D96 exchanges its proton much less frequent with H_2O hydrogens, which in addition is found to require a dynamic behavior of water molecules at the proton uptake site in BR. An exchange signal between D85 and R82 suggests a proton path between them. Our study provides insight into the relation of protonation dynamics and active proton pumping, suggesting that NMR at fast MAS will be the method of choice in further investigations of proton translocating membrane protein systems.

Introduction

The principle of protonation dynamics exhibits several features of protons which are regulating how proteins function (Karplus and Kuriyan, 2005). It includes the movement of protons between neighboring groups (shift of a proton in a hydrogen bond), the relocation of protons between H_2O molecules and amino acid side chains that can be protonated, and long-range proton transfer processes. To enable these features, networks of hydrogen-bonds between H_2O molecules and the protein must be rearranged (Freier et al., 2011). This may require conformational changes of amino acids or even secondary structure elements. In general, understanding the regulatory principle of protonation dynamics requires the possibility to measure changes in protonation states. To establish an experimental approach to investigate such dynamics in membrane proteins, we employ direct detection of protons using fast magic-angle-spinning (MAS) solid-state NMR spectroscopy. Sufficient spectral resolution in proton-detected experiments can be achieved by using high MAS frequencies (> 40 kHz), especially when combined with deuteration of the protein followed by back-exchange of protons at labile position (Zhou et al., 2007; Kurauskas et al., 2016; Lakomek et al., 2017; Linser et al., 2011). The methodological progress in solid-state NMR has opened new possibilities in investigations of membrane proteins, fibrils and large biomolecular complexes (Baker and Baldus, 2014; Brown and Ladizhansky, 2015; Fitzpatrick et al., 2013; Lalli et al., 2017; Weingarth and Baldus, 2013). Protonation and deprotonation of individual amino acids can be investigated by time-resolved infrared spectroscopy (rapid scan and step scan) (Kötting and Gerwert, 2005; Radu et al., 2009). In many cases, however, vibrational bands are heavily overlapping and the attribution of

individual vibrations in the difference spectra is difficult and in most cases impossible. In this study, we use NMR exchange spectroscopy to elucidate proton exchange between amino acid side chains and water molecules (Zheng et al., 1993). The resulting homonuclear multi-dimensional correlations contain information about chemical exchange including the kinetics, but also continuous exchange of energy between the individual nuclear spins (spin diffusion). Due to limited spectral resolution, it is difficult to distinguish different water populations based on the ^{1}H chemical shift in ^{1}H-^{1}H exchange spectra. Therefore, resulting signals at the water frequency may contain contributions from the bulk water. Still, it is highly desirable to determine proton exchange processes between residues that can be protonated and H_2O molecules. Here we study such a process at the aspartic acids D85 and D96 as well as R82 in bacteriorhodopsin (BR). These residues show changes in their protonation states at the carboxylic acid and guanidinium moieties during the photocycle of this light-dependent proton pump (Freier et al., 2011). BR is an excellent model system to establish new approaches for determining chemical exchange of protons between amino acid side chains and H_2O molecules since both are involved in the proton transport pathway (Figure 1A). Recently, a time-resolved serial femtosecond crystallography study using an X-ray free electron laser revealed structural changes and repositioning of water molecules during the BR photocycle (Nango et al., 2016). This allows conclusions about potential proton transport in BR, however, the direct detection of protons and their exchange behavior was not possible so far.

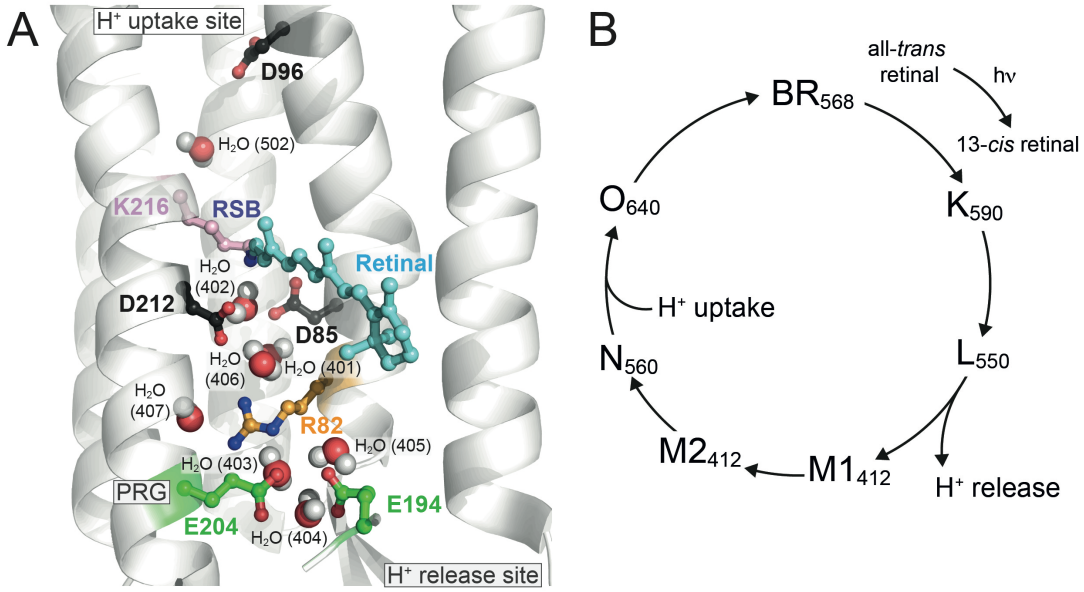

Figure 1. The light-driven proton pump bacteriorhodopsin (BR, PDB 1C3W (Luecke et al., 1999)). (A) The proton transport pathway in BR involves the aspartic acids D96, D85, the retinal Schiff base (RSB), R82 and the proton release group (PRG) with the glutamic acids E194 and E194 constituting the extracellular H^+ release site. **(B)** The photocycle of BR (Mak-Jurkauskas et al., 2008; Neutze et al., 2002; Wickstrand et al., 2015).

During its photocycle, BR relocates in a non-consecutive transport step a single proton across the membrane out of the *Halobacterium salinarum* cell (Figure 1B). After absorption of a photon, the retinal chromophore isomerizes from an all-*trans* configuration to 13-*cis* during the transition from BR_{568} dark-state to the K_{590} intermediate. This K state, however, comprises a not fully rotated chromophore (Shim et al., 2009). The reaction is followed by a relaxation of retinal into the fully rotated 13-*cis* conformer (L_{550}-state) and a subsequent relocation of the retinal Schiff base (RSB) proton to the carboxylic acid of the D85 side chain. This is caused by a drastic pK drop of the RSB and an increase of the D85 pK (Lanyi and Schobert, 2007). Protonation of D85 initiates an outward movement of R82 and a decrease in

pK of the proton release group (PRG), consisting of E194, E204 and a trimeric water cluster (H_2O 403, 404 and 405), resulting in a proton release into the extracellular bulk phase ($L_{550} \rightarrow M1_{412}$) (Bashford and Gerwert, 1992; Garczarek et al., 2005; Spassov et al., 2001). After reorientation of Helix F and large structural changes ($M1_{412} \rightarrow M2_{412}$), water is invading into the intercellular proton channel and the RSB is reprotonated from D96 via a transient water chain visualized as $M2_{412} \rightarrow N_{520}$ transition. Protonation of the RSB reduces the pK of D85 and its proton is transferred to the proton release group (PRG) ($N_{520} \rightarrow O_{640}$). However, it remained unclear whether this late proton transfer involves deprotonation and reprotonation of R82 (Hutson et al., 2000). The photocycle is complemented by restoring the initial all-*trans* configuration of the retinal by thermal relaxation ($O_{640} \rightarrow BR_{568}$) (Lanyi, 2004). The key steps of this global proton relocation process across the membrane are only possible through the involvement of H_2O molecules (Gerwert et al., 2014; Kandori, 2000). This is especially true for the proton movement from D96 to the RSB but also for the proton release from D85 towards the PRG (Figure 1).

Therefore, the chemical exchange of protons from carboxylic moieties of an aspartic acid with H_2O molecules is crucial for the molecular operation of BR. To gain further insights into the underlying proton exchange processes, we aim to characterize such chemical exchanges site-specifically. In addition, the role of R82 in the proton transport mechanism must be elucidated in more detail because time-resolved infrared spectroscopy for this residue is not available. To characterize and finally understand the proton relocation pathway from D85 to the PRG during the photocycle, we investigate the protonation state of the R82 side chain and its exchange behavior to H_2O and the carboxylic moiety of D85.

To study the delocalization of exchangeable protons in the BR dark-state and to help understanding the role of R82, D96 and D85 in the proton transport mechanism of BR, we use deuterated and ^{13}C,^{15}N-labeled purple membranes. We applied high MAS frequencies (40 kHz and 60 kHz) after re-introducing protons during illumination of the samples and collected proton-detected solid-state NMR exchange spectra (Zheng et al., 1993). This approach facilitates the detection of proton delocalization and the underlying exchange measured in the BR dark-state. Therefore, it may inform on contributions of the chemical sites involved in the global proton relocation process. To help interpreting the exchange signals observed, we performed *ab-initio* molecular dynamics simulations that allow estimating the proton distribution between a H_2O molecule and a carboxylic moiety. This approach enabled us to conclude about the exchange behavior of protons at amino acid side chains with H_2O molecules in the core of the protein, even when measuring the samples in the dark.

Results and Discussion

Detectability of protons in deuterated BR by solid-state MAS NMR

The experimental procedure chosen makes different sites accessible by proton-detected solid-state MAS NMR spectroscopy (Figure 2A). If the sample is not back-exchanged, no signals can be expected in such experiments (Figure 2A, *top left*). After re-introducing protons at exchangeable positions, one should observe signals from the amides in the protein backbone (Figure 2A, *top right*), at least when the position is solvent accessible – which is limited in membrane proteins (Lalli et al., 2017; Ward et al., 2011). In addition to these sites, exchangeable protons at side chains of residues that are involved in proton pumping (glutamate, aspartate and arginine) should give rise to NMR resonances as well since the back-exchange was performed during illumination (Figure 2A, *bottom left* and *right*). In BR, these residues include R82 and the two aspartic acids D85 and D96.

To monitor the efficiency of the back-exchange of protons, we recorded a ^{1}H based two-dimensional ^{15}N-^{1}H correlation using cross polarization (CP) (Figure 2B) (Chevelkov et al., 2003; Zhou et al., 2007). The spectrum contains approximately 70 signals corresponding to amides of the protein backbone. This means only about 28% of the backbone amides in BR are detectable due to limited solvent accessibility. By recording a set of three-dimensional experiments allowing a sequential backbone walk ((H)CANH, (H)CA(CO)NH, (H)CONH, (H)COCANH, (H)CBCANH), (H)CBCA(CO)NH) (Barbet-Massin et al., 2014), we could assign approximately 50% of the signals observed in the ^{15}N-^{1}H correlation through establishing sequential connections. These signals correspond to amides in the loops or in solvent accessible amino acids of the α-helices as it is often seen in ^{1}H

detecting solid-state MAS NMR studies of deuterated membrane proteins (Lalli et al., 2017; Ward et al., 2011). However, not all loop regions show signals in our spectra. This may be attributed to high conformational flexibility of these regions causing disappearance of their amide backbone signals in CP-based experiments (Andronesi et al., 2005).

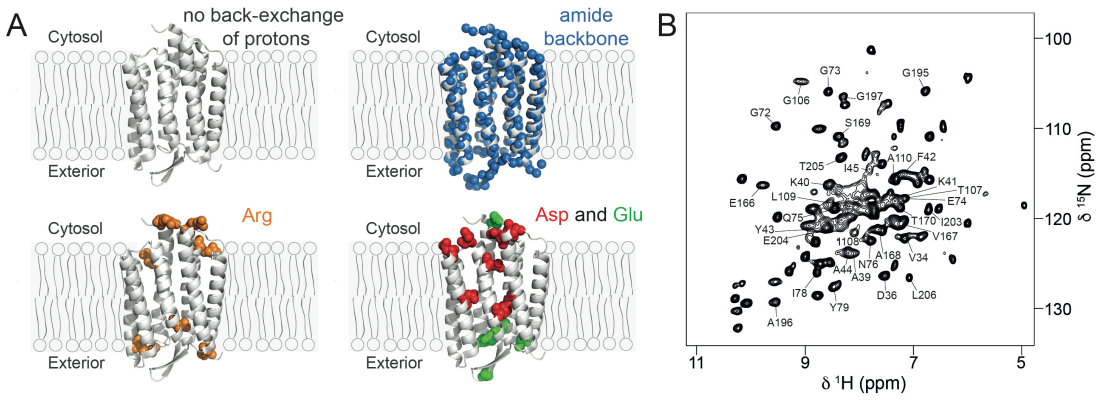

Figure 2. Accessibility of sites in bacteriorhodopsin (PDB 1C3W) by proton-detected solid-state MAS NMR. (A) After introducing protons into the sample during illumination, signals of the backbone amides (*blue*), arginine side chains (*orange*) and carboxylic protons in aspartic and glutamic acids (*red* and *green*) in the core of the protein can be expected. **(B)** Proton-detected two-dimensional ^{15}N-^{1}H correlation spectrum of BR in the purple membrane. Signals that could be assigned after performing a sequential backbone walk are labeled.

In addition to amides, exchangeable sites in the functionally relevant side chains of D85, D96 and R82 are expected to be accessible with proton-detected solid-state NMR at high MAS frequencies. Using exchange spectroscopy under such conditions, the proton exchange between individual amino acids and water molecules can be detected. However, chemical exchange is not the only mechanisms contributing to

signals observed in such spectra. They may also partially result from spin diffusion processes.

Assessment of exchangeable protons at R82, D85 and D96 side chains

The protonation state and chemical exchange behavior of protons at the guanidinium group of R82 and the two aspartic acids D96 and D85 is of specific interest with respect to the proton transport mechanism of BR. To probe the proton relocation between the carboxylic groups of D96, D85 and the guanidinium group of R82 with H_2O molecules, we performed exchange spectroscopy experiments under MAS conditions (Figure 3) (Zheng et al., 1993). To enable the assignment of the protons, we recorded two-dimensional ^{13}C-^{1}H (Figure 3A), ^{15}N-^{1}H spectra (Figure 3B) and ^{1}H-^{1}H correlations (Figure 3C) of both BR wildtype and the mutants D96N, D85T and R82Q. We acquired the latter using the jump-and-return water suppression with the 1-1 hard pulse scheme allowing the observation of water protons (Clore et al., 1983). In proton-detected MAS NMR, the proton magnetization of water is usually suppressed with very efficient techniques such as MISSISSIPPI (Zhou and Rienstra, 2008). Here, water protons are of specific interest and their magnetization needs to be preserved to allow the observation of the H_2O proton NMR signal. This can be achieved by applying the water suppression called jump-and-return.

Using the BR mutant D96N (Figure 3A and 3C, *blue* spectra), the signal at 11.0 ppm ^{1}H chemical shift can be assigned to the carboxylic proton D96–$H^{\delta 2}$. This is also confirmed by the heteronuclear ^{13}C-^{1}H correlation involving the C^{γ} chemical shifts of aspartic acids (Figure 3A). The carboxylic proton of D96 also shows a cross peak at

the water frequency resulting from its chemical exchange to H_2O (Figure 3C, *black* spectrum).

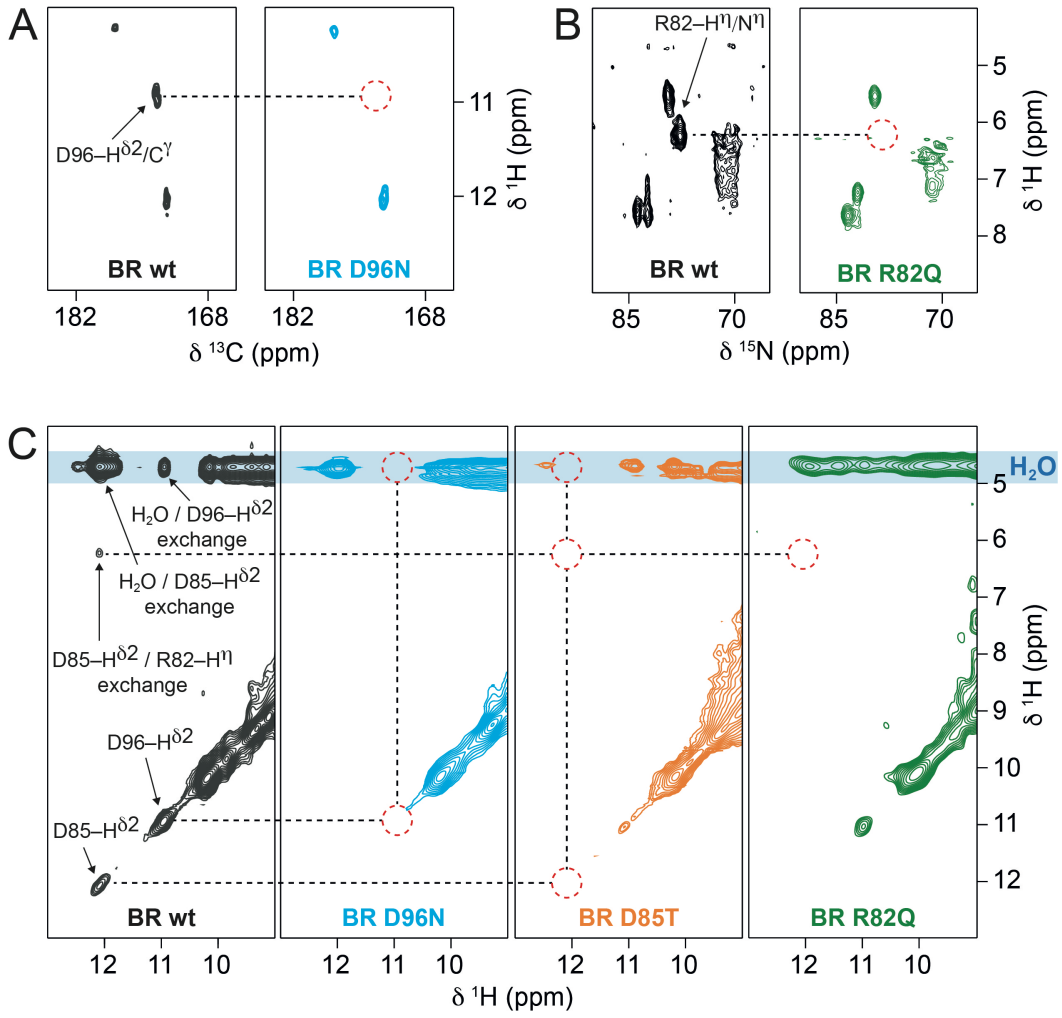

Figure 3. Protonation state and chemical exchange of R82, D96 and D85 with H_2O in bacteriorhodopsin (BR) probed by proton-detected solid-state MAS NMR. (A) ^{13}C-^{1}H correlations of BR wildtype (wt, *black* spectrum) and the mutant D96N (*blue* spectrum). **(B)** ^{15}N-^{1}H correlations of BR wildtype (wt, *black* spectrum) and the mutant R82Q (*green* spectrum). **(C)** ^{1}H-^{1}H exchange spectra of BR wildtype (wt, *black* spectrum), D96N (*blue* spectrum), D85T (*orange* spectrum) and R82Q (*green* spectrum). The mutants are used to assign the signals of D96–$H^{\delta2}$ (11.0 ppm), D85–$H^{\delta2}$ (12.1 ppm) and R82–H^{η} (6.2 ppm). *Red dashed* circles indicate missing signals resulting from mutations that allow the assignment.

The exchangeable proton of the R82 guanidinium group, R82–H^{η}, can be assigned to the signal at 6.2 ppm ^{1}H chemical shift as it disappears in the ^{15}N-^{1}H spectrum of blue membrane with the BR mutant R82Q (Figure 3B). It shows a weak cross peak to D85–$H^{\delta 2}$ in the BR wt spectrum (Figure 3C, *black* spectrum) which may reflect a long-range proton exchange between the carboxylic group of D85 and the guanidinium group of R82 via the water molecules 401 and 406 (see Figure 1). This finding indicates that the R82 guanidinium group must be involved in the proton relocation from D85 towards the proton release group during the photocycle.

Based on the spectrum of the D85T mutant (Figure 3C, *orange* spectrum), the signal at 12.1 ppm ^{1}H chemical shift in the wildtype spectrum (Figure 3C, *black* spectrum) can be assigned to D85–$H^{\delta 2}$. At this frequency neither a diagonal peak nor any cross signals can be detected in the D85T spectrum which shows that this resonance corresponds to D85–$H^{\delta 2}$. However, the diagonal signal of D85–$H^{\delta 2}$ at 12.1 ppm also disappears in the two other mutants D96N and R82Q. But, the proton exhibits a cross peak at the water frequency (12.1 ppm in F1 and 4.8 ppm in F2) only. Therefore, this proton must be located predominantly at a water molecule and much rarely at the D85 carboxyl group in these two mutants. This can be explained by a change in kinetic of the proton delocalization between the carboxyl group of D85 and H_2O in both the D96N and R82Q mutants. Similar to D96–$H^{\delta 2}$, also D85–$H^{\delta 2}$ exhibits an exchange peak to H_2O. Consequently, this proton exchanges chemically with H_2O. In contrast to D96–$H^{\delta 2}$, the exchange peak of D85–$H^{\delta 2}$ at the water frequency has a much higher intensity as the corresponding diagonal peak as described above. This suggests that the localization of this proton is in favor of the chemical environment of water. The underlying mechanism could be a proton shift within the hydrogen bond between the D85 carboxyl group and a water molecule close to it.

In conclusion, both the D85 and D96 carboxylic groups show chemical exchange of protons with H_2O in the BR dark-state upon illumination as seen after $^{1}H/^{2}H$ back-exchange. In addition, a weak exchange signal is observed between D85 and R82. Illumination allowed protons to enter the pore of BR via exchangeable sites involved in the proton relocation pathway. We therefore conclude that in both cases (D85 and D96) a proton is delocalized between the carboxylic group and water.

The carboxyl group of D85 exchanges a proton with H_2O in the BR dark-state

Under the experimental conditions chosen, we assume BR to be fully in its light-adapted dark-state (BR_{568} after lighting off) with retinal completely in the C13=C14 *trans*, C15=N *anti* conformation and three stored protons that become involved in the proton transport mechanism after the next light absorption. They are proposed to be located at the RSB, the carboxylic group of D96 and the H_2O cluster coordinated with E194 and E204 in the proton release group (Gerwert et al., 2014; Lórenz-Fonfría et al., 2017). Interestingly, our findings suggest that D85 is exchanging a proton with H_2O in the BR even in the dark. After a long discussion in the literature, the combination of isotope labeling, mutagenesis and infrared spectroscopic studies identified D85 as the residue that out of the four internal aspartates 85, 96, 115 and 212 is the only deprotonated one in darkness (Eisenstein et al., 1987; Mogi et al., 1988; Rothschild et al., 1981). However, only time-resolved spectroscopy revealed that D85 is the acceptor of the RSB proton. But already in the dark-state, a proton near the carboxylic group of D85 is confirmed by the C^{γ}–$H^{\delta 2}$ cross peak of D85 in the heteronuclear dipolar based ^{13}C-^{1}H correlation reporting on through-space interactions between ^{13}C and ^{1}H nuclei (Figure 3A). This proton is delocalized

306 between the carboxylic group of D85 and the H_2O molecules 401 and 402 as shown
307 in the exchange spectra (Figure 3C).
308 To estimate the delocalization of such a proton, we computed from simulations the
309 equilibrium distribution in a simplified configuration (Figure 4). The model consists
310 of one H_2O molecule located between two carboxylic groups with one excess proton
311 (Figure 4A). Such a system reflects the cluster of the water molecule 402 coordinated
312 with D212 and D85 in BR (Figure 5A). The *ab-initio* molecular dynamics
313 simulations were performed using the CP2K 2.4 environment and a TZV2P basis set
314 with the BLYP exchange correlation functional (Becke, 1988; Hutter et al., 2014;
315 VandeVondele and Hutter, 2007). Depending on the distance between a carboxylic
316 group oxygen atom and the water oxygen ($R_{O_C O_W}$), the relative proton position,
317 described by an asymmetry coordinate ($R_{O_C H} – R_{O_W H}$, Figure 4A), differs. Note that a
318 negative asymmetry refers to a localization near the carboxylic oxygen, and a
319 positive asymmetry to the water oxygen. For $R_{O_C O_W}$ of 2.4 – 2.6 Å, intermediate
320 proton localizations are also occupied (Figure 4B), i.e. a proton exchange is observed
321 in the time-resolved trajectories. The energy required to delocalize a proton between
322 a carboxylic oxygen atom and the water oxygen within 0.5 Å corresponds to about
323 2.5 k_BT (Figure 4C). Similarly, Eckert and Zundel suggested a 6 k_BT barrier for a
324 fixed $R_{O_C O_W}$ of 2.65 Å from *ab-initio* SCF calculations (Eckert and Zundel, 1988). In
325 the case of D85, $R_{O_C O_W}$ is 2.6 Å as measured in the crystal structure solved at
326 cryogenic temperatures (100 K) (PDB 1C3W (Luecke et al., 1999) and Figure 5A).
327 In contrast to such low temperatures, the proton exchange observed here by NMR is
328 detected at room temperature. Consequently, the water molecules must be considered
329 less rigid as in this crystal structure and therefore a shorter distance $R_{O_C O_W}$ for D85
330 and H_2O 401 or 402 is possible as well. Such a high mobility of these water

molecules is in well agreement with molecular dynamic simulations of the group of Gerwert (Kandt et al., 2004). The mobility of water molecules in BR was also observed by time-resolved serial femtosecond crystallography (Nango et al., 2016).

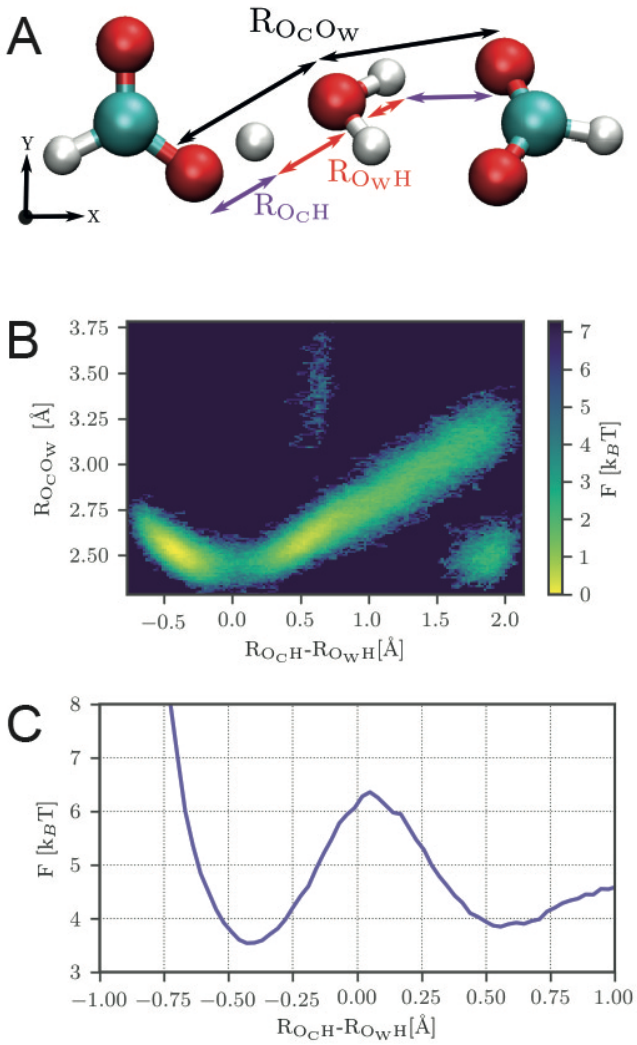

Figure 4. Definition of the localization of the protons in a cluster of one H_2O molecule and two carboxyl groups. The distance between a carboxylic group oxygen atom and the water oxygen ($R_{O_C O_W}$) and a proton's relative asymmetry with respect to the two oxygens ($R_{O_C H}$–$R_{O_W H}$) is used as coordinates, inspired by Marx et al. (Marx et al., 1999). **(A)** The thermal energy of the proton localization as a function of the coordinates, defined in (A). **(B)** The localization of the protons along the asymmetry coordinate ($R_{O_C H}$–$R_{O_W H}$).

The *ab-initio* simulation of proton distribution between a carboxylic moiety and a H_2O molecule supports the notion that a proton is exchanged between D85 and water. This delocalized proton gives rise to the NMR signal reflecting a D85–$H^{\delta 2}$ resonance as described above (Figure 3C, *black* spectrum).

In addition to the observed proton exchange between D85 and H_2O, it was conceivable that also the RSB proton is delocalized in a dynamic proton exchange network in the BR dark-state (Figure 5A). The RSB proton is expected to show a signal in a dipolar-based ^{15}N-^{1}H correlation involving the RSB nitrogen resonance. The RSB nitrogen signal could be observed at 100 K in the spectral region of 165 – 175 ppm for the BR dark-state (Mak-Jurkauskas et al., 2008). In a similar experimental approach, the signal of the RSB proton itself could be detected at around 100 K recently (Ni et al., 2018). In the room temperature proton-detected spectra presented here, however, we could not observe such a proton resonance. This may be attributed to a delocalization of the RSB proton in the BR dark-state. The rate of the underlying exchange process of such a proton delocalization can lead to disappearance of the proton signal in NMR spectra at room temperature. It is possible that the RSB proton is delocalized with H_2O (402) (Figure 5A), and its exchange is coupled to the proton delocalization between D85 and H_2O. However, the high and low proton affinities of the RSB (pKa 13.3) and D85 (pKa 2.2), respectively, still hinder the directed proton transport towards the release site between these two moieties (Chang et al., 1988; Sheves et al., 1986).

The limited spectral proton resolution of the H_2O resonances does not allow to distinguish between the two H_2O molecules 401 and 402 that could be involved in the proton exchange of D85. Both molecules have the same distance of 2.6 Å to D85–$O^{\delta 2}$ and form a pentameric hydrogen bond arrangement together with D85,

D212 and H_2O (406) (Figure 5A) (Gerwert et al., 2014; Luecke et al., 1999). Based on the detected D85–$H^{\delta 2}$ and the observed proton exchange, the protonation states of this cluster should be revisited. We suggest considering the protonation state of D85 and the neighboring H_2O molecules as dynamic with a delocalized proton between D85 and H_2O in the BR dark-state.

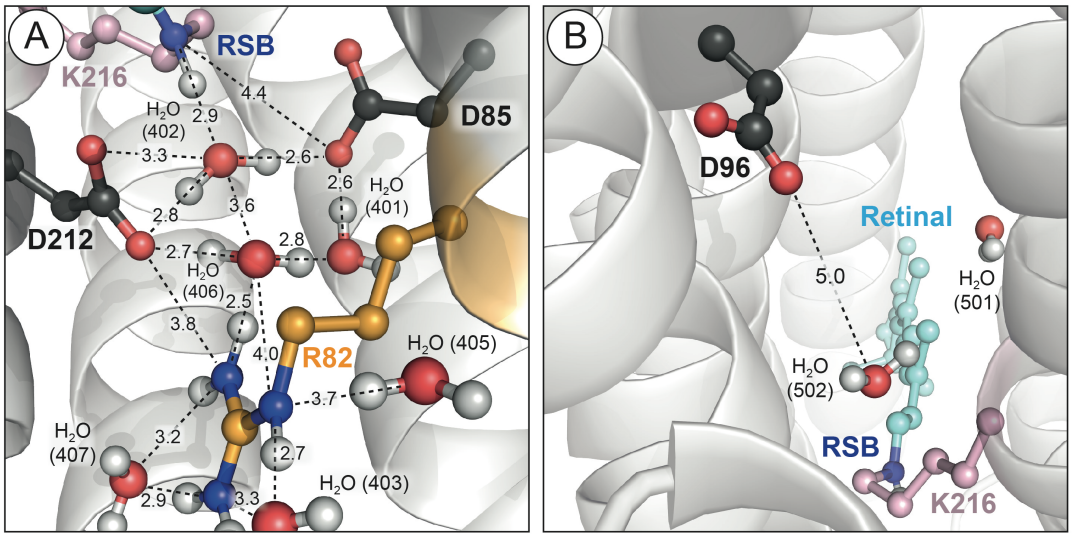

Figure 5. Structural view of D85 and D96 in the BR dark-state crystal structure (PDB 1C3W (Luecke et al., 1999), dashed lines indicate distances in Å). (A) The carboxyl group of D85 is near the H_2O molecules (401) and (402). **(B)** The distance of H_2O (502) to the D96 carboxyl group is longer than the D85–H_2O distances.

R82 shows proton exchange with H_2O and D85

Based on the crystal structure and spectroscopic studies, the guanidinium group of R82 is involved in a hydrogen bonding network with water molecules and the carboxyl group of D85. It acts as a regulator of the D85 pK_{app}, but a transient deprotonation of R82 has neither been unequivocally observed nor excluded (Figure 5A and (Hutson et al., 2000; Shibata et al., 2003; Vogt et al., 2015)). The weak

exchange signal correlating the R82–H^{η} and the D85–$H^{\delta 2}$ suggests a chemical proton exchange within this network, presumably via the water molecules 401 and 406 seen in the 100 K crystal structure (Figure 3C (*black* spectrum), Figure 5A and Luecke et al., 1999). To further elucidate the role of R82, the proton transfer from the guanidinium group of R82 towards the PRG had to be investigated. To address this further, studying the R82 protonation state in the O_{640} intermediate might prove instrumental. After retinal isomerization upon light reception, the underlying equilibrium of the exchange between R82 and D85 might be shifted towards the protonated form of D85 during the $L_{550} \rightarrow M1_{412}$ transition compared to the dark-state. This change in equilibrium could be facilitated by the structural changes detected by time-resolved serial X-ray crystallography (Nango et al., 2016). Based on the observed protonated form of R82 (Figure 3B), the guanidinium group of this amino acid must be involved in the proton transport mechanism. The solid-state MAS NMR exchange spectra show a delocalization of R82–$H^{\delta 2}$ in the dark-state (Figure 3C) which indicates the possibility of R82 deprotonation in the $L_{550} \rightarrow M1_{412}$ transition.

D96–H_2O proton exchange indicates a dynamic behavior of water molecules at room temperature

In contrast to the finding concerning D85, the detected protonation of D96 in the BR dark-state agrees well with previously obtained results (Gerwert et al., 2014). D96 serves as the central binding position in the H^+ uptake site in conjunction with H_2O molecules located at the cytoplasmic entry of the protein pore. It has been reported that the D96–$H^{\delta 2}$ is relocated via a transiently established chain of three water

molecules to the RSB in a Grotthuss-type mechanism in the $M_{412} \rightarrow N_{520}$ transition (Freier et al., 2011). In the dark-state of BR, such a water chain was not detected so far and the next H_2O molecule (H_2O (502)) on the proton transport pathway towards the RSB has a distance of 5.0 Å to the D96–$O^{\delta 2}$ as measured in the crystal structure solved at 100 K (Figure 5B) (Luecke et al., 1999). A proton exchange mechanism crossing such a long distance is unlikely. Thus, we conclude that the water molecule 502 in the BR_{568} state must be highly dynamic at room-temperature in contrast to the situation observed in the crystal structure solved at cryogenic temperatures. The possibility of a proton delocalization between D96 and water molecules at the cytoplasmic entry site of the BR pore can be largely excluded due to low water accessibility in the dark-state (Kandt et al., 2004). Therefore, it presumably results from a dynamic water molecule positioned at the other side of D96, towards the RSB. The existence of additional water molecules at this site, although not observed in the crystal structure at 100 K, may lead to a reduced distance between the D96 carboxylic group and the next water molecule. Such additional water molecules represent another possible explanation for the proton exchange observed between these sites. In any case, the D96–$H^{\delta 2}$ can exchange with a water molecule in the dark-adapted BR_{568} state. However, to prove the proton transport experimentally from D96 in the direction of the RSB during the $M2_{412} \rightarrow N_{520}$ transition via the transient water line bridging the 5.0 Å distance, further investigations are required. Such an elucidation could be complemented by using proton-detected solid-state NMR focusing on the stabilized N_{520} intermediate in which the water chain is formed. This could be accomplished by using the BR mutant V49A (Schobert et al., 2003).

Conclusions

In summary, we have directly observed chemical exchange of protons at key positions in the proton transport pathway of BR using ^{1}H detection by fast MAS solid-state NMR. This approach allowed us to measure proton exchange processes in the native environment of the protein, the purple membrane. Our results suggest chemical exchange of the D85 proton with H_2O in the dark-adapted BR_{568}. The possibility of such a delocalized proton between H_2O and a carboxylic group is corroborated by *ab-initio* molecular dynamics simulations. At the proton uptake site, D96 shows a proton delocalization with H_2O in BR_{568} indicating either the water 502 to be highly dynamic or the existence of additional water molecules between D96 and the RSB in dark-adapted BR_{568}. In addition, our findings suggest that the guanidinium group of R82 is involved in the proton transport mechanism of BR. It shows a proton exchange to the carboxylic group of D85 in dark-adapted BR indicating the possibility of a change in the R82 protonation state during the photocycle. Our study establishes a new approach to observe proton exchange in membrane proteins that can be directly extended to all targets of solid-state MAS NMR. Therefore, we expect this method to have a great impact in research of protonation dynamics within membrane proteins in the near future.

Material and Methods

Preparation of $^{2}H,^{13}C,^{15}N$-labled purple membrane

For production of purple membranes of bacteriorhodopsin, the *Halobacterium salinarum* strains BR-wildtype, BR-R82Q, BR-D85T and BR-D96N from Janos Lanyi, Dieter Oesterhelt and Markus Lange, Actilor GmbH were used. The following procedures were the same for all four strains. Cells were grown in deuterated celtone medium for at least 10 days at 37°C at 100 rpm in shaking flasks, after pre-culturing in protonated medium. In 200 mL, the sterile filtered medium contained, both in deuterated and protonated form: 1 g $^{13}C,^{15}N$-celtone, 50 g NaCl, 0.4 g KCl, 4 g $MgSO_4$, 0.04 g $CaCl_2$, 0.6 g Na-citrate ($C_6H_5Na_3O_7*2H_2O$), 0.4 mg Biotin, 0.4 mg Thiamin, 0.06 µg $MnSO_4$, 0.72 µg $FeCl_2$, 0.088 µg $ZnSO_4$ and 0.01 µg $CuSO_4$ at pH 7. Cells were harvested at 7,000 rpm for 20 min at 4 °C in a Beckman JLA 8.1 rotor with 1 L tubes. The supernatant was discarded and cells were resuspended in 6 mL basal salt (250 g/L NaCl, 20 g/L $MgSO_4*7H_2O$ and 2 g/L KCl at pH 7). After adding DNAse (grade II) and 65 mL H_2O, the cell suspension was dialyzed over night at 4 °C against H_2O under stirring. Membranes were then collected via centrifugation for 60 min at 40,000 rpm and 4 °C with a Sorvall 90SE ultracentrifuge using a 45Ti rotor. 3 mL of 50 mM Tris-HCl at pH 7.4 were used to resuspend the pellet, and the membranes were homogenized and fractionated by density gradient centrifugation using saccharose (30% – 70%) for 14 hours at 22,000 rpm and 15 °C with a Sorvall 90SE ultracentrifuge using a TST-28 rotor. The purple membrane fraction was collected and concentrated for 1 hour at 40,000 rpm and 4 °C with a Sorvall 90SE ultracentrifuge using a 45Ti rotor. After washing with 50 mM Tris-HCl

489 at pH 7.4, followed by homogenization and concentrating again (this procedure was
490 performed twice), the purple membranes were stored at -20°C.
491
492 *Sample preparation for NMR measurements*
493 The purple membranes were diluted in 90% / 10% $^{1}H_2O$ / $^{2}H_2O$ 50 mM Tris-HCl at
494 pH 7.4 to 0.01 OD and illuminated (a 595 nm filter was used) for 4 hours under
495 stirring in a water-cooled cuvette at 15 °C. The purple membranes were collected by
496 ultracentrifugation for 2 hours at 150,000 x *g* and 4 °C, and packed into 1.9 mm (for
497 40 kHz MAS experiments) or 1.3 mm (for 60 kHz MAS experiments) Bruker MAS
498 NMR rotors using home-made filling tools. Rotors were sealed with silicone rubber
499 disks to avoid loss of liquid during MAS.
500
501 *Solid-state MAS NMR measurements*
502 NMR experiments were performed on Bruker Avance III spectrometers with ^{1}H
503 Larmor frequencies of 800 MHz and 900 MHz using 1.3 mm triple-resonance (HCN)
504 and 1.9 mm four-channel (HCND) Bruker MAS probes, respectively. The variable
505 temperature was controlled using a Bruker cooling unit and adjusted to 260 K and
506 230 K for 60 kHz MAS experiments with the 1.3 mm probe and 40 kHz MAS
507 experiments with the 1.9 mm probe, respectively. According to external temperature
508 calibration, this corresponds to actual sample temperatures of 291 K for the 1.3 mm
509 probe and 293 K for the 1.9 mm probe.
510 In all experiments, cross polarization for heteronuclear magnetization transfers and
511 MISSISSIPPI solvent suppression was applied. (H)NH, (H)CANH, (H)CA(CO)NH,
512 (H)CONH, (H)CO(CA)NH, (H)CBCANH and (H)CBCA(CO)NH experiments were
513 recorded with pulse sequences according to Barbet-Massin et al., 2014 and

experimental parameters as used in Nieuwkoop et al., 2015. Tangential shapes were applied for heteronuclear cross polarization transfers. The $^{1}H–^{15}N$ and $^{1}H–^{13}C$ CP steps were optimized around $w_1^H = 3\omega_R/2$ and $w_1^X = 1\omega_R/2$. The $^{13}C–^{15}N$ specific CP transfers were optimized between $w_1^C = 3\omega_R/4$ and $w_1^C = 5\omega_R/4$, and $w_1^N = 1\omega_R/4$. For homonuclear ($^{13}C–^{13}C$) transfers, DREAM and INEPT was used at 40 kHz and 60 kHz MAS, respectively. WALTZ-16 was applied for ^{1}H, ^{13}C and ^{15}N decoupling during indirect evolution periods.

The $^{1}H–^{1}H$ exchange spectra were recorded at 40 kHz and 60 kHz MAS using a conventional z-exchange scheme with a mixing time of 10 ms. For water suppression, 1-1 hard pulses were applied just before detection. Both pulses were adjusted to 45°, separated by a delay of 45 μs corresponding to $1/4\upsilon_{max}$ (with υ_{max} being the difference in frequency of the protons of interest and the water protons).

The $^{1}H–^{13}C$ correlation spectrum was recorded at 40 kHz MAS with ^{13}C-detection using one CP transfer.

Ab-initio molecular dynamics simulations

In order to quantify the excess proton localization in the vicinity of a carboxyl group, *ab-initio* molecular dynamics (MD) simulations were performed in a model system, using the BLYP exchange-correlation functional and a TZVP basis set in the CP2K environment. The toy model system consists of a pair of deprotonated carboxyl molecules, as commonly assumed in a protein environment, with a water molecule and an excess proton in between as shown in Figure 4A. Note that this toy model agrees well with the crystal structure of bacteriorhodopsin shown in Figure 5A, which resolved a water molecule located right in between the D85 and D212 side chains. The simulation box size was optimized to be $15 \times 8 \times 8$ Å^3. The molecules

were kept near the central axis of the simulation box by constraining the carbon atoms in y and z direction using Lagrangian multipliers implemented in a Shake algorithm. In addition, the water oxygen atom is constraint by a quadratic potential of 2 $k_BT/Å$ in y and z direction to keep it close to the central axis as well. A 40 ps simulation was performed under NVT conditions at 300 K by coupling all atoms to a Nose-Hover chain of size three and decay time constant of 100 fs. Consequently, nine independent simulations (5 ps each) were performed under NVE conditions starting from different snapshots of the NVT data. The used trajectories stem from the NVE simulations. Distributions however are computed from both, NVT and NVE simulations, resulting in a total simulation time of 85 ps.

Acknowledgement

We thank Margrit Michalsky and Thi Bich Thao Nguyen for excellent technical assistance and production of purple membranes, and Janos Lanyi, Dieter Oesterhelt and Markus Lange, Actilor GmbH for the Halobacteria strains BR-R82Q, BR-D85T, and BR-D96N. Financial support by the Deutsche Forschungsgemeinschaft through SFB 1078 to Roland R. Netz, Peter Hegemann and Hartmut Oschkinat is kindly acknowledged.

References

Andronesi, O.C., Becker, S., Seidel, K., Heise, H., Young, H.S., and Baldus, M. (2005). Determination of Membrane Protein Structure and Dynamics by Magic-Angle-Spinning Solid-State NMR Spectroscopy. J. Am. Chem. Soc. *127*, 12965–12974.

Baker, L.A., and Baldus, M. (2014). Characterization of membrane protein function by solid-state NMR spectroscopy. Curr. Opin. Struct. Biol. *27*, 48–55.

Barbet-Massin, E., Pell, A.J., Retel, J.S., Andreas, L.B., Jaudzems, K., Franks, W.T., Nieuwkoop, A.J., Hiller, M., Higman, V., Guerry, P., et al. (2014). Rapid Proton-Detected NMR Assignment for Proteins with Fast Magic Angle Spinning. J. Am. Chem. Soc. *136*, 12489–12497.

Bashford, D., and Gerwert, K. (1992). Electrostatic calculations of the pKa values of ionizable groups in bacteriorhodopsin. Journal of Molecular Biology *224*, 473–486.

Becke, A.D. (1988). Density-functional exchange-energy approximation with correct asymptotic behavior. Phys. Rev. A *38*, 3098–3100.

Brown, L.S., and Ladizhansky, V. (2015). Membrane proteins in their native habitat as seen by solid-state NMR spectroscopy. Protein Sci *0*, 1–14.

Chang, C.H., Jonas, R., Govindjee, R., and Ebrey, T.G. (1988). Regeneration of blue and purple membranes from deionized bleached membranes of Halobacterium halobium. Photochem. Photobiol. *47*, 261–265.

596 Chevelkov, V., van Rossum, B.J., Castellani, F., Rehbein, K., Diehl, A., Hohwy, M.,
597 Steuernagel, S., Engelke, F., Oschkinat, H., and Reif, B. (2003). ^{1}H detection in
598 MAS solid-state NMR spectroscopy of biomacromolecules employing pulsed field
599 gradients for residual solvent suppression. J. Am. Chem. Soc. *125*, 7788–7789.

600 Clore, G.M., Kimber, B.J., and Gronenborn, A.M. (1983). The 1-1 hard pulse: A
601 simple and effective method of water resonance suppression in FT ^{1}H NMR. Journal
602 of Magnetic Resonance *54*, 170–173.

603 Eckert, M., and Zundel, G. (1988). Energy surfaces and proton polarizability of
604 hydrogen-bonded chains: an ab initio treatment with respect to the charge conduction
605 in biological systems. J. Phys. Chem. *92*, 7016–7023.

606 Eisenstein, L., Lin, S.L., Dollinger, G., Odashima, K., Termini, J., Konno, K., Ding,
607 W.D., and Nakanishi, K. (1987). FTIR difference studies on apoproteins. Protonation
608 states of aspartic and glutamic acid residues during the photocycle of
609 bacteriorhodopsin. J. Am. Chem. Soc. *109*, 6860–6862.

610 Fitzpatrick, A.W.P., Debelouchina, G.T., Bayro, M.J., Clare, D.K., Caporini, M.A.,
611 Bajaj, V.S., Jaroniec, C.P., Wang, L., Ladizhansky, V., Müller, S.A., et al. (2013).
612 Atomic structure and hierarchical assembly of a cross-β amyloid fibril. Proc. Natl.
613 Acad. Sci. U.S.A. *110*, 5468–5473.

614 Freier, E., Wolf, S., and Gerwert, K. (2011). Proton transfer via a transient linear
615 water-molecule chain in a membrane protein. Proc. Natl. Acad. Sci. U.S.A. *108*,
616 11435–11439.

617 Garczarek, F., Brown, L.S., Lanyi, J.K., and Gerwert, K. (2005). Proton binding
618 within a membrane protein by a protonated water cluster. Proc. Natl. Acad. Sci.
619 U.S.A. *102*, 3633–3638.

620 Gerwert, K., Freier, E., and Wolf, S. (2014). The role of protein-bound water
621 molecules in microbial rhodopsins. BBA - Bioenergetics *1837*, 606–613.

622 Hutson, M.S., Alexiev, U., Shilov, S.V., Wise, K.J., and Braiman, M.S. (2000).
623 Evidence for a perturbation of arginine-82 in the bacteriorhodopsin photocycle from
624 time-resolved infrared spectra. Biochemistry *39*, 13189–13200.

625 Hutter, J., Iannuzzi, M., Schiffmann, F., and VandeVondele, J. (2014). cp2k:
626 atomistic simulations of condensed matter systems. Wiley Interdisciplinary Reviews:
627 Computational Molecular Science *4*, 15–25.

628 Kandori, H. (2000). Role of internal water molecules in bacteriorhodopsin. Biochim.
629 Biophys. Acta *1460*, 177–191.

630 Kandt, C., Schlitter, J., and Gerwert, K. (2004). Dynamics of Water Molecules in the
631 Bacteriorhodopsin Trimer in Explicit Lipid/Water Environment. Biophysj *86*, 705–
632 717.

633 Karplus, M., and Kuriyan, J. (2005). Molecular dynamics and protein function. Proc.
634 Natl. Acad. Sci. U.S.a. *102*, 6679–6685.

635 Kötting, C., and Gerwert, K. (2005). Proteins in Action Monitored by Time-
636 Resolved FTIR Spectroscopy. Chemphyschem *6*, 881–888.

637 Kurauskas, V., Crublet, E., Macek, P., Kerfah, R., Gauto, D.F., Boisbouvier, J., and
638 Schanda, P. (2016). Chemical Communications *52*, 9558–9561.

639 Lakomek, N.-A., Frey, L., Bibow, S., Böckmann, A., Riek, R., and Meier, B.H.
640 (2017). Proton-Detected NMR Spectroscopy of Nanodisc-Embedded Membrane
641 Proteins: MAS Solid-State vs Solution-State Methods. J Phys Chem B *121*, 7671–
642 7680.

643 Lalli, D., Idso, M.N., Andreas, L.B., Hussain, S., Baxter, N., Han, S., Chmelka, B.F.,
644 and Pintacuda, G. (2017). Proton-Based Structural Analysis of a Heptahelical
645 Transmembrane Protein in Lipid Bilayers. J. Am. Chem. Soc. *139*, 13006–13012.

646 Lanyi, J.K. (2004). Bacteriorhodopsin. Annu. Rev. Physiol. *66*, 665–688.

647 Lanyi, J.K., and Schobert, B. (2007). Structural Changes in the L Photointermediate
648 of Bacteriorhodopsin. Journal of Molecular Biology *365*, 1379–1392.

649 Linser, R., Dasari, M., Hiller, M., Higman, V., Fink, U., Lopez del Amo, J.-M.,
650 Markovic, S., Handel, L., Kessler, B., Schmieder, P., et al. (2011). Proton-detected
651 solid-state NMR spectroscopy of fibrillar and membrane proteins. Angew. Chem.
652 Int. Ed. Engl. *50*, 4508–4512.

653 Lórenz-Fonfría, V.A., Saita, M., Lazarova, T., Schlesinger, R., and Heberle, J.
654 (2017). pH-sensitive vibrational probe reveals a cytoplasmic protonated cluster in
655 bacteriorhodopsin. Proc. Natl. Acad. Sci. U.S.A. *114*, E10909–E10918.

656 Luecke, H., Schobert, B., Richter, H.T., Cartailler, J.P., and Lanyi, J.K. (1999).
657 Structure of bacteriorhodopsin at 1.55 A resolution. Journal of Molecular Biology
658 *291*, 899–911.

659 Mak-Jurkauskas, M.L., Bajaj, V.S., Hornstein, M.K., Belenky, M., Griffin, R.G., and
660 Herzfeld, J. (2008). Energy transformations early in the bacteriorhodopsin
661 photocycle revealed by DNP-enhanced solid-state NMR. Proc. Natl. Acad. Sci.
662 U.S.A. *105*, 883–888.

663 Marx, D., Tuckerman, M.E., Hutter, J., and Parrinello, M (1999). The nature of the
664 hydrated excess proton in water. Nature *397*, 601–604.

665 Mogi, T., Stern, L.J., Marti, T., Chao, B.H., and Khorana, H.G. (1988). Aspartic acid
666 substitutions affect proton translocation by bacteriorhodopsin. Proc. Natl. Acad. Sci.
667 U.S.A. *85*, 4148–4152.

668 Nango, E., Royant, A., Kubo, M., Nakane, T., Wickstrand, C., Kimura, T., Tanaka,
669 T., Tono, K., Song, C., Tanaka, R., et al. (2016). A three-dimensional movie of
670 structural changes in bacteriorhodopsin. Science *354*, 1552–1557.

671 Neutze, R., Pebay-Peyroula, E., Edman, K., Royant, A., Navarro, J., and Landau,
672 E.M. (2002). Bacteriorhodopsin: a high-resolution structural view of vectorial proton
673 transport. Biochim. Biophys. Acta *1565*, 144–167.

Ni, Q.Z., Can, T.V., Daviso, E., Belenky, M., Griffin, R.G., and Herzfeld, J. (2018). Primary Transfer Step in the Light-Driven Ion Pump Bacteriorhodopsin: An Irreversible U-Turn Revealed by Dynamic Nuclear Polarization-Enhanced Magic Angle Spinning NMR. J. Am. Chem. Soc. *140*, 4085–4091.

Nieuwkoop, A.J., Franks, W.T., Rehbein, K., Diehl, A., Akbey, Ü., Engelke, F., Emsley, L., Pintacuda, G., and Oschkinat, H. (2015). Sensitivity and resolution of proton detected spectra of a deuterated protein at 40 and 60 kHz magic-angle-spinning. J. Biomol. NMR *61*, 161–171.

Radu, I., Schleeger, M., Bolwien, C., and Heberle, J. (2009). Time-resolved methods in biophysics. 10. Time-resolved FT-IR difference spectroscopy and the application to membrane proteins. Photochem. Photobiol. Sci. *8*, 1517.

Rothschild, K.J., Zagaeski, M., and Cantore, W.A. (1981). Conformational changes of bacteriorhodopsin detected by Fourier transform infrared difference spectroscopy. Biochem. Biophys. Res. Commun. *103*, 483–489.

Schobert, B., Brown, L.S., and Lanyi, J.K. (2003). Crystallographic Structures of the M and N Intermediates of Bacteriorhodopsin: Assembly of a Hydrogen-bonded Chain of Water Molecules Between Asp-96 and the Retinal Schiff Base. Journal of Molecular Biology *330*, 553–570.

Sheves, M., Albeck, A., Friedman, N., and Ottolenghi, M. (1986). Controlling the pKa of the bacteriorhodopsin Schiff base by use of artificial retinal analogues. Proc. Natl. Acad. Sci. U.S.A. *83*, 3262.

Shibata, M., Tanimoto, T., and Kandori, H. (2003). Water Molecules in the Schiff Base Region of Bacteriorhodopsin. J. Am. Chem. Soc. *125*, 13312–13313.

Shim, S., Dasgupta, J., and Mathies, R.A. (2009). Femtosecond Time-Resolved Stimulated Raman Reveals the Birth of Bacteriorhodopsin's J and K Intermediates. J. Am. Chem. Soc. *131*, 7592–7597.

Spassov, V.Z., Luecke, H., Gerwert, K., and Bashford, D. (2001). pKa calculations suggest storage of an excess proton in a hydrogen-bonded water network in bacteriorhodopsin. Journal of Molecular Biology *312*, 203–219.

VandeVondele, J., and Hutter, J. (2007). Gaussian basis sets for accurate calculations on molecular systems in gas and condensed phases. J. Chem. Phys. *127*, 114105.

Vogt, A., Guo, Y., Tsunoda, S.P., Kateriya, S., Elstner, M., and Hegemann, P. (2015). Conversion of a light-drivenproton pump into a light-gatedion channel. Sci Rep 1–13.

Ward, M.E., Shi, L., Lake, E., Krishnamurthy, S., Hutchins, H., Brown, L.S., and Ladizhansky, V. (2011). Proton-Detected Solid-State NMR Reveals Intramembrane Polar Networks in a Seven-Helical Transmembrane Protein Proteorhodopsin. J. Am. Chem. Soc. *133*, 17434–17443.

Weingarth, M., and Baldus, M. (2013). Solid-State NMR-Based Approaches for Supramolecular Structure Elucidation. Acc. Chem. Res. *46*, 2037–2046.

Wickstrand, C., Dods, R., Royant, A., and Neutze, R. (2015). Bacteriorhodopsin: Would the real structural intermediates please stand up? Biochim. Biophys. Acta *1850*, 536–553.

Zheng, L., Fishbein, K.W., Griffin, R.G., and Herzfeld, J. (1993). Two-dimensional solid-state proton NMR and proton exchange. J. Am. Chem. Soc. *115*, 6254–6261.

Zhou, D.H., and Rienstra, C.M. (2008). High-performance solvent suppression for proton detected solid-state NMR. Journal of Magnetic Resonance *192*, 167–172.

Zhou, D.H., Shah, G., Cormos, M., Mullen, C., Sandoz, D., and Rienstra, C.M. (2007). Proton-Detected Solid-State NMR Spectroscopy of Fully Protonated Proteins at 40 kHz Magic-Angle Spinning. J. Am. Chem. Soc. *129*, 11791–11801.

Zhou, D.H., Shea, J.J., Nieuwkoop, A.J., Franks, W.T., Wylie, B.J., Mullen, C., Sandoz, D., and Rienstra, C.M. (2007). Solid-State Protein-Structure Determination with Proton-Detected Triple-Resonance 3D Magic-Angle-Spinning NMR Spectroscopy. Angew. Chem. Int. Ed. *46*, 8380–8383.

4

INSIGHT INTO SMALL MOLECULE BINDING TO THE NEONATAL FC RECEPTOR BY X-RAY CRYSTALLOGRAPHY AND 100 KHZ MAGIC-ANGLE-SPINNING NMR

4.1 Synopsis

As introduced in chapter 1, the different features of protonation dynamics may play a role in protein-protein interactions. The binding of human serum albumin (HSA) and Immunoglobulin G (IgG) to the neonatal Fc receptor (FcRn) is such a case. It has been shown that these interactions are pH-dependent, modulated through protonatable amino acid side chains at the respective binding interfaces. Since FcRn has been validated as a drug target in autoimmune diseases, we intend to develop a small molecule that may be used as an inhibitor of the FcRn–IgG interaction after further chemical optimization.

In a fragment screening approach, we identified a small molecule that binds into an evolutionarily conserved cavity of FcRn. We could solve the crystal structure of the soluble extra-cellular domain of FcRn ($FcRn_{ECD}$) in complex with the compound. However, structural changes in $FcRn_{ECD}$ upon small molecule binding could not be observed in the crystal structures with and without ligand. This might be due to crystal packing hindering conformational changes in remote regions, i.e. the observation of potential allosteric effects may be not possible in this case. To address this, we applied MAS NMR to the soluble protein. The use of NMR at 100 kHz MAS was crucial since $FcRn_{ECD}$ cannot be produced in deuterated form in sufficient amounts, and because of its size of 42 kDa. For these reasons, the acquisition of triple-resonance experiments required for the resonance assignment procedure is not possible with sufficient S/N in solution-state NMR. Interestingly, we could sediment the soluble protein directly into a 0.7 mm MAS rotor by ultracentrifugation, making proton-detected MAS NMR at 100 kHz on the fully protonated protein possible. This allowed us to establish resonance assignments based on (H)NH, (H)CANH, (H)CA(CO)NH and (H)CBCANH spectra. Using (H)CANH spectra recorded with and without ligand, we could detect chemical shift perturbations (CSPs). These were found to be in the small molecule binding pocket and the HSA binding site (and in other remote regions) of $FcRn_{ECD}$, indicating allosteric effects. Unfortunately, we could not observe CSPs in the IgG binding site which would highlight the potential of allosteric modulation of the FcRn–IgG interaction. This suggests the need of an optimized ligand to induce larger structural changes upon binding of the compound.

With the developed small molecule, the FcRn–IgG protein-protein interaction based on changes in protonation states could not be perturbed. Still, the current chapter contributes methodologically to future protonation dynamics studies by applying 100 kHz MAS NMR to soluble proteins upon sedimentation using ultracentrifugation.

4.2 Personal contribution

In this study, I prepared $FcRn_{ECD}$ samples with and without UCB-FcRn-303 for NMR experiments, recorded MAS NMR spectra, analyzed data and was involved in writing the manuscript. $FcRn_{ECD}$ was expressed and purified by James White and Robert Griffin.

Alex Macpherson, Nicolas Basse and Alastair Lawson designed the study; Daniel Stöppler, Alex Macpherson, Susanne Smith-Penzel, Fabien Lecomte, Hervé Deboves, Richard D. Taylor, Tim Norman, John Porter, Lorna C. Waters, Marta Westwood, Ben Cossins, Katherine Cain, James White, Robert Griffin, Christine Prosser, Sebastian Kelm, Amy H. Sullivan and David Fox III performed research; Daniel Stöppler, Alex Macpherson, Susanne Smith-Penzel, Nicolas Basse, Fabien Lecomte, Hervé Deboves, Richard D. Taylor, Tim Norman, John Porter, Lorna C. Waters, Marta Westwood, Ben Cossins, Katharine Cain, James White, Robert Griffin, Christine Prosser, Sebastian Kelm, Amy H. Sullivan, David Fox III, Mark D. Carr, Alistair Henry, Richard Taylor, Beat H. Meier, Hartmut Oschkinat, and Alastair Lawson analyzed data; Daniel Stöppler and Alex Macpherson wrote the paper with contributions from David Fox III and Hartmut Oschkinat.

4.3 Original Publication

Daniel Stöppler,[#] Alex Macpherson,[#] Susanne Smith-Penzel, Nicolas Basse, Fabien Lecomte, Hervé Deboves, Richard D. Taylor, Tim Norman, John Porter, Lorna C. Waters, Marta Westwood, Ben Cossins, Katharine Cain, James White, Robert Griffin, Christine Prosser, Sebastian Kelm, Amy H. Sullivan, David Fox III, Mark D. Carr, Alistair Henry, Richard Taylor, Beat H. Meier, Hartmut Oschkinat, and Alastair Lawson:

'Insight into Small Molecule Binding to the Neonatal Fc Receptor by X-ray Crystallography and 100 kHz Magic-Angle-Spinning NMR', *PLOS Biology*, 2018, (16):5, e2006192

[#] ***Equal contribution***

The article and all additional supplementary files are available at https://doi.org/10.1371/journal.pbio.2006192

PLOS BIOLOGY

METHODS AND RESOURCES

Insight into small molecule binding to the neonatal Fc receptor by X-ray crystallography and 100 kHz magic-angle-spinning NMR

Daniel Stöppler[1‡], Alex Macpherson[2‡], Susanne Smith-Penzel[3], Nicolas Basse[4], Fabien Lecomte[2], Hervé Deboves[5], Richard D. Taylor[2], Tim Norman[2], John Porter[6], Lorna C. Waters[7], Marta Westwood[2], Ben Cossins[2], Katharine Cain[8], James White[2], Robert Griffin[2], Christine Prosser[2], Sebastian Kelm[2], Amy H. Sullivan[9], David Fox, III[9], Mark D. Carr[7], Alistair Henry[2], Richard Taylor[2], Beat H. Meier[3], Hartmut Oschkinat[1]*, Alastair D. Lawson[2]*

1 Leibniz-Forschungsinstitut für Molekulare Pharmakologie, Berlin, Germany, **2** UCB Celltech, Slough, United Kingdom, **3** Laboratory of Physical Chemistry, ETH Zürich, Zürich, Switzerland, **4** Sanofi, Strasbourg, France, **5** Evotec, Milton, United Kingdom, **6** Midatech Pharma Plc, Milton, United Kingdom, **7** Leicester Institute of Structural and Chemical Biology, University of Leicester, Leicester, United Kingdom, **8** Vertex, Milton, United Kingdom, **9** Beryllium Discovery, Bedford, Massachusetts, United States of America

‡ These authors share first authorship on this work.
* oschkinat@fmp-berlin.de (HO); alastair.lawson@ucb.com (ADL)

Citation: Stöppler D, Macpherson A, Smith-Penzel S, Basse N, Lecomte F, Deboves H, et al. (2018) Insight into small molecule binding to the neonatal Fc receptor by X-ray crystallography and 100 kHz magic-angle-spinning NMR. PLoS Biol 16(5): e2006192. https://doi.org/10.1371/journal.pbio.2006192

Academic Editor: Ann Stock, UMDNJ/Robert Wood Johnson Medical School, United States of America

Received: February 6, 2018

Accepted: May 2, 2018

Published: May 21, 2018

Data Availability Statement: The crystallographic data are available from the Protein Data Bank (www.rcsb.org, accession numbers 6C97, 6C98, and 6C99) and the chemical-shift data from the Biological Magnetic Resonance Data Bank (www.bmrb.wisc.edu, accession number 27437). All other relevant data are within the paper and its Supporting information files.

Abstract

Aiming at the design of an allosteric modulator of the neonatal Fc receptor (FcRn)–Immunoglobulin G (IgG) interaction, we developed a new methodology including NMR fragment screening, X-ray crystallography, and magic-angle-spinning (MAS) NMR at 100 kHz after sedimentation, exploiting very fast spinning of the nondeuterated soluble 42 kDa receptor construct to obtain resolved proton-detected 2D and 3D NMR spectra. FcRn plays a crucial role in regulation of IgG and serum albumin catabolism. It is a clinically validated drug target for the treatment of autoimmune diseases caused by pathogenic antibodies via the inhibition of its interaction with IgG. We herein present the discovery of a small molecule that binds into a conserved cavity of the heterodimeric, extracellular domain composed of an α-chain and β2-microglobulin (β2m) ($FcRn_{ECD}$, 373 residues). X-ray crystallography was used alongside NMR at 100 kHz MAS with sedimented soluble protein to explore possibilities for refining the compound as an allosteric modulator. Proton-detected MAS NMR experiments on fully protonated [^{13}C,^{15}N]-labeled $FcRn_{ECD}$ yielded ligand-induced chemical-shift perturbations (CSPs) for residues in the binding pocket and allosteric changes close to the interface of the two receptor heterodimers present in the asymmetric unit as well as potentially in the albumin interaction site. X-ray structures with and without ligand suggest the need for an optimized ligand to displace the α-chain with respect to β2m, both of which participate in the $FcRn_{ECD}$–IgG interaction site. Our investigation establishes a method to characterize structurally small molecule binding to nondeuterated large proteins by NMR, even in their glycosylated form, which may prove highly valuable for structure-based drug discovery campaigns.

Funding: Deutsche Forschungsgemeinschaft (grant number SFB 1078 B1). The funder had no role in study design, data collection and analysis, decision to publish, or preparation of the manuscript. iNEXT (grant number WP1). The funder had no role in study design, data collection and analysis, decision to publish, or preparation of the manuscript. Swiss National Science Foundation (grant number 200020_159707 and 200020_146757). The funder had no role in study design, data collection and analysis, decision to publish, or preparation of the manuscript. European Research Council (grant number 741863, FASTER). The funder had no role in study design, data collection and analysis, decision to publish, or preparation of the manuscript.

Competing interests: I have read the journal's policy and the authors of this manuscript have the following competing interests. Alex Macpherson, Fabien Lecomte, Richard D. Taylor, Tim Norman, Marta Westwood, Ben Cossins, James White, Robert Griffin, Christine Prosser, Sebastian Kelm, Alistair Henry, Richard Taylor, and Alastair D. Lawson are all current or former employees and/or shareholders in UCB Pharma. Nicolas Basse is an employee and/or shareholder in Sanofi. Hervé Deboves is an employee and/or shareholder in Evotec. John Porter is an employee and/or shareholder in Midatech Pharma. Katharine Cain is an employee and/or shareholder in Vertex. Amy H. Sullivan and David Fox III are/were employees and/or shareholders in Beryllium Discovery. This work was funded by UCB Pharma.

Abbreviations: β2m, β2-microglobulin; APS, Advanced Photon Source; AUC, analytical ultracentrifugation; BMRB, Biological Magnetic Resonance Data Bank; CD8, cluster of differentiation 8; CLS, Canadian Light Source; COOT, Crystallographic Object-Oriented Toolkit; CP, Cross Polarization; CSP, chemical-shift perturbation; ECD, extracellular domain; FcRn, neonatal Fc receptor; $FcRn_{ECD}$, extracellular domain of the neonatal Fc receptor; HSA, Human Serum Albumin; IgG, Immunoglobulin G; MAS, magic-angle-spinning; MHC1, class I major histocompatibility complex; ORF, Open Reading Frame; PDB, Protein Data Bank; r.m.s.d., root mean square deviation; SPR, Surface Plasmon Resonance; TCR, T cell receptor; TIPS, titerless infected-cells preservation and scale-up.

Author summary

In drug design, a detailed characterization of structural changes induced by drug binding is useful for further optimizing lead compounds. In many cases, structural alterations are distant from the compound binding site, potentially acting through allosteric effects. These allosteric effects are often difficult to observe by static methods, i.e., X-ray crystallography, but can be monitored by NMR spectroscopy. The latter method, however, has size-limitations when investigating the protein backbone structure in solution-state. To overcome this, we present an innovative approach employing ultrafast magic-angle-spinning (MAS) NMR on the extracellular domain of the neonatal Fc receptor ($FcRn_{ECD}$). This is a validated drug target in autoimmune diseases, and we aim to identify and characterize novel compounds to serve as starting points to develop allosteric inhibitors of this receptor. After sedimentation, we could record well-resolved proton-detected MAS NMR spectra of the fully protonated [^{13}C,^{15}N]-labeled protein, enabling the observation of structural changes. In combination with computational methods, X-ray crystallography, and other biophysical tools, we present new compounds that may be used as allosteric modulators of FcRn after further optimization. The introduced MAS NMR approach can be applied to a large variety of proteins to support structure-based drug design, facilitating the detection of allosteric effects.

Introduction

In order to discover new chemical drugs, fragment screening followed by structure-based design is an efficient way to sample chemical space and find hits for challenging target classes such as protein-protein interactions [1–3]. In addition to discovering orthosteric ligands, fragment screening has the potential to locate secondary binding sites on a protein that may be exploited for allosteric regulation [4]. In the development process, a methodology that includes detection of allosteric effects is highly welcome. Magic-angle-spinning (MAS) NMR has the potential to contribute via the detection of long-range chemical-shift changes when the investigated protein is too large for solution-state NMR and can even not be deuterated. It is applied here to a soluble 42 kDa construct of the neonatal Fc receptor (FcRn) within a search for allosteric regulators, employing very fast MAS (100 kHz).

FcRn facilitates new-born humoral immunity by regulating Immunoglobulin (IgG) transport across the epithelium [5]. In addition, it has been shown to bind to IgG and Human Serum Albumin (HSA) at nonoverlapping sites in a pH-dependent manner (Fig 1) [6,7]. This allows maintenance of IgG and HSA homeostasis, accounting for the long serum half-life of both proteins [8–11]. At low pH, the interaction of FcRn with IgG occurs through protonation of ionizable residues, located at the CH2–CH3 hinge of the IgG Fc, which produces transient, intermolecular salt bridges with negatively charged residues on FcRn [12]. The interaction of FcRn with IgG and HSA occurs in acidified early endosomes, diverting the proteins from catabolism and carrying them back to the neutral pH environment of the extracellular compartment. At near-neutral pH, the affinity of the interaction decreases, and the complex dissociates [10,13].

Existing as a heterodimer composed of β2-microglobulin (β2m) and a membrane-anchored α-chain (Fig 1), FcRn is homologous to the class I major histocompatibility complex (MHC1) [14]. MHC1 presents antigenic peptide fragments to the T cell receptor (TCR) in complex with cluster of differentiation 8 (CD8) [14]. In contrast, FcRn is not involved in endogenous peptide presentation to the TCR; its peptide-binding groove is closed and nonfunctional [14].

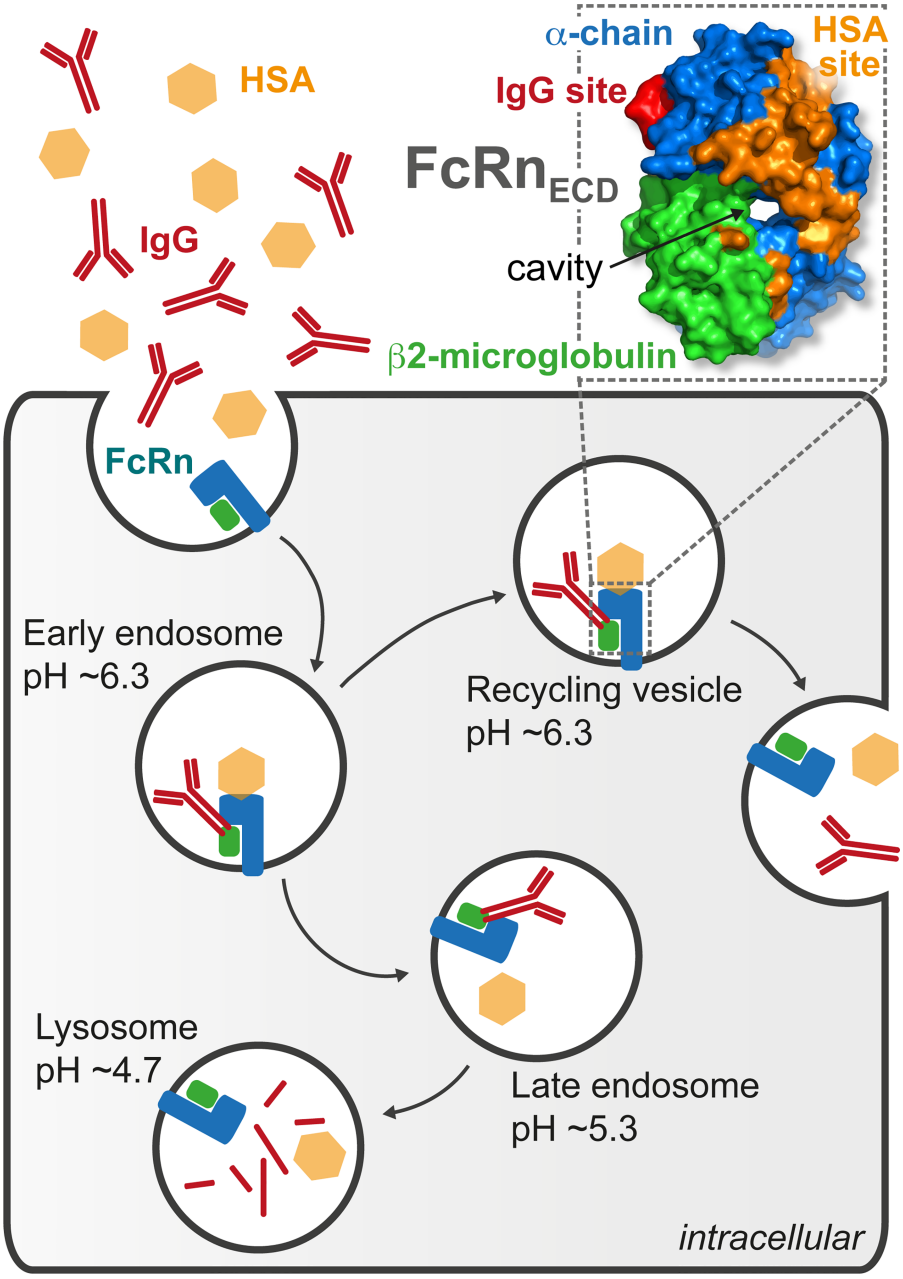

Fig 1. FcRn allows maintenance of protein homeostasis. The soluble extracellular domain of neonatal Fc receptor (FcRn$_{ECD}$, PDB code 1EXU) is a heterodimer composed of β2m (green) and α-chain (blue) with a cavity at the interface between the two proteins. FcRn is involved in the regulation of HSA (orange) and IgG (red) levels. The binding of both HSA and IgG to FcRn is pH dependent, which provides a mechanism for protein homeostasis through endosomal trafficking. β2m, β2-microglobulin; FcRn, neonatal Fc receptor; FcRn$_{ECD}$, extracellular domain of the neonatal Fc receptor; HSA, Human Serum Albumin; IgG, Immunoglobulin G; PDB, Protein Data Bank.

https://doi.org/10.1371/journal.pbio.2006192.g001

The effect of FcRn loss has been studied using β2m-deficient mice, which develop normally but are defective in T cell–mediated cytotoxicity [15]. Deletion of β2m precluded FcRn expression, resulting in a reduction in IgG half-life [16–18]. Additionally, random mutation of residues proximal to the IgG–FcRn binding site allowed selection of Fc variants with increased

affinity for FcRn at pH 6. These Fc constructs maintained pH-dependent binding and showed an extended half-life relative to wild-type IgG [19].

FcRn has been proposed as a drug target in the treatment of autoimmune diseases, in which pathogenic autoantibodies are detrimental to health [20]. Examples of such diseases include, but are not restricted to, myasthenia gravis, Guillain–Barré syndrome, and dermatomyositis [21–24]. Antibodies produced against the FcRn heavy chain ameliorated myasthenia gravis symptoms in rats, and it has been shown that mice without FcRn are resistant to autoimmune disease [25–27]. The current treatment for these conditions is intravenous application of immunoglobulin, which increases the turnover of pathogenic IgG by saturating FcRn [26]. Recently, rozanolixizumab, an antihuman FcRn monoclonal antibody, reduced the serum IgG concentration in a randomized phase 1 study, providing clinical evidence for the potential of an anti-FcRn therapeutic [28].

A chemical inhibitor to control FcRn trafficking is therapeutically desirable for potential treatment of autoimmune disorders. Orthosteric peptide inhibitors with in vivo efficacy have previously been reported [29–33]. Additionally, structure–activity relationships of small molecule antagonists using ELISA assays have also been described [34]. However, to date, no allosteric modulators of FcRn–IgG or FcRn–HSA interactions have been reported. Should such molecules be found, they could be used therapeutically or as tools in biomedical investigations.

In this study, we present the discovery of a compound that binds to the soluble extracellular domain of FcRn, abbreviated here as $FcRn_{ECD}$. In the initial screening process, complementary in silico methods were used to predict binding sites on the basis of charge and topography or sequence conservation, alone and in combination [35–37]. The interaction of the ligand with $FcRn_{ECD}$ is investigated by a combination of X-ray crystallography and proton-detected, ultrafast MAS NMR, revealing its localization in an evolutionarily conserved binding pocket. At high MAS frequencies of 100 kHz, we could acquire well-resolved proton-detected NMR spectra on sedimented, fully protonated $FcRn_{ECD}$, allowing de-novo chemical-shift assignments of residues in the binding pocket and in β2m through establishing sequential connections. MAS NMR pinpoints chemical-shift changes upon ligand binding close to the binding site and in regions distant to it. In this context, MAS NMR helps to exclude the influence of crystal packing effects by making use of protein solutions. Both crystal structures with and without ligand were available, but structural changes were not obvious when using global fitting procedures, with the molecules possibly "locked" into a conformation by crystal contacts. To identify sections of the structure not affected by ligand binding for a fit that is also sensitive to small allosteric effects, residues that did not show chemical-shift changes were used to produce "chemical-shift–informed" overlays of $FcRn_{ECD}$ X-ray structures with and without ligand. Our findings suggest that therapeutic intervention in autoimmune diseases may be achieved through allosteric small molecules that bind to $FcRn_{ECD}$. In addition, such compounds could potentially be used as chemical probes to study FcRn trafficking. The presented approach highlights further the use of MAS NMR for detecting structural changes in nondeuterated proteins expressed in mammalian cells upon ligand binding.

Results and discussion

X-ray crystallography of $FcRn_{ECD}$ and ligandability assessments

Small molecule binding sites on proteins can be identified based on surface shape, charge, and functionality. We used SiteMap software to identify binding sites on the $FcRn_{ECD}$ [35]. To obtain structural data for our analysis, diffraction data for $FcRn_{ECD}$ crystals, at pH 3 and pH 8.5, were collected at cryogenic temperatures and structures solved to 2.0 Å and 2.45 Å, respectively, by molecular replacement. Two copies of $FcRn_{ECD}$ were found in the asymmetric unit.

In addition to the structures at acidic and basic pH, a pH 7.2 structure was generated using molecular dynamics simulation (S1 Fig and S1 Text).

The SiteMap software detected a number of regions with a druggability score >1.0, a nominal quantifier indicating that nM binding might be achieved with a conventional small molecule of <500 Da molecular weight. In particular, SiteMap identified a ligandable site at the interface between the α-chain and β2m (S1 Fig and S1 Text). The respective boundaries were predicted to vary with pH, with the area described as either one large or three distinct cavities.

No regions near the IgG binding site were found by SiteMap. Based on our analysis, should an orthosteric pocket for an IgG blocking small molecule exist, it is likely to be transient in nature and not stabilized in the crystal lattice.

Evolutionary conservation of $FcRn_{ECD}$

On the premise that evolutionarily conserved cavities may have an associated function, we evaluated such conservation of the cavities found by SiteMap (S2 Fig). We identified ortholog sequences using OrthoDB and performed sequence alignments using Clustal Omega [38,39]. A homology model was then created for each sequence using MEDELLER that enabled us to visualize mutations according to the evolutionary conservation in PyMOL [40,41].

Our sequence analysis broadly supports the notion that regions of the protein important for structural integrity or function are conserved, in particular the interface between the α-chain and β2m. It contains key contacts, such as those between $D53_{\beta 2m}$, $Q34_{\alpha\text{-chain}}$, and $S37_{\alpha\text{-chain}}$, and conservation of these contacts preserves the structural integrity of the noncovalently linked heterodimer.

Additionally, motifs within the HSA binding site were also conserved. One of them has previously been identified as being critical for albumin binding and was the site of a protein contact in our pH 3 and pH 8.5 crystal structures, between the two copies of $FcRn_{ECD}$ in the asymmetric unit [8]. We were initially surprised to see the IgG binding site is poorly conserved with the exception of key residues, such as $D130_{\alpha\text{-chain}}$. This may be attributed to the heterogeneity in Fc moieties between mammalian orthologues, which presumably reduces species' cross-reactivity. Of the regions identified by SiteMap, the central cavity was highly conserved, potentially due to the proximity to the dimer interface.

Fragment screening to identify small molecules

Our in silico analysis suggests the presence of an evolutionarily conserved binding site at the interface between the α-chain and β2m. To find ligands for this cavity and, potentially, other sites, a solution-state NMR fragment screen was performed. For this purpose, we used an in-house library of approximately 1,100 molecules containing fluorine atoms to enable ligand interrogation by ^{19}F Carr-Purcell-Meiboom-Gill NMR [42,43]. This screen detected 143 potential binders. In order to select compounds for crystallographic studies, active molecules were further tested in Saturated Transfer Difference NMR experiments and by Surface Plasmon Resonance (SPR), yielding an estimated K_D of 80 μM for the highest affinity fragment, the racemate UCB-FcRn-84 (S3 Fig and S1 Data) [44,45]. Chiral separation showed preferential binding of the R enantiomer. Competition of UCB-FcRn-84 with IgG was tested in a $FcRn_{ECD}$–IgG FRET assay; however, no measurable inhibition was observed.

Crystallographic studies of ligand-bound $FcRn_{ECD}$

Confirmed hits from the fragment-screen were soaked into $FcRn_{ECD}$ crystals that had been grown under acidic conditions. Based on the derived crystal structures, we aimed to further improve both affinity and solubility of the ligand.

UCB-FcRn-84 was found in the conserved cavity at the interface of β2m and the α-chain (S4 Fig and S2 Text), as predicted by SiteMap. Key properties of binding interactions include burial of the 3-fluorophenyl group in a hydrophobic cavity composed of $Y26_{\beta 2m}$, $S52_{\beta 2m}$, $Y63_{\beta 2m}$, $L65_{\beta 2m}$, $W29_{\alpha\text{-chain}}$ and $P228_{\alpha\text{-chain}}$. The most visually striking feature of the binding pocket is a tunnel-like cavity that extends through the middle of the protein (S5 Fig and S2 Text). The bicyclic ring of UCB-FcRn-84 occupies this cavity, being involved in one direct and one water-mediated hydrogen bond to the main-chain of $Q34_{\alpha\text{-chain}}$.

As the fragment was centrally located in this region, it afforded us a tractable chemical platform to explore the binding site further (S4 Fig and S2 Text). We attempted to improve the affinity of UCB-FcRn-84 by better occupying space around the 3-fluorophenyl group, which was nested in a well-defined hydrophobic pocket. Notably, we identified a small area available for growth adjacent to the unsubstituted meta position of the 3-fluorophenyl group. After scanning a range of disubstituted phenyl derivatives, we identified 3,5 difluorophenyl as the best option, yielding a ligand with 2.4 μM affinity for the racemate. Moreover, adding a 3-pyridile group in position 5 led to an equipotent compound (UCB-FcRn-303) but with improved solubility (S5 and S6 Figs, S1 Data and S2 Text).

The crystal structure of UCB-FcRn-303 bound to $FcRn_{ECD}$ displays the R enantiomer (Fig 2 and S5 Fig). The binding mode is consistent with the position observed for UCB-FcRn-84 (Fig 2A and 2B, S4 and S5 Figs). The di-substituted phenyl ring better fills the hydrophobic pocket in the α-chain/β2m interface, while hydrogen bond interactions are maintained with the α-chain and the local water network.

In biochemical experiments molecules from our series did not inhibit IgG binding when tested in a $FcRn_{ECD}$–IgG FRET competition assay. This was consistent with our crystallographic studies which showed no discernible change in the IgG binding site, although accurate interpretation of small changes may be hampered by crystal contacts. The $FcRn_{ECD}$ crystallized with two copies of the heterodimer present in the asymmetric unit, packing in an anti-parallel fashion (Fig 2A). Overlay of the IgG heavy chain–$FcRn_{ECD}$ complex (Protein Data Bank [PDB] code 1FRT) with the ligand-free crystal structure shows significant overlap between CH2 and CH3 domains of IgG and symmetry related copies of $FcRn_{ECD}$ (S7 Fig) [46].

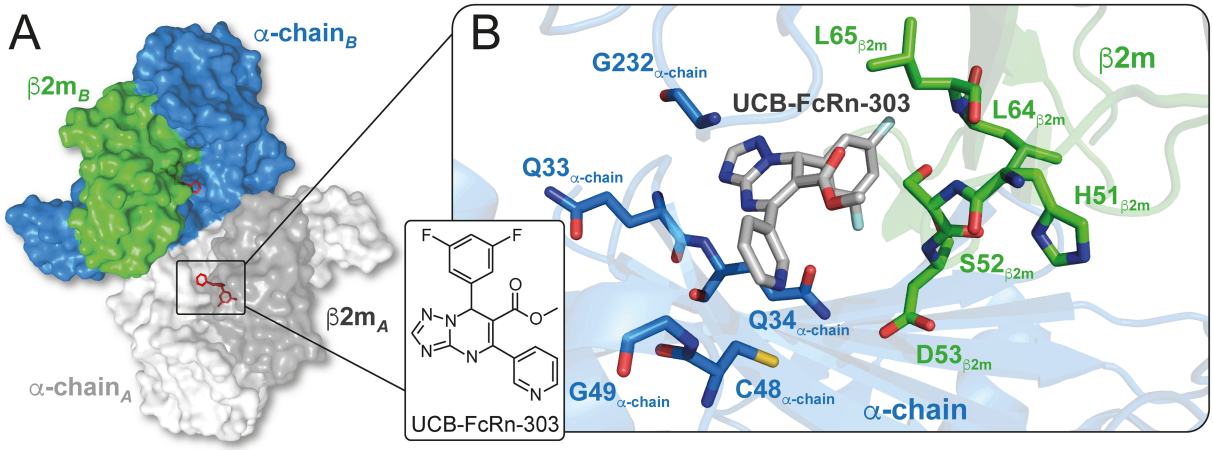

Fig 2. Crystal structure of the compound UCB-FcRn-303 (R enantiomer) bound to $FcRn_{ECD}$. (A) The protein crystallized as a dimer composed of two β2m (dark grey and green) and two α-chain (light grey and blue) molecules. **(B)** At the interface of β2m and the α-chain, UCB-FcRn-303 (grey) occupies a binding pocket with Glycine, Cysteine, hydrophobic (Leucine), charged (Histidine, Aspartate), and polar uncharged (Serine, Glutamine) residues. β2m, β2-microglobulin; FcRn, neonatal Fc receptor; $FcRn_{ECD}$, extracellular domain of the neonatal Fc receptor.

https://doi.org/10.1371/journal.pbio.2006192.g002

In order to determine whether the ligand might induce small conformational and/or dynamic changes in regions beyond the direct binding site, we have used orthogonal solution-based techniques, which will avoid conformational restrictions imposed by crystal packing.

Sedimented, fully protonated $FcRn_{ECD}$ yielded well resolved proton-detected MAS NMR spectra

Until recently, solution-state and proton-detected MAS NMR typically required deuteration of proteins in the size-range of the 42 kDa $FcRn_{ECD}$, as the signal-to-noise ratios obtained in triple-resonance experiments involving $^{13}C\beta$ and $^{13}C\alpha$ chemical-shifts critically depend on the T_2 of ^{13}C coherences [47,48]. Since we were unable to produce deuterated $FcRn_{ECD}$ in sufficient amounts it was not possible to acquire 3D solution-state NMR spectra that would allow sequential assignments. The spectral quality of a 2D ^{15}N-^{1}H correlation spectrum recorded in solution, however, is remarkably high (S8 Fig) [49]. It indicates that $FcRn_{ECD}$ most likely does not form a stable dimer of heterodimers in solution at the applied concentrations, which agrees with biochemical data and earlier studies [50]. At least 227 of the expected 349 backbone amide signals could be observed, with the remainder of the signals most probably obscured by overlap.

To circumvent these experimental limitations, we applied MAS NMR. Progress in recent years, in particular ever faster sample spinning, enables the acquisition of proton-detected MAS NMR spectra on fully protonated samples which increases sensitivity and facilitates resonance assignments through triple-resonance experiments [51–54]. At the highest MAS frequency routinely available (110 kHz), well resolved proton spectra have been reported for fully protonated microcrystalline and membrane proteins, sedimented assemblies and fibrillar proteins [55–57].

In the present case, we have investigated soluble $FcRn_{ECD}$ by MAS NMR experiments via sedimentation. For this purpose, the availability of dedicated filling tools is a prerequisite [58,59]. With the help of such appliances, we sedimented the 42 kDa soluble, fully protonated [^{13}C,^{15}N]-labeled $FcRn_{ECD}$ by ultracentrifugation directly into a 0.7 mm MAS rotor (Fig 3A).

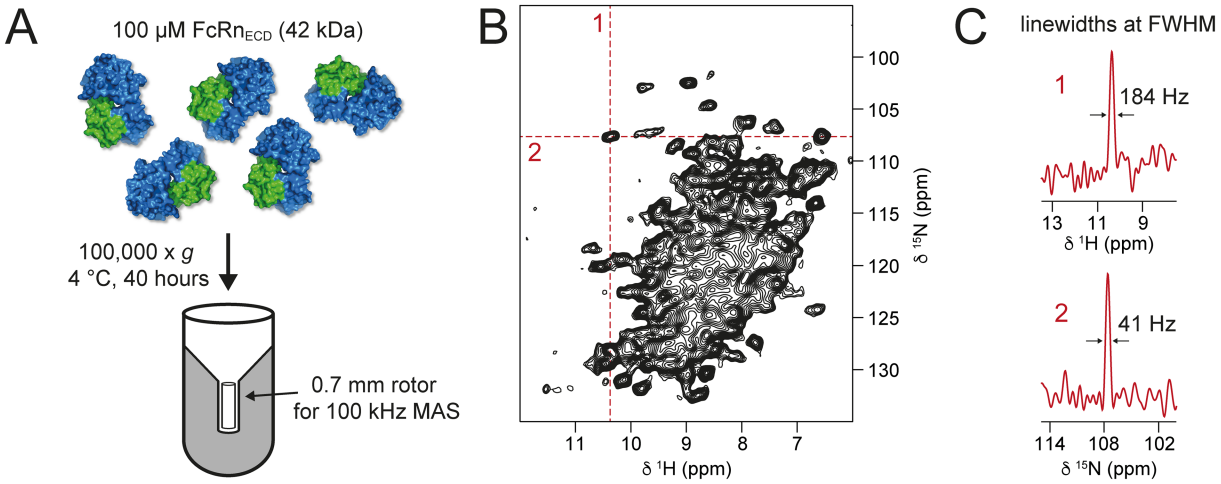

Fig 3. Proton-detected MAS NMR on fully protonated $FcRn_{ECD}$. (A) The soluble $FcRn_{ECD}$ (42 kDa) was sedimented by ultracentrifugation at 100,000 x *g* directly into a 0.7 mm MAS NMR rotor using a home-made filling tool. **(B)** 2D ^{15}N-^{1}H correlation spectrum recorded at 100 kHz MAS of fully protonated [^{13}C,^{15}N]-labeled $FcRn_{ECD}$. **(C)** Typical linewidths of ^{1}H (1) and ^{15}N (2) at full-width-half-maximum (FWHM) of a selected cross peak from the ^{15}N-^{1}H spectrum. β2m, β2-microglobulin; FcRn, neonatal Fc receptor; $FcRn_{ECD}$, extracellular domain of the neonatal Fc receptor.

https://doi.org/10.1371/journal.pbio.2006192.g003

The 2D ^{15}N-^{1}H correlation spectrum measured at 100 kHz MAS is shown in Fig 3B. The observed linewidths demonstrate a remarkable spectral quality by MAS NMR standards (Fig 3C). Recorded at a magnetic field of about 20 T, the ^{1}H and ^{15}N linewidths of a selected typical cross peak are 184 Hz and 41 Hz, respectively. The amide ^{1}H linewidth of $FcRn_{ECD}$ is still higher than is observed in the model protein GB1, by a factor of approximately 1.8, but similar to the precipitated viral capsid coat protein AP205 [60]. The spectrum displays a large number of unresolved signals and a considerable fraction of signals that are well dispersed, both of which may be assigned on the basis of suitable triple-resonance spectra.

In order to monitor the folding state of $FcRn_{ECD}$ in the sedimented sample, we compared the MAS ^{15}N-^{1}H spectrum to the ^{15}N-^{1}H correlation recorded in solution (S8 Fig and S3 Text). The agreement of the spectra indicates that the structure of $FcRn_{ECD}$ in solution is very similar to the one in the sedimented sample. $FcRn_{ECD}$ did not form the stable dimers of heterodimers in solution as had been observed in the crystal structure. Analytical ultracentrifugation, however, reveals a concentration-dependent protomer–diprotomer equilibrium of the $FcRn_{ECD}$ heterodimer in solution, with a very low populated diprotomer fraction (S9 Fig and S4 Text). It is possible that this equilibrium is changed in the sedimentation process which may explain small chemical-shift differences. However, due to the signal overlap in the ^{15}N-^{1}H MAS NMR spectrum, a more detailed chemical-shift comparison is not possible.

Resonance assignments in proton-detected MAS NMR spectra of $FcRn_{ECD}$

To allow interpretation of chemical-shift perturbations (CSPs) upon binding of UCB-FcRn-303 to $FcRn_{ECD}$, resonance assignments are critical. The high MAS frequencies now available facilitate an assignment procedure based on triple-resonance MAS NMR experiments as in solution-state NMR. These include (H)CANH, (H)CBCANH, (H)CA(CO)NH, and (H)CBCA(CO)NH spectra, yielding assignments of ^{15}N, ^{1}H^{N}, ^{13}Cα0, and ^{13}Cβ chemical-shifts [61,62]. If it is not possible to obtain a (H)CBCA(CO)NH spectrum with sufficient signal-to-noise due to too short ^{13}Cα and ^{13}CO relaxation times, the first two experiments allow for identification of amino acids that, in a following step, can be sequentially connected according to the protein sequence by using a (H)CA(CO)NH spectrum. In this study, such spectra were acquired on the fully protonated [^{13}C,^{15}N]-labeled $FcRn_{ECD}$ enabling assignments of 25 α-chain residues close to the binding pocket and of 73% of all β2m residues.

To ease the assignment of β2m resonances, we made use of data in Beerbaum and colleagues, in which [^{2}H,^{13}C,^{15}N]-labeled β2m was investigated in complex with unlabeled MHC1 [63]. However, the final assignments were achieved by establishing sequential connections along the protein backbone, as shown for the sequence from $K41_{\beta 2m}$ to $R45_{\beta 2m}$ (Fig 4). All chemical-shift assignments are listed in S1 Table and S2 Data and are deposited in the Biological Magnetic Resonance Data Bank (BMRB) (accession number 27437). In total, signals of 98 residues were assigned this way (S1 Table, S2 Data, and S5 Text). The more sensitive (H)CANH spectrum contained 84 additional resolved cross peaks that could not be assigned further due to overlap or lacking correlations in the less sensitive (H)CA(CO)NH and (H)CBCANH spectra.

Interestingly, a large number of the measured ^{13}Cα, ^{13}Cβ, ^{15}N, and ^{1}H chemical-shifts of β2m in the $FcRn_{ECD}$ heterodimer match the observed solution-state NMR resonances for deuterated β2m in MHC1 complexes of the previous study (S1 Table and S5 Text) [63]. Differences in chemical-shifts can be explained by ^{1}H/^{2}H isotope effects, the limited number of amino acid substitutions in MHC1, potential dimers of $FcRn_{ECD}$ heterodimers in the sedimented sample, and differences in buffer and temperature [64]. The similarity of the chemical-shifts supports the notion that β2m adopts its globular fold in the sedimented sample of

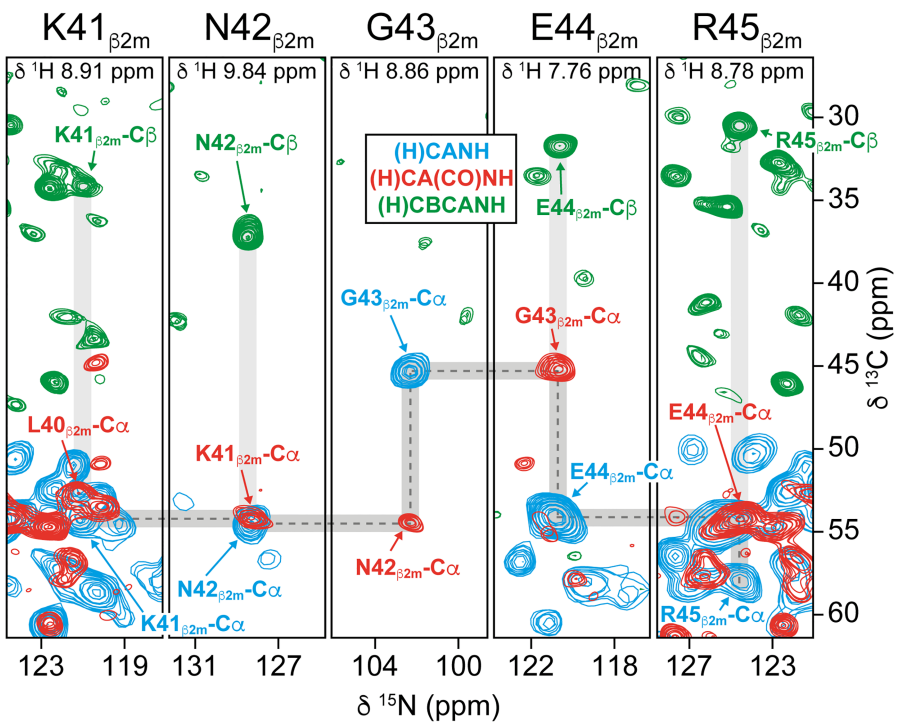

Fig 4. Triple-resonance MAS NMR spectra enable assignments of chemical-shifts. Sequential resonance assignments using the experiments (H)CANH (blue), (H)CA(CO)NH (red), and (H)CBCANH (green) recorded on fully protonated [^{13}C,^{15}N]-labeled FcRn$_{ECD}$ at 100 kHz MAS. As an example, the sequential connections from K41$_{β2m}$ to R45$_{β2m}$ in β2m are indicated by dashed lines. All assigned chemical-shifts can be found in S1 Table, S2 Data, and in the BMRB (accession number 27437). β2m, β2-microglobulin; BMRB, Biological Magnetic Resonance Data Bank; FcRn$_{ECD}$, extracellular domain of the neonatal Fc receptor; MAS, magic-angle-spinning.

https://doi.org/10.1371/journal.pbio.2006192.g004

FcRn$_{ECD}$. Based on these findings and on the similarity between the solution-state ^{15}N-^{1}H and MAS ^{15}N-^{1}H spectra, we assume the overall FcRn$_{ECD}$ structure to be highly similar in solution and in sedimented samples (S8 Fig, S3 Text, S1 Table and S5 Text).

In summary, (H)CANH, (H)CA(CO)NH, and (H)CBCANH spectra represent an acceptable basis for obtaining backbone resonance assignments and allowed us to exploit CSPs as monitors for structural alterations in FcRn$_{ECD}$ upon UCB-FcRn-303 binding.

Structural changes in FcRn$_{ECD}$ upon binding of UCB-FcRn-303

CSPs (Δδ) are probes for both direct effects of ligand binding and concomitant long-range structural changes in receptor proteins that may hint at allosteric effects. Since differences between X-ray structures with and without ligand may be masked by crystal contacts, we analyzed this possibility by comparing 3D (H)CANH spectra recorded on samples of FcRn$_{ECD}$ with and without UCB-FcRn-303 (Fig 5A and 5B). The introduction of a third dimension compared to a 2D ^{15}N-^{1}H correlation leads to better spectral resolution. The observed minimal chemical-shift differences are displayed in Fig 5A. Overall, many of the assigned signals show very similar chemical-shifts in both spectra ($\Delta\delta < 0.02$ ppm, white in Fig 5C and 5D), whereas signals that shift significantly (0.02 ppm $< \Delta\delta <$ 0.03 ppm, cyan; 0.03 ppm $< \Delta\delta <$ 0.04 ppm, marine; 0.04 ppm $< \Delta\delta$, dark blue in Fig 5C and 5D) appear well clustered, suggesting a conformational/dynamic change extending from the ligand binding site. In the following discussions, we consider all residues with $\Delta\delta < 0.02$ ppm as not perturbed. Selected cross peaks of

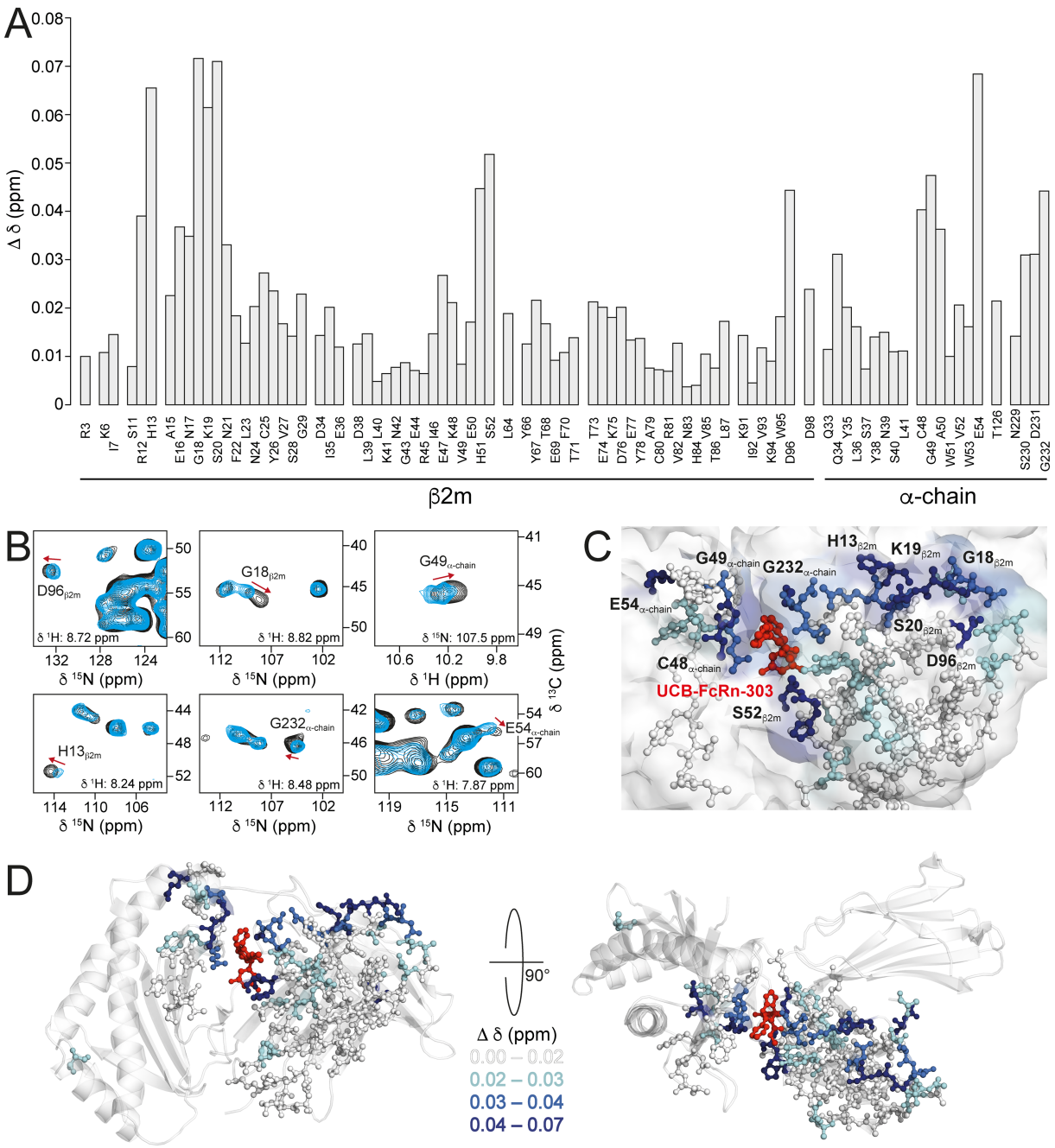

Fig 5. CSPs (Δδ) indicate structural changes in $FcRn_{ECD}$ upon ligand binding. **(A)** CSPs of all assigned amino acids in $FcRn_{ECD}$ upon binding to UCB-FcRn-303, calculated with $\Delta\delta = MIN\{SQRT[(\Delta\delta(^{1}H))^2 + (\Delta\delta(^{13}C)/10)^2 + (\Delta\delta(^{15}N)/5)^2]\}$ (standard deviation = 0.015 ppm). The changes were measured in 3D (H)CANH MAS NMR spectra. **(B)** CSPs upon UCB-FcRn-303 binding to $FcRn_{ECD}$ in 2D planes of 3D (H) CANH spectra with (black) and without (blue) the ligand, both recorded in the presence of 3% DMSO. **(C)** Structural view of UCB-FcRn-303 (red) bound to $FcRn_{ECD}$ with assigned residues in stick representation color-coded according to their CSP ($\Delta\delta < 0.02$, white; $0.02 < \Delta\delta < 0.03$, cyan; $0.03 < \Delta\delta < 0.04$, marine; $0.04 < \Delta\delta$, dark blue). **(D)** Structural view of $FcRn_{ECD}$ in complex with UCB-FcRn-303 (*red*) with the same color-coding of changes in chemical-shifts as in (C). All chemical-shifts can be found in S1 Table, S2 Data, and in the BMRB (accession number 27437). BMRB, Biological Magnetic Resonance Data Bank; CSP, chemical-shift perturbation; FcRn, neonatal Fc receptor; $FcRn_{ECD}$, extracellular domain of the neonatal Fc receptor.

https://doi.org/10.1371/journal.pbio.2006192.g005

strongly affected residues (0.04 ppm < Δδ) are shown in 2D planes of the (H)CANH spectra with and without ligand (Fig 5B). The calculated CSPs shown in Fig 5A are based on the chemical-shift changes in all three spectral dimensions. Large CSPs displayed in Fig 5A may therefore not be obvious from the 2D planes shown in Fig 5B, see $D96_{\beta 2m}$.

As expected, strong effects are seen in the vicinity of the binding pocket of UCB-FcRn-303 observed by X-ray crystallography ($G232_{\alpha\text{-chain}}$, $C48_{\alpha\text{-chain}}$, $G49_{\alpha\text{-chain}}$ and $S52_{\beta 2m}$, Fig 5A and 5C) since the chemical environment of these residues is altered upon binding.

More interestingly, several residues that experienced changes in their chemical-shifts are distant from the binding pocket. These include, for example, $E54_{\alpha\text{-chain}}$ at the C-terminal end of the short α-helix close to the binding region (Fig 5C and 5D). Such an effect could potentially be explained by a small movement of the α-helix. Furthermore, strong CSPs can be observed in a rather remote region composed of loops in β2m, involving $D96_{\beta 2m}$, $G18_{\beta 2m}$, $K19_{\beta 2m}$, $S20_{\beta 2m}$, and $H13_{\beta 2m}$ (Fig 5C and 5D). These residues cluster at the surface close to or at the interface of β2m and the α-chain of two different heterodimers seen in the asymmetric unit (Fig 6A and 6B). A second ligand binding site in this region of $FcRn_{ECD}$ can be excluded since stoichiometric ratios >1 were not observed in SPR experiments or by X-ray crystallography (Fig 2A, S3, S4, S5, S6 Figs, and S1 Data). Interestingly, strong shift changes were observed at comparably long distances from the small molecule binding site. Those strong CSPs may be direct effects of ligand binding, such as introducing a slight displacement of the β2m subunit with respect to the α-chain. Alternatively, it is possible that changes in the protomer–diprotomer equilibrium occur, and thus the chemical-shifts of residues at a potential diprotomer interface are affected. Although we do not observe a stable dimer of heterodimers in solution, a small fraction is present as seen in analytical ultracentrifugation (AUC) experiments (S9 Fig and S4 Text). A diprotomer may also be more highly populated at very high protein concentrations after the applied sedimentation through ultracentrifugation in preparation of 100 kHz MAS experiments. However, the samples with and without ligand have been prepared under identical conditions, making structural effects unrelated to ligand binding unlikely. For a ligand-induced alteration of the equilibrium, long-range structural changes towards the potential diprotomer interface are required, highlighting again the possibility for the occurrence of allosteric effects upon ligand binding.

In the HSA interaction site, a number of strongly affected residues could be found. These included $R12_{\beta 2m}$, $H13_{\beta 2m}$, $C48_{\alpha\text{-chain}}$, $G49_{\alpha\text{-chain}}$, $A50_{\alpha\text{-chain}}$, and $E54_{\alpha\text{-chain}}$ with CSPs around 0.04 ppm or larger (Figs 5A, 6C and S2 Data). Some of these amino acids are close to the binding site of UCB-FcRn-303, but especially $R12_{\beta 2m}$, $H13_{\beta 2m}$, and $E54_{\alpha\text{-chain}}$ are distant to it and may be therefore structurally altered through allosteric effects (Figs 5C and 6C). It is possible that the FcRn–HSA interaction can be modulated with UCB-FcRn-303. The binding site to HSA, however, is located at the possible diprotomer interface and CSPs in this region may be caused by potential ligand-induced changes in the protomer–diprotomer equilibrium of $FcRn_{ECD}$ as discussed above.

Of the NMR assigned residues, only a few from β2m are found in the IgG binding area, such as $R3_{\beta 2m}$ and $T86_{\beta 2m}$ (Fig 6C), for which negligible chemical-shift changes occur (Fig 5A) [46]. In general, residues in the β-sheet region of β2m distant from the binding site or the interface between heterodimers do not exhibit notable CSPs (Fig 5D).

In order to further investigate the potential for allosteric interference with IgG binding, we generated chemical-shift–informed overlays of the two $FcRn_{ECD}$ crystal structures, with and without UCB-FcRn-303. All residues with Δδ < 0.02 ppm (Fig 5A) were used for fitting, including the area around $R3_{\beta 2m}$, $T86_{\beta 2m}$, and $L87_{\beta 2m}$ in β2m that is involved in IgG interaction (Fig 6C), yielding a root mean square deviation (r.m.s.d.) of 0.095 Å. If a movement of the α-helical region of the α-chain could be induced upon ligand binding, it may disseminate

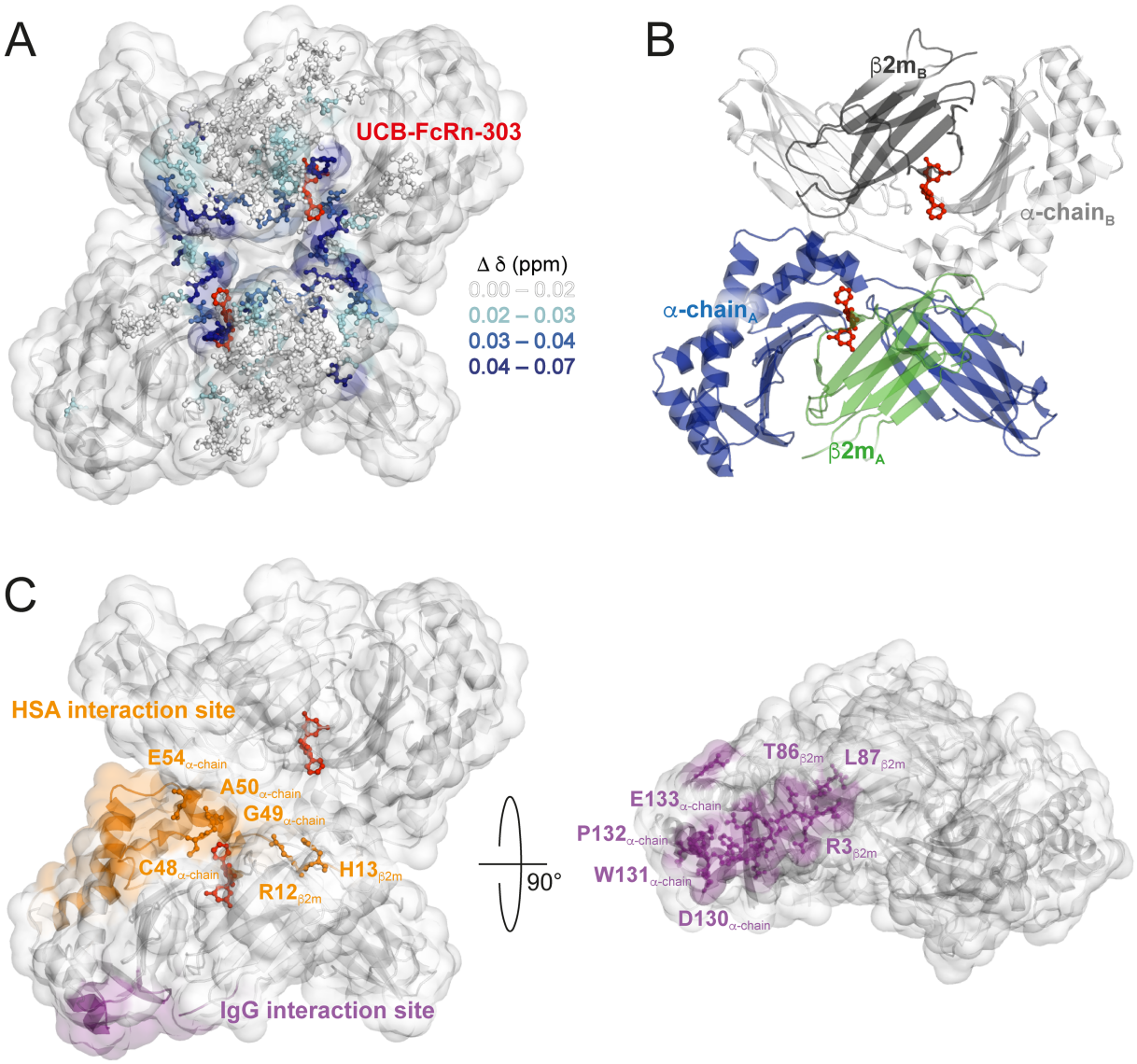

Fig 6. CSPs cluster at the potential $FcRn_{ECD}$ diprotomer interface. (A) CSPs in surface representation of the $FcRn_{ECD}$ diprotomer crystal structure in complex with UCB-FcRn-303 (red), with the same color-coding as in Fig 5. **(B)** For orientation, the $FcRn_{ECD}$ crystal structure is shown in cartoon representation with β2m in green and dark grey and the α-chain molecules in blue and light grey. **(C)** The IgG and HSA interaction sites are depicted in purple and orange, respectively. The highlighted residues are discussed in the text. CSP, chemical-shift perturbation; FcRn, neonatal Fc receptor; $FcRn_{ECD}$, extracellular domain of the neonatal Fc receptor; HSA, Human Serum Albumin; IgG, Immunoglobulin G.

https://doi.org/10.1371/journal.pbio.2006192.g006

towards the loop from $D130_{α\text{-chain}}$ to $E133_{α\text{-chain}}$, which is part of the binding site to IgG (Fig 6C) [46]. Unfortunately, the overlay does not reveal any significant structural changes of α-chain residues close to this loop, except for subtle differences, which we are unable to isolate as a compound-induced effect due to its proximity to crystal packing interactions. Still, the CSPs observed distant to the ligand cavity reveal the potential for allosteric effects in $FcRn_{ECD}$ induced by UCB-FcRn-303 by affecting the HSA interaction site. This provides evidence that binding of an optimized ligand could be aimed at displacing the β2m and α-chain subunits and distally disrupting the IgG binding interface of $FcRn_{ECD}$.

Conclusions

In the context of a druggability study, we identified a compound of <500 Da molecular weight, UCB-FcRn-303, that binds to the extracellular domain of FcRn with low μM affinity. The conserved binding site is located at the interface of β2m and the α-chain, featuring a tunnel-like cavity with solvent access from two different sides. The pocket was identified by computational chemistry methods in a theoretical druggability examination and was corroborated by fragment screening, X-ray crystallography, and NMR spectroscopy. The respective crystal structures show a dimer of heterodimers, with a 1:1 stoichiometry for the ligand/protein complex.

Due to the distance of about 35 Å between the small molecule binding pocket and the site of IgG interaction (Fig 6C), substantial allosteric effects would be required for pharmacologically relevant interference with IgG binding [46]. Such allosteric effects can be monitored by comparing X-ray structures with and without ligand and by NMR spectroscopy via the analysis of ligand-induced CSPs. We therefore established a new approach for testing ligand binding effects on soluble proteins, employing proton-detected 100 kHz MAS NMR spectroscopy on fully protonated $FcRn_{ECD}$. After successful sedimentation of the protein by ultracentrifugation using dedicated filling tools, remarkably well-resolved proton-detected MAS NMR spectra could be obtained and partially assigned. CSPs upon UCB-FcRn-303 binding are observed around the small molecule binding pocket but also distant residues are affected, however, overlapping with the HSA interaction site.

Since a large fraction of residues in β2m towards the IgG binding site and some in the α-chain do not show substantial CSPs (Figs 5A, 6A and 6C), we generated alignments of the two X-ray structures with and without ligand, superposing the nonshifting residues. This approach revealed no substantial changes of residues close to the IgG interaction site upon FcRn-UCB-303 binding, which could modulate the $FcRn_{ECD}$–IgG interaction. It may be envisaged that an optimized ligand could produce a shift of the α-helical region in the α-chain, with potential effects on IgG interaction. Such an optimization could include derivatives with additional functional groups that enter the α-chain/β2m interface and thus produce a slight displacement of the two with respect to each other. Strong CSPs could be observed in the HSA interaction site of $FcRn_{ECD}$, highlighting the potential to achieve a functional modulation of FcRn with UCB-FcRn-303. However, it cannot be fully excluded that changes in oligomeric state of $FcRn_{ECD}$ caused by the ligand under MAS conditions lead to the observed CSPs in this region.

The presented MAS NMR methodology provides an appealing approach for structural investigations of large, soluble proteins expressed in mammalian or other types of eukaryotic cells in which deuteration is challenging, especially in cases when glycosylation is crucial. Moreover, it extends the range of NMR applications to pharmacologically relevant targets, which are often inaccessible by solution-state NMR methods due to size. The MAS NMR approach works with high molecular weight targets and is independent of the physical state of the sample, providing spectral complexity can be handled, e.g., by applying appropriate labelling concepts. This facilitates protein-ligand interaction studies by NMR for any type of protein or biomolecular complex, making previously intractable pharmacological targets accessible, such as the ribosome, G protein-coupled receptors, and the like. Our investigation shows that MAS NMR complements X-ray crystallography in structure-based drug discovery campaigns. It is particularly useful to explore allosteric changes beyond small molecule binding sites, which may be difficult to observe by X-ray crystallography.

Materials and methods

$FcRn_{ECD}$ vector generation

The coding sequences of extracellular domain (ECD) (amino acids 1–297) of human FcRn α-chain and human β2m were synthesized by Entelechon (Entelechon, Regensburg, Germany). The α-chain fragment was cloned into the expression vector pMH (UCB) and the β2m sequence was cloned into pMK (UCB) as HindIII and EcoRI fragments. Both vectors were digested with SalI and NotI and the relevant fragments excised and ligated to generate a vector containing both the α-chain and β2m genes (pM-ECDFcRn-B2M).

The vector was further digested with SalI and a neomycin cassette was ligated in to generate a double gene vector with antibiotic selection (pMFcRnECD-B2M-Neo).

Generation of a $FcRn_{ECD}$ stable mammalian cell line

HEK293 cells were transfected with pMFcRnECD-B2M-Neo using 293fectin (Thermofisher) according to the manufacturer's instructions. Transfected cells were incubated in a static incubator at 37 ˚C and 8% CO_2 for 24 hours. The cells were then diluted to the required concentration with medium supplemented with 0.5 mg/L G418 (Invitrogen) and subsequently divided into 1-mL pools in 24-well plates and incubated in a static incubator at 37 ˚C with 8% CO_2. Every 7 days, the medium was removed from each well and replaced with fresh medium. After a further 14 days, the pools that exhibited cell growth were transferred to 6-well plates. These were expanded up to 50-mL cultures in E250 flasks in shaking incubators. To determine total expression of the $FcRn_{ECD}$ heterodimer composed of β2m and α-chain, batch overgrows were set up and incubated for 10 days.

Samples of the 50-mL batch overgrow supernatants were analyzed for $FcRn_{ECD}$ expression using western blotting. 15 μL of each supernatant was run on a (denatured Tris/Gly gel western blot) alongside known concentrations of purified human FcRn as a control.

The highest expressing pool was expanded (without Neomycin selection) up to 10-L scale in a Wave Bioreactor 20/50 EHT at 37 ˚C, 8% CO_2 for 4 days, at which point the temperature was reduced to 32 ˚C and incubated for a further 6 days. The cell culture was harvested by centrifugation (1,000x *g* for 1 hour) and supernatant put through a 0.22-μm filter.

Purification of $FcRn_{ECD}$ expressed in HEK293 cells

Mammalian cell culture supernatant containing the heterodimer $FcRn_{ECD}$ was concentrated with a 10,000 MWCO membrane using tangential flow filtration (Centramate, Pall) or Amicon stirred cell (Millipore), depending on scale. The sample buffer was exchanged into 50 mM sodium phosphate, pH 5.8, 30 mM NaCl by diluting and concentrating. $FcRn_{ECD}$ was loaded onto a KappaSelect (GE Healthcare) column, which had been preloaded with an IgG4 monoclonal antibody to bind $FcRn_{ECD}$, before washing with 50 mM sodium phosphate, pH 5.8, 30 mM NaCl, and eluting with 50 mM sodium phosphate, pH 8.0, 30 mM NaCl. Elution fractions were analyzed by SDS-PAGE and relevant fractions pooled.

The sample was concentrated using an Amicon spin concentrator (Millipore), 10,000 MWCO membrane. The protein was purified by Gel Filtration with a Superdex 200 (GE Healthcare) column using 25 mM sodium phosphate, pH 7.4, 100 mM NaCl. Peak fractions were analyzed by SDS-PAGE before pooling and concentrating if required.

SPR analysis

SPR was carried out using BIAcore 4000 instruments (GE Healthcare). Reagents including CM5 sensor chips, *N*-hydroxysuccinimide (NHS), *N*-ethyl-*N*-(3-dimethylaminopropyl)

carbodiimide (EDC), and ethanolamine HCl, 10 mM sodium acetate buffers (pH 5.0, pH 4.5) and HBS-P (10x buffer) were obtained from GE Healthcare.

$FcRn_{ECD}$ was diluted into 10 mM sodium acetate buffer, pH 5.0 and immobilized on a CM5 Sensor Chip via amine coupling chemistry to a capture level of approxmimately 4,000 response units. Compounds were screened in a 10-point titration from 200 μM, at 2% DMSO, pH 6.0, and the surface was re-immobilized after each 384-well plate. Injections were performed at a flow rate of 10 μL/min.

All data were double-referenced for blank injections and reference surface, following standard procedures. Both data processing and fitting were performed using Activity Base template protocols developed in house.

Fragment library screening using ^{19}F NMR

A library of approximately 1,100 fluorine-containing fragments were cocktailed into groups of 12 ensuring no overlap of ^{19}F signals. Cocktails were initially prepared at a concentration of 4.2 mM in d6-DMSO and diluted to 800 μM in PBS pH 7.4 before a final dilution to 40 μM ligand concentration (1% d6-DMSO) in either PBS containing 10% D_2O (for control samples) or 20 μM $FcRn_{ECD}$ containing 10% D_2O (for protein samples). NMR spectra were acquired at 25 ˚C on a Bruker 600 MHz AVIII-HD spectrometer equipped with a QCI-F cryoprobe and a SampleJet autosampler. Data were collected using a CPMG pulse sequence with a total echo time of 160 ms across a sweep width of 126 ppm with an acquisition time of 1 s. All spectra were processed using TopSpin 3.2. Fragments were considered binders to $FcRn_{ECD}$ when the ^{19}F signal intensity was significantly reduced in the spectra with $FcRn_{ECD}$ present compared to the spectra recorded in the absence of protein.

Fragment library screening using STD NMR

STD NMR samples were prepared with a ligand to protein ratio of 50:1 (500 μM ligand, 10 μM $FcRn_{ECD}$) in 500 μL phosphate buffered saline, pH 7.4 (90% H_2O, 10% D_2O) with 5% d6-DMSO to help solubilize the ligand. STD NMR spectra were recorded using a Bruker Avance III HD 600 MHz spectrometer equipped with a 5 mm QCI-F Cryoprobe. Data were acquired and processed using the standard Bruker software and were collected at 298 K. The protein was saturated in the methyl region of the spectrum at 0 ppm, and off-resonance saturation was performed at 33 ppm. A series of 120 EBurp2 pulses (50 ms each) were applied with a 4-μs delay between each pulse, resulting in total saturation time of 6 s. Protein signals were removed by applying a spinlock of 100 ms. Interleaved on- and off-resonance data were recorded, processed separately, and then the difference spectra obtained by subtracting the on- from the off-resonance spectra. Data were zero filled once and an exponential multiplication window function applied (LB 2 Hz).

Plasmid construction of $FcRn_{ECD}$ for expression in Sf9 insect cells

The parent construct for α-chain/β2m expresses two Open Reading Frames (ORFs) within one baculovirus multiple-target expression plasmid, pBacugs4X-1. Protein targets are based on the following amino acid sequences (both α-chain and β2m each contain their native leaders): α-chain 1–297 based on NCBI reference sequence NP_004098, β2m 1–119 based on NCBI reference sequence NP_004039. Codons for both ORFs were engineered by GeneComposer for highly expressed baculovirus genes, such that BamHI, HindIII, BglII, and EcoRI restriction sites were eliminated from the inserts to facilitate cloning [65]. Both genes, including flanking restriction sites, were synthesized at GeneArt. The ORF for α-chain was cloned behind the polyhedrin promoter via unique BamHI and HindIII sites; in this case, the BamHI site

preceded the signal sequence while HindIII followed the sequence "TGAT" such that two stops are introduced after the C-terminal residue. The ORF for β2m was cloned behind the p10 promoter via unique BglII and EcoRI sites; the BglII site preceded the signal sequence, while EcoRI followed the sequence "TGATAA" such that two stops are introduced after the C-terminal residue. Using this cloning scheme, polyhedrin and p10 promoters are arranged in divergent/opposing orientations within the baculovirus transfer vector. ORFs were sequence verified prior to the commencement of expression studies.

Expression of $FcRn_{ECD}$ in Sf9 insect cells

The α-chain/β2m construct was transfected into Sf9 insect cells (Expression Systems) using BestBac 2.0, v-cath/chiA Deleted Linearized Baculovirus DNA (Expression Systems, Cat#-91-002). Virus from each transfection was amplified through 3 rounds to produce virus stock for large-scale production. The large-scale preparations were grown in ESF921 medium (Expression Systems, Cat#96–001). Large-scale preparations were infected using the titerless infected-cells preservation and scale-up (TIPS) method [66]. Approximately 10^6 Tni cells (*Trichopulsia ni*, Expression Systems) per mL were infected using 1 mL of TIPS cells. Secreted proteins were harvested after 2–3 days by Tangential Flow Filtration (Spectrum KrosFlo, 0.2 μm filter Cat# P-NO2-E20U-05-N).

Purification of $FcRn_{ECD}$ expressed in Sf9 insect cells

Harvested baculovirus medium (*Trichoplusia ni*) containing secreted $FcRn_{ECD}$ was concentrated 10-fold and buffer exchanged (50 mM sodium phosphate pH 5.8 and 30 mM NaCl via Tangential Flow Filtration (TFF) (Spectrum Labs). The concentrated medium was centrifuged using a JA-10 rotor at 9,000 RPM for 15 minutes at 4 ˚C and then filtered through a 0.2 μm bottle top filter. Three complete EDTA free protease inhibitor tablets were added to the concentrated media prior to chromatography. The filtered concentrated medium was applied to 35 mL of IgG Sepharose FF resin (GE Healthcare) equilibrated with 50 mM sodium phosphate buffer, pH 5.8, and 30 mM NaCl (Sigma) and rotated end over end for one hour at 4 ˚C. The resin was then poured into a gravity flow column and washed with 10 column volumes of the same equilibration buffer. $FcRn_{ECD}$ was eluted from the resin with eight column volumes of 50 mM sodium phosphate buffer pH 8.0 and 30 mM NaCl. The elution fractions containing $FcRn_{ECD}$ were pooled and loaded onto two 5-mL HiTrap Q FF columns (GE Healthcare) and eluted over a 1 M NaCl gradient. The fractions of interest were pooled and glycerol was added to a final concentration of 10%. The pool was concentrated to 15 mg/mL via centrifugal concentration (Amicon Regenerated Cellulose, 10 kDa MWCO, Millipore) and further purified via size exclusion chromatography over a HiLoad 16/600 Superdex 200 pg (GE Healthcare) column in 50 mM HEPES (4-(2-hydroxyethyl)-1-piperazineethanesulfonic acid) pH 7.0 and 75 mM NaCl. The fractions containing $FcRn_{ECD}$ were pooled and concentrated for crystallography via centrifugal concentration (Amicon Regenerated Cellulose, 10 kDa MWCO, Millipore) to 9.9 mg/mL prior to being aliquoted and flash frozen in liquid nitrogen for later use in crystallization experiments.

Crystallization of $FcRn_{ECD}$

In order to search for crystallization conditions for $FcRn_{ECD}$ expressed in insect cells, sitting-drop vapor diffusion crystallization trials were set up at 291 K using a variety of commercial spare-matrix (Rigaku Reagents: JCSG+, Wizard 1/2, Wizard 3/4; Hampton Research: Crystal Screen HTIndex; Molecular Dimensions: PACT, Morpheus, Proplex; Microlytics: MCSG1) using 0.4 μL of protein solution at 5 mg/mL that were mixed with 0.4 μL of reservoir solution

and equilibrated against 80 μL of reservoir solution. The initial crystallization trials produced small kite crystals in several conditions that contain PEG 3350, PEG 6000, or PEG 8000 at low pH. Low pH crystals of $FcRn_{ECD}$ were produced in an optimized crystallization condition screen (Rigaku) containing 12%–16% PEG 6000, 100 mM Citric Acid/Ammonium citrate tribasic pH 3.00–3.09. Crystals of $FcRn_{ECD}$ appeared within 24 hours and grew larger overtime, typically to 50–150 microns in size. The crystals were harvested using 20% glycerol as a cryoprotectant and flash frozen in liquid nitrogen prior to data collection.

Additionally, small rod-like crystals appeared in a single condition at a significantly higher pH (condition PACT H3, 100 mM Bis-Tris Propane/HCl pH 8.5, 200 mM NaI, and 20% PEG 3350) [67]. High/neutral pH crystals of $FcRn_{ECD}$ were produced in optimized crystallization condition containing 100 mM Bis-Tris Propane/HCl pH 8.5, 200 mM NaI, and 20% PEG 3350. Crystals of $FcRn_{ECD}$ appeared within 48 hours and grew larger overtime, typically greater than 150 microns in size. The crystals were harvested using 20% ethylene glycol and flash frozen in liquid nitrogen prior to data collection. To obtain compound bound crystals, apo $FcRn_{ECD}$ crystals grown at pH 3 were soaked for three days in buffer containing 0.1 M Citric Acid/NaOH at pH 3.0, 20% w/v PEG 6000, 20% glycerol, and 12.5–20 mM compound dissolved in 100% DMSO. For crystallization of the UCB-FcRn-303 bound structure of $FcRn_{ECD}$, protein expressed in Sf9 insect cells was used.

Structure determination by X-ray crystallography

Datasets were collected at Canadian Light Source (CLS) on beamline 08ID-1 (CMCF) equipped with a Rayonix MX300 CCD X-ray detector and Advanced Photon Source (APS) on beamline 21-ID-F (LS-CAT) equipped with a Marmosaic 225 CCD X-ray detector. Diffraction data were reduced and scaled with XDS/XSCALE [68]. The structures of $FcRn_{ECD}$ at low and high/neutral pH were solved by molecular replacement using a pre-existing structure of the complex. A significant portion of the structure required remodeling; therefore, Phenix.autobuild was run to generate a starting structure for further refinement. All structures were refined using iterative cycles of TLS and restrained refinement with Phenix.refine and model-building using the Crystallographic Object-Oriented Toolkit (COOT; Version 0.8.1-pre) and were validated using Molprobity prior to deposition in the PDB (IDs 6C97, 6C98, 6C99) [69–73]. Diffraction data and refinement statistics for apo $FcRn_{ECD}$ at pH 3 and both ligand bound structures are listed in S2 Table.

Molecular dynamics simulation

The $FcRn_{ECD}$ structures at pH 3 and pH 8.5 were used as the starting points for molecular dynamics simulation, after adding hydrogen. Protonation states and missing loops were predicted with Maestro (Schrödinger LLC). The structure was solvated in a dodecahedron such that no protein atom was within 10 Å of the edge of the solvent. Monatomic ions were added to a salt concentration of 0.15 M. All simulations were 1,000 ns in length and were carried out with GROMACS 4.6.2 [74]. Particle mesh Ewald was used for long-range electrostatics along with 10 Å cutoffs for Coulomb and Lennard–Jones potential functions.

Expression of fully protonated [^{13}C,^{15}N]-labeled $FcRn_{ECD}$ for NMR experiments

$FcRn_{ECD}$ was expressed using a stable HEK293 cell line, as described above, but the growth media was replaced with Bioexpress 6000 media (Cambridge Isotope Laboratories).

Acquisition of 2D ^{15}N-^{1}H TROSY solution-state NMR spectrum on fully protonated [^{13}C,^{15}N]-labeled $FcRn_{ECD}$

The solution-state 2D ^{15}N-^{1}H TROSY spectrum was acquired from a 0.35-mL sample of 300 μM [^{13}C,^{15}N]-labeled $FcRn_{ECD}$ in a 25 mM Na_2HPO_4, 100 mM NaCl, 50 μM EDTA, 0.02% (w/v) NaN_3 buffer at pH 7.4 containing 5% D_2O/95% H_2O [49]. NMR data were acquired at 35 ˚C on a 600 MHz Bruker AVIII HD spectrometer fitted with a cryogenically cooled probe. The spectrum was acquired for 40 minutes with acquisition times of 40 ms in F_1 (^{15}N) and 60 ms in F_2 (^{1}H). It was processed using Topspin 3.5 (Bruker Biospin Ltd) with linear prediction used to extend the effective acquisition time to 60 ms in F_1.

Sedimentation of $FcRn_{ECD}$ by ultracentrifugation for NMR experiments using fast MAS

A 0.5-mL sample of 100 μM [^{13}C,^{15}N]-labeled $FcRn_{ECD}$ in a 25 mM Na_2HPO_4, 100 mM NaCl, 50 μM EDTA, 0.02% (w/v) NaN_3 buffer at pH 7.4 containing 3% DMSO was directly ultracentrifuged into a 0.7 mm MAS NMR rotor at 100,000 x *g* and 4 ˚C for 40 hours using a swinging bucket ultracentrifuge rotor. Dedicated home-made filling tools were used for this step. Both bottom and top caps of the 0.7 mm MAS rotor were glued to avoid the loss of liquid or removal of caps during MAS. Excess protein and liquid after ultracentrifugation was removed before closing the 0.7 mm NMR MAS rotor. For experiments to detect CSPs, 3 mM UCB-FcRn-303 was added to a 0.5-mL sample of 100 μM [^{13}C,^{15}N]-labeled $FcRn_{ECD}$ in a 25 mM Na_2HPO_4, 100 mM NaCl, 50 μM EDTA, 0.02% (w/v) NaN_3 buffer at pH 7.4 containing 3% DMSO (ligand:protein ratio of 30:1). The ligand-bound sample was sedimented into a second 0.7 mm MAS rotor under the same conditions as the ligand-free sample.

Proton-detected NMR experiments using fast MAS on fully protonated [^{13}C,^{15}N]-labeled $FcRn_{ECD}$

All MAS NMR experiments were performed on a Bruker AVANCE III 850 MHz spectrometer. The spectra were recorded at 80, 90, or 100 kHz MAS with a triple-resonance 0.7 mm MAS probe (Bruker) and referenced to 4,4-dimethyl-4-silapentane-1-sulfonic acid (DSS) (see S3 Table for experimental parameters). The sample temperature of 283 K was monitored by the frequency of the water resonance line. To achieve this sample temperature, the sample was cooled during MAS using nitrogen gas through a cooling unit (BCU II, Bruker) in strong mode with the gas flow set to 400 L/h. (H)NH, (H)CANH, (H)CA(CO)NH, and (H)CBCANH spectra were recorded using Cross Polarization (CP) (heteronuclear transfers) and DREAM (homonuclear transfers) magnetization transfer steps according to the procedures described in Penzel and colleagues [61,75,76]. All spectra were processed with Topspin 3.5 (Bruker) and analyzed with CCPNmr Analysis v. 2.4.2. [77]. All assigned chemical-shifts and observed CSPs are listed in S1 Table and S2 Data, and are deposited in the Biological Magnetic Resonance Data Bank (BMRB) (accession number 27437).

Analytical ultracentrifugation of $FcRn_{ECD}$

Sedimentation velocity experiments were performed at 8 ˚C and 35,000 rpm with an An-60Ti rotor using 12-mm Epon 2-sector centerpieces. For each of the three measurements at different $FcRn_{ECD}$ concentrations (4 μM, 14 μM, and 52 μM), a 400-μL sample in 10 mM Na_2HPO_4, 137 mM NaCl, 2.7 mM KCl, 1.8 mM KH_2PO_4 buffer at pH 7.2 was used. The data were analyzed and plotted with the GUSSI implementation and SEDFIT [78].

Experimental and analytical details for synthetic analogues

All solvents and reagents were used as received from commercial suppliers, unless noted otherwise. The compounds were named using the Biovia Draw 2016 package (IUPAC).

NMR spectra were recorded on a Bruker Avance III HD 500 MHz or 250 MHz spectrometer.

The chemical-shifts (δ) reported are given in parts per million (ppm) and the coupling constants (J) are in Hertz (Hz). The spin multiplicities are reported as s = singlet, d = doublet, t = triplet, q = quartet, dd = doublet of doublet, ddd = doublet of doublet of doublet, dt = doublet of triplet, td = triplet of doublet, and m = multiplet.

uPLC-MS was performed on a Waters Acquity UPLC system coupled to a Waters Acquity PDA detector, an ELS detector and an MSD (Scan Positive: 150–850). Method (pH 3): Phenomenex Kinetix-XB C18 (2.1 x 100 mm, 1.7 μm) column. Elution with a linear gradient of Water + 0.1% Formic acid and Acetonitrile + 0.1% Formic acid at a flow rate of 0.6 mL/min. Chiral SFC analysis: Waters Thar 3100 SFC system connected to Waters 2998 PDA detector, Chiralcel OD-H 25 cm. Chiral SFC separation: Water Thar SFC system with a Waters Thar FDM pump, Waters Thar Alias autoinjector, Waters Thar fraction collector and a Waters 2998 PDA detector.

***(R)* and *(S)* 1-[7-(3-Fluorophenyl)-5-methyl-4,7-dihydro-[1,2,4]triazolo[1,5-a]pyrimidin-6-yl]ethanone (UCB-FcRn-84) (S10 Fig).** 1-[7-(3-fluorophenyl)-5-methyl-4,7-dihydro-[1,2,4]triazolo[1,5-a]pyrimidin-6-yl]ethanone (CAS 691368-95-3) was purchased as a racemate from Life Chemicals and the mixture separated by chiral chromatography using a Chiralpak AD phase (100*500), 300 mL/min with an heptane/isopropanol (8/2) system. 1.21 G of starting material led to respectively 577 mg and 588 mg of separated isomers. Chiral analytical SFC: RT = 8.22 min, 100% ee; RT = 10.40 min, 100% ee.

1-[7-(3,5-Difluorophenyl)-5-methyl-4,7-dihydro-[1,2,4]triazolo[1,5-a]pyrimidin-6-yl] ethanone (S11 Fig). A stirred solution of 3,5-difluorobenzaldehyde (0.1 mL, 0.946 mmol), pentane-2,4-dione (0.146 mL, 1.42 mmol, 1.5 eq.), and *4H*-1,2,4-triazol-3-amine (119 mg, 1.42 mmol, 1.5 eq.) in N,N-dimethylformamide (1.5 mL) was irradiated in a microwave oven (up to 200 W) at 150 ˚C for 60 min. The reaction mixture was left to cool down to ambient temperature and water (6 mL) was added leading to the formation of a precipitate. The resulting solid was collected by filtration, rinsed with water (2 x 1 mL) and cyclohexane (2 x 1 mL), then triturated in hot acetonitrile (1 mL) and dried *in vacuo* to afford 94 mg (34% yield) of the title compound as a pale yellow solid.

The ^{1}H NMR analysis yielded (500 MHz, DMSO-d6) δ 10.89 (s, 1H), 7.70 (s, 1H), 7.14 (t, J = 9.1 Hz, 1H), 6.98 (d, J = 6.3 Hz, 2H), 6.46 (s, 1H), 2.46 (s, 3H), 2.20 (s, 3H). uPLC-MS: $[M+H]^{+}$ m/z = 291, RT = 2.38 min (99%).

***(R)* and *(S)* 1-[7-(3,5-Difluorophenyl)-5-methyl-4,7-dihydro-[1,2,4]triazolo[1,5-a]pyrimidin-6-yl]ethanone (S12 Fig).** The racemate (50 mg) was separated by chiral preparative chromatography on a Chiralpak ASV (50*490) phase, 80 mL/min with a heptane/ethanol (9/1) system to afford 24 mg and 19 mg of the pure enantiomers. Chiral analytical SFC: RT = 10.89 min, 100% ee; RT = 15.16 min, 97.8% ee.

Methyl 7-(3,5-difluorophenyl)-5-(3-pyridyl)-4,7-dihydro-[1,2,4]triazolo[1,5-a]pyrimidine-6-carboxylate (UCB-FcRn-303) (S13 Fig). To a stirred solution of 3,5-difluorobenzaldehyde (150 mg, 1.06 mmol), methyl 3-oxo-3-(pyridin-3-yl)propanoate (265 mg, 1.48 mmol, 1.4 eq.), and *4H*-1,2,4-triazol-3-amine (124 mg, 1.48 mmol, 1.4 eq.) in N,N-dimethylformamide (1.5 mL) was added chloro(trimethyl)silane (0.268 mL, 2.11 mmol) dropwise. The reaction mixture was then irradiated in a microwave oven (up to 200 W) at 130 ˚C for 60 minutes. The reaction mixture was left to cool down to ambient temperature and water (6 mL) was

added leading to the formation of a precipitate. The resulting solid was collected by filtration, rinsed with water (2 x 1 mL) and cyclohexane (2 x 1 mL) then recrystallized from acetonitrile (2 mL) and dried in vacuo to afford 238 mg (59% yield) of the title compound as a pale yellow solid. The ^{1}H NMR analysis yielded (500 MHz, DMSO-d6) δ 11.18 (s, 1H), 8.67–8.61 (m, 2H), 7.92 (dt, J = 7.8, 1.9 Hz, 1H), 7.75 (s, 1H), 7.48 (dd, J = 7.8, 4.9 Hz, 1H), 7.20 (tt, J = 9.2, 2.2 Hz, 1H), 7.16–7.10 (m, 2H), 6.50 (s, 1H), 3.27 (s, 3H). uPLC-MS: $[M+H]^{+}$ m/z = 370, RT = 2.12 min (97%).

Supporting information

S1 Fig. Ligandability assessments on $FcRn_{ECD}$ and predicted small molecule binding sites. At low pH binding sites with the capacity to yield high affinity binding are restricted to the dimer interface, with the region described as either one large or three distinct pockets (pockets A-C). At neutral and basic pH, transient sites arise at the albumin binding site, between the α1 and α2 helices (D), and between the β2m and the α3 domain (E). β2m, β2-microglobulin; $FcRn_{ECD}$, extracellular domain of the neonatal Fc receptor.
(JPG)

S2 Fig. Evolutionary conservation of $FcRn_{ECD}$. (A) The pH 3 structure of the human $FcRn_{ECD}$ heterodimer is colored to illustrate sequence conservation in vertebrate orthologues. Universally conserved residues are colored white; mutated residues are shown in red, with the color intensity indicating the BLOSUM62 score of the worst-matching substitution (darker red = more radical amino acid change away from the human residue). Species included in the analysis are: *Pan troglodytes*, *Gorilla gorilla*, *Pongo pygmaeus*, *Macaca mulatta*, *Callithrix aurita*, *Microcebus murinus*, *Otolemur garnettii*, *Mus musculus*, *Rattus norvegicus*, *Cavia porcellus*, *Oryctolagus cuniculus*, and *Bos taurus*. Mutations occur throughout the α-chain and β2m. Areas of clear conservation include the interface of α-chain and β2m and the central cavity that was detected in the SiteMap analysis. **(B)** For reference, human $FcRn_{ECD}$ from the HSA-bound FcRn structure (PDB code 4N0F) has been colored to highlight residues that constitute the surfaces with the Fc moiety of IgG (magenta) and HSA (orange), the α-chain is shown in green and β2m in cyan. β2m, β2-microglobulin; FcRn, neonatal Fc receptor; $FcRn_{ECD}$, extracellular domain of the neonatal Fc receptor; HSA, Human Serum Albumin; IgG, Immunoglobulin G; PDB, Protein Data Bank.
(TIF)

S3 Fig. UCB-FcRn-84 binds with K_D approximately 80 μM to $FcRn_{ECD}$ as measured by SPR. The numerical values can be found in S1 Data. FcRn, neonatal Fc receptor; $FcRn_{ECD}$, extracellular domain of the neonatal Fc receptor; SPR, Surface Plasmon Resonance.
(TIF)

S4 Fig. Crystal structure of the compound UCB-FcRn-84 bound to $FcRn_{ECD}$. The compound binds at the interface of β2m (green) and the α-chain (blue). Also in this crystal structure, a second heterodimer can be found in the asymmetric unit (grey). β2m, β2-microglobulin; FcRn, neonatal Fc receptor; $FcRn_{ECD}$, extracellular domain of the neonatal Fc receptor.
(JPG)

S5 Fig. Crystal structure of UCB-FcRn-303 bound to $FcRn_{ECD}$. The compound occupies the same binding pocket as UCB-FcRn-84 at the interface of β2m (green) and the α-chain (blue). The binding region is a tunnel-like cavity extending through the protein. Again, a second

heterodimer is found in the crystal structure (depicted in grey). β2m, β2-microglobulin; FcRn, neonatal Fc receptor; $FcRn_{ECD}$, extracellular domain of the neonatal Fc receptor.
(JPG)

S6 Fig. UCB-FcRn-303 binds with K_D = 2.4 μM to $FcRn_{ECD}$ as measured by SPR. The numerical values can be found in S1 Data. FcRn, neonatal Fc receptor; $FcRn_{ECD}$, extracellular domain of the neonatal Fc receptor; SPR, Surface Plasmon Resonance.
(TIF)

S7 Fig. The CH2 and CH3 domains (red) of IgG heavy chain in complex with $FcRn_{ECD}$ (α-chain in blue, β2m in green) (PDB code 1FRT) show overlap with symmetry related copies (dark and medium grey) of ligand-free $FcRn_{ECD}$ (light grey) [46]. β2m, β2-microglobulin; $FcRn_{ECD}$, extracellular domain of the neonatal Fc receptor; IgG, Immunoglobulin G; PDB, Protein Data Bank.
(JPG)

S8 Fig. Comparison of $FcRn_{ECD}$ ^{15}N-^{1}H NMR spectra in solution and after sedimentation. **(A)** 2D ^{15}N-^{1}H correlation using TROSY of fully protonated [^{13}C,^{15}N]-labeled $FcRn_{ECD}$ measured in solution. **(B)** Overlay of the spectrum shown in (A) (orange) with a 2D ^{15}N-^{1}H spectrum of sedimented fully protonated [^{13}C,^{15}N]-labeled $FcRn_{ECD}$ recorded at 100 kHz MAS (black). $FcRn_{ECD}$, extracellular domain of the neonatal Fc receptor; MAS, magic-angle-spinning.
(JPG)

S9 Fig. Analytical ultracentrifugation of $FcRn_{ECD}$. Sedimentation velocity experiments at three different concentrations (52 μM, grey; 14 μM, red; 4 μM, blue) exhibit protein concentration dependent peaks at 3.5 S, 5.1 S, and 5.3 S. $FcRn_{ECD}$, extracellular domain of the neonatal Fc receptor.
(JPG)

S10 Fig. *(R)* and *(S)* 1-[7-(3-Fluorophenyl)-5-methyl-4,7-dihydro-[1,2,4]triazolo[1,5-a]pyrimidin-6-yl]ethanone (UCB-FcRn-84). FcRn, neonatal Fc receptor.
(PDF)

S11 Fig. 1-[7-(3,5-Difluorophenyl)-5-methyl-4,7-dihydro-[1,2,4]triazolo[1,5-a]pyrimidin-6-yl]ethanone.
(PDF)

S12 Fig. *(R)* and *(S)* 1-[7-(3,5-Difluorophenyl)-5-methyl-4,7-dihydro-[1,2,4]triazolo[1,5-a] pyrimidin-6-yl]ethanone.
(PDF)

S13 Fig. Methyl 7-(3,5-difluorophenyl)-5-(3-pyridyl)-4,7-dihydro-[1,2,4]triazolo[1,5-a] pyrimidine-6-carboxylate (UCB-FcRn-303). FcRn, neonatal Fc receptor.
(PDF)

S1 Data. Numerical values of SPR experiments in S3 and S6 Figs.
(XLSX)

S2 Data. Observed chemical-shifts and CSP values of $FcRn_{ECD}$ with and without UCB-FcRn-303 as shown in Fig 5. β2m, β2-microglobulin; CSP, chemical-shift perturbation; FcRn, neonatal Fc receptor; $FcRn_{ECD}$, extracellular domain of the neonatal Fc receptor; MHC1, class I major histocompatibility complex.
(XLSX)

S1 Table. ^{1}H, ^{15}N, $^{13}C\alpha$, and $^{13}C\beta$ chemical-shifts observed in proton-detected NMR experiments at 100 kHz MAS on sedimented fully protonated [^{13}C,^{15}N]-labeled $FcRn_{ECD}$. They are compared to the corresponding chemical-shifts (Beerbaum and colleagues) of [^{2}H,^{13}C,^{15}N]-labeled β2m in MHC1 complexes measured in solution-state NMR [63]. Amino acids of the α-chain are depicted in blue, β2m residues in green. β2m, β2-microglobulin; $FcRn_{ECD}$, extracellular domain of the neonatal Fc receptor; MAS, magic-angle-spinning.
(PDF)

S2 Table. X-ray diffraction data and refinement statistics.
(PDF)

S3 Table. Experimental parameters for proton-detected MAS NMR experiments on fully protonated [^{13}C,^{15}N]-labeled $FcRn_{ECD}$. $FcRn_{ECD}$, extracellular domain of the neonatal Fc receptor; MAS, magic-angle-spinning.
(PDF)

S1 Text. Ligandability assessments on $FcRn_{ECD}$. $FcRn_{ECD}$, extracellular domain of the neonatal Fc receptor.
(PDF)

S2 Text. UCB-FcRn-303 binds in a tunnel-like cavity with low μM affinity. FcRn, neonatal Fc receptor.
(PDF)

S3 Text. $FcRn_{ECD}$ adopts a similar structure in solution and sedimented samples. $FcRn_{ECD}$, extracellular domain of the neonatal Fc receptor.
(PDF)

S4 Text. Analytical ultracentrifugation reveals a small fraction of dimers of heterodimers at higher concentrations of $FcRn_{ECD}$ in solution. $FcRn_{ECD}$, extracellular domain of the neonatal Fc receptor.
(PDF)

S5 Text. Observed chemical-shifts of $FcRn_{ECD}$ in MAS NMR experiments. FcRn, neonatal Fc receptor; MAS, magic-angle-spinning.
(PDF)

Acknowledgments

Excellent technical support by Nils Cremer is kindly acknowledged.

Author Contributions

Conceptualization: Daniel Stöppler, Alex Macpherson, Richard Taylor, Beat H. Meier, Hartmut Oschkinat, Alastair D. Lawson.

Data curation: Daniel Stöppler, Alex Macpherson, Susanne Smith-Penzel, David Fox, III.

Formal analysis: Daniel Stöppler, Alex Macpherson, Nicolas Basse, Lorna C. Waters, David Fox, III, Mark D. Carr, Beat H. Meier, Hartmut Oschkinat.

Funding acquisition: Beat H. Meier, Hartmut Oschkinat, Alastair D. Lawson.

Investigation: Daniel Stöppler, Alex Macpherson, Susanne Smith-Penzel, Nicolas Basse, Fabien Lecomte, Hervé Deboves, Richard D. Taylor, Tim Norman, John Porter, Lorna C. Waters, Marta Westwood, Ben Cossins, Katharine Cain, James White, Robert Griffin,

Christine Prosser, Sebastian Kelm, Amy H. Sullivan, David Fox, III, Mark D. Carr, Alistair Henry, Richard Taylor, Beat H. Meier, Hartmut Oschkinat, Alastair D. Lawson.

Methodology: Daniel Stöppler, Alex Macpherson, Susanne Smith-Penzel, Nicolas Basse, Fabien Lecomte, Hervé Deboves, Richard D. Taylor, Tim Norman, John Porter, Lorna C. Waters, Marta Westwood, Ben Cossins, Katharine Cain, James White, Robert Griffin, Christine Prosser, Sebastian Kelm, Amy H. Sullivan, David Fox, III, Mark D. Carr, Alistair Henry, Richard Taylor, Beat H. Meier, Hartmut Oschkinat, Alastair D. Lawson.

Project administration: Daniel Stöppler, Alex Macpherson, Nicolas Basse, Alistair Henry, Richard Taylor, Hartmut Oschkinat, Alastair D. Lawson.

Supervision: Daniel Stöppler, Alex Macpherson, Nicolas Basse, Alistair Henry, Richard Taylor, Beat H. Meier, Hartmut Oschkinat, Alastair D. Lawson.

Validation: Daniel Stöppler, Alex Macpherson, David Fox, III, Mark D. Carr, Hartmut Oschkinat, Alastair D. Lawson.

Visualization: Daniel Stöppler, Alex Macpherson, Marta Westwood.

Writing – original draft: Daniel Stöppler, Alex Macpherson.

Writing – review & editing: Daniel Stöppler, Alex Macpherson, Susanne Smith-Penzel, Nicolas Basse, Fabien Lecomte, Hervé Deboves, Richard D. Taylor, Tim Norman, John Porter, Lorna C. Waters, Marta Westwood, Ben Cossins, Katharine Cain, James White, Robert Griffin, Christine Prosser, Sebastian Kelm, Amy H. Sullivan, David Fox, III, Mark D. Carr, Alistair Henry, Richard Taylor, Beat H. Meier, Hartmut Oschkinat, Alastair D. Lawson.

References

1. Verdonk ML, Hartshorn MJ. Structure-guided fragment screening for lead discovery. Curr Opin Drug Discov Devel. 2004; 7: 404–410. PMID: 15338949
2. Siegal G, Ab E, Schultz J. Integration of fragment screening and library design. Drug Discov Today. 2007; 12: 1032–1039. https://doi.org/10.1016/j.drudis.2007.08.005 PMID: 18061882
3. Magee TV. Progress in discovery of small-molecule modulators of protein-protein interactions via fragment screening. Bioorg Med Chem Lett. 2015; 25: 2461–2468. https://doi.org/10.1016/j.bmcl.2015.04.089 PMID: 25971770
4. Ludlow RF, Verdonk ML, Saini HK, Tickle IJ, Jhoti H. Detection of secondary binding sites in proteins using fragment screening. Proc Natl Acad Sci USA. 2015; 112: 15910–15915. https://doi.org/10.1073/pnas.1518946112 PMID: 26655740
5. Brambell FW, Hemmings WA, Morris IG. A theoretical model of γ-globulin catabolism. Nature. 1964; 203: 1352–1354. PMID: 14207307
6. Raghavan M, Bonagura VR, Morrison SL, Bjorkman PJ. Analysis of the pH dependence of the neonatal Fc receptor/immunoglobulin G interaction using antibody and receptor variants. Biochemistry. 1995; 34: 14649–14657. PMID: 7578107
7. Raghavan M, Chen MY, Gastinel LN, Bjorkman PJ. Investigation of the interaction between the class I MHC-related Fc receptor and its immunoglobulin G ligand. Immunity. 1994; 1: 303–315. PMID: 7889418
8. Chaudhury C, Mehnaz S, Robinson JM, Hayton WL, Pearl DK, Roopenian DC, et al. The major histocompatibility complex-related Fc receptor for IgG (FcRn) binds albumin and prolongs its lifespan. J Exp Med. 2003; 197: 315–322. https://doi.org/10.1084/jem.20021829 PMID: 12566415
9. Borvak J, Richardson J, Medesan C, Antohe F, Radu C, Simionescu M, et al. Functional expression of the MHC class I-related receptor, FcRn, in endothelial cells of mice. Int Immunol. 1998; 10: 1289–1298. PMID: 9786428
10. Ober RJ, Martinez C, Lai X, Zhou J, Ward ES. Exocytosis of IgG as mediated by the receptor, FcRn: an analysis at the single-molecule level. Proc Natl Acad Sci USA. 2004; 101: 11076–11081. https://doi.org/10.1073/pnas.0402970101 PMID: 15258288

11. Ward ES, Martinez C, Vaccaro C, Zhou J, Tang Q, Ober RJ. From sorting endosomes to exocytosis: association of Rab4 and Rab11 GTPases with the Fc receptor, FcRn, during recycling. Mol Biol Cell. 2005; 16: 2028–2038. https://doi.org/10.1091/mbc.E04-08-0735 PMID: 15689494

12. Kim JK, Tsen MF, Ghetie V, Ward ES. Localization of the site of the murine IgG1 molecule that is involved in binding to the murine intestinal Fc receptor. Eur J Immunol. 1994; 24: 2429–2434. https://doi.org/10.1002/eji.1830241025 PMID: 7925571

13. Ober RJ, Martinez C, Vaccaro C, Zhou J, Ward ES. Visualizing the site and dynamics of IgG salvage by the MHC class I-related receptor, FcRn. J Immunol. 2004; 172: 2021–2029. PMID: 14764666

14. Burmeister WP, Gastinel LN, Simister NE, Blum ML, Bjorkman PJ. Crystal structure at 2.2 A resolution of the MHC-related neonatal Fc receptor. Nature. 1994; 372: 336–343. https://doi.org/10.1038/372336a0 PMID: 7969491

15. Zijlstra M, Bix M, Simister NE, Loring JM, Raulet DH, Jaenisch R. β2-microglobulin deficient mice lack $CD4^{-}8^{+}$ cytolytic T cells. Nature. 1990; 344: 742–746. https://doi.org/10.1038/344742a0 PMID: 2139497

16. Israel EJ, Wilsker DF, Hayes KC, Schoenfeld D, Simister NE. Increased clearance of IgG in mice that lack β2-microglobulin: possible protective role of FcRn. Immunology. 1996; 89: 573–578. PMID: 9014824

17. Ghetie V, Hubbard JG, Kim JK, Tsen MF, Lee Y, Ward ES. Abnormally short serum half-lives of IgG in β2-microglobulin-deficient mice. Eur J Immunol. 1996; 26: 690–696. https://doi.org/10.1002/eji.1830260327 PMID: 8605939

18. Praetor A, Hunziker W. β2-microglobulin is important for cell surface expression and pH-dependent IgG binding of human FcRn. J Cell Sci. 2002; 115: 2389–2397. PMID: 12006623

19. Ghetie V, Popov S, Borvak J, Radu C, Matesoi D, Medesan C, et al. Increasing the serum persistence of an IgG fragment by random mutagenesis. Nat Biotechnol. 1997; 15: 637–640. https://doi.org/10.1038/nbt0797-637 PMID: 9219265

20. Wang Y, Tian Z, Thirumalai D, Zhang X. Neonatal Fc receptor (FcRn): a novel target for therapeutic antibodies and antibody engineering. J Drug Target. 2014; 22: 269–278. https://doi.org/10.3109/1061186X.2013.875030 PMID: 24404896

21. Le Panse R, Berrih-Aknin S. Autoimmune myasthenia gravis: autoantibody mechanisms and new developments on immune regulation. Curr Opin Neurol. 2013; 26: 569–576.

22. Feltkamp TE, van den Berg-Loonen PM, Nijenhuis LE, Engelfriet CP, van Rossum AL, van Loghem JJ, et al. Myasthenia gravis, autoantibodies, and HL-A antigens. Br Med J. 1974; 1: 131–133. PMID: 4544224

23. Israeli E, Agmon-Levin N, Blank M, Chapman J. Shoenfeld Y. Guillain-Barré syndrome—a classical autoimmune disease triggered by infection or vaccination. Clin Rev Allergy Immunol. 2012; 42: 121–130. https://doi.org/10.1007/s12016-010-8213-3 PMID: 20890797

24. Curtis AC, Heckaman JH, Wheeler AH. Study of the autoimmune reaction in dermatomyositis. JAMA. 1961; 178: 571–573. PMID: 13882763

25. Liu L, Garcia AM, Santoro H, Zhang Y, McDonnell K, Dumont J, et al. Amelioration of experimental autoimmune myasthenia gravis in rats by neonatal FcR blockade. J Immunol. 2007; 178: 5390–5398. PMID: 17404325

26. Li N, Zhao M, Hilario-Vargas J, Prisayanh P, Warren S, Diaz LA, et al. Complete FcRn dependence for intravenous Ig therapy in autoimmune skin blistering diseases. J Clin Invest. 2005; 115: 3440–3450. https://doi.org/10.1172/JCI24394 PMID: 16284651

27. Akilesh S, Petkova S, Sproule TJ, Shaffer DJ, Christianson GJ, Roopenian D. The MHC class I-like Fc receptor promotes humorally mediated autoimmune disease. J Clin Invest. 2004; 113: 1328–1333. https://doi.org/10.1172/JCI18838 PMID: 15124024

28. Kiessling P, Lledo-Garcia R, Watanabe S, Langdon G, Tran D, Bari M, et al. The FcRn inhibitor rozanolixizumab reduces human serum IgG concentration: A randomized phase 1 study. Sci Transl Med. 2017; 9: eaan1208.

29. McDonnell KA, Low SC, Hoehn T, Donnelly R, Palmieri H, Fraley C, et al. Synthesis and structure-activity relationships of dimeric peptide antagonists of the human immunoglobulin G-human neonatal Fc receptor (IgG-FcRn) interaction. J Med Chem. 2010; 53: 1587–1596. https://doi.org/10.1021/jm901128z PMID: 20092334

30. Mezo AR, Low SC, Hoehn T, Palmieri H. PEGylation enhances the therapeutic potential of peptide antagonists of the neonatal Fc receptor, FcRn. Bioorg Med Chem Lett. 2011; 21: 6332–6335. https://doi.org/10.1016/j.bmcl.2011.08.111 PMID: 21920737

31. Mezo AR, Sridhar V, Badger J, Sakorafas P, Nienaber V. X-ray crystal structures of monomeric and dimeric peptide inhibitors in complex with the human neonatal Fc receptor, FcRn. J Biol Chem. 2010; 285: 27694–27701. https://doi.org/10.1074/jbc.M110.120667 PMID: 20592032

32. Mezo AR, McDonnell KA, Hehir CAT, Low SC, Palombella VJ, Stattel JM, et al. Reduction of IgG in non-human primates by a peptide antagonist of the neonatal Fc receptor FcRn. Proc Natl Acad Sci USA. 2008; 105: 2337–2342. https://doi.org/10.1073/pnas.0708960105 PMID: 18272495

33. Mezo AR, McDonnell KA, Castro A, Fraley C. Structure-activity relationships of a peptide inhibitor of the human FcRn:human IgG interaction. Bioorg Med Chem. 2008; 16: 6394–6405. https://doi.org/10.1016/j.bmc.2008.05.004 PMID: 18501614

34. Wang Z, Fraley C, Mezo AR. Discovery and structure-activity relationships of small molecules that block the human immunoglobulin G-human neonatal Fc receptor (hIgG-hFcRn) protein-protein interaction. Bioorg Med Chem Lett. 2013; 23: 1253–1256. https://doi.org/10.1016/j.bmcl.2013.01.014 PMID: 23375228

35. Halgren TA. Identifying and characterizing binding sites and assessing druggability. J Chem Inf Model. 2009; 49: 377–389. https://doi.org/10.1021/ci800324m PMID: 19434839

36. Kozakov D, Grove LE, Hall DR, Bohnuud T, Mottarella SE, Luo L, et al. The FTMap family of web servers for determining and characterizing ligand-binding hot spots of proteins. Nat Protoc. 2015; 10: 733–755. https://doi.org/10.1038/nprot.2015.043 PMID: 25855957

37. Capra JA, Laskowski RA, Thornton JM, Singh M, Funkhouser TA. Predicting protein ligand binding sites by combining evolutionary sequence conservation and 3D structure. PLoS Comput Biol. 2009; 5: e1000585. https://doi.org/10.1371/journal.pcbi.1000585 PMID: 19997483

38. Zdobnov EM, Tegenfeldt F, Kuznetsov D, Waterhouse RM, Simão FA, Ioannidis P, et al. OrthoDB v9.1: cataloging evolutionary and functional annotations for animal, fungal, plant, archaeal, bacterial and viral orthologs. Nucleic Acids Res. 2017; 45: 744–749.

39. Sievers F, Wilm A, Dineen D, Gibson TJ, Karplus K, Li W, et al. Fast, scalable generation of high-quality protein multiple sequence alignments using Clustal Omega. Mol Syst Bio. 2011; 7: 1–6.

40. Kelm S, Shi J, Deane CM. MEDELLER: homology-based coordinate generation for membrane proteins. Bioinformatics. 2010; 26: 2833–2840. https://doi.org/10.1093/bioinformatics/btq554 PMID: 20926421

41. Delano WL. The PyMOL molecular graphics system, Version 2.0 Schrödinger, LLC.

42. Carr HY, Purcell EM. Effects of diffusion on free precession in nuclear magnetic resonance experiments. Phys Rev. 1954; 94: 630–638.

43. Meiboom S, Gill D. Modified spin-echo method for measuring nuclear relaxation times. Rev Sci Instrum. 1958; 29: 688–691.

44. Forsén S, Hoffman RA. Study of moderately rapid chemical exchange reactions by means of nuclear magnetic resonance. J Chem Phys. 1963; 39: 2892–2902.

45. Forsén S, Hoffman RA. Exchange rates by nuclear magnetic multiple resonance. III. Exchange reactions in systems with several nonequivalent sites. J Chem Phys. 1964; 40: 1189–1196.

46. Burmeister WP, Huber AH, Bjorkman PJ. Crystal structure of the complex of rat neonatal Fc receptor with Fc. Nature. 1994; 372: 379–383. https://doi.org/10.1038/372379a0 PMID: 7969498

47. Gardner KH, Kay LE. The use of ^{2}H, ^{13}C, ^{15}N multidimensional NMR to study the structure and dynamics of proteins. Annu Rev Biophys Biomol Struct. 1998; 27: 357–406. https://doi.org/10.1146/annurev.biophys.27.1.357 PMID: 9646872

48. Frueh DP. Practical aspects of NMR signal assignment in larger and challenging proteins. Prog Nucl Magn Reson Spectrosc. 2014; 78: 47–75. https://doi.org/10.1016/j.pnmrs.2013.12.001 PMID: 24534088

49. Pervushin K, Riek R, Wider G, Wüthrich K. Attenuated T2 relaxation by mutual cancellation of dipole-dipole coupling and chemical shift anisotropy indicates an avenue to NMR structures of very large biological macromolecules in solution. Proc Natl Acad Sci USA. 1997; 94: 12366–12371. PMID: 9356455

50. Gastinel LN, Simister NE, Bjorkman PJ. Expression and crystallization of a soluble and functional form of an Fc receptor related to class I histocompatibility molecules. Proc Natl Acad Sci USA. 1992; 89: 638–642. PMID: 1530991

51. Zhou DH, Shah G, Cormos M, Mullen C, Sandoz D, Rienstra CM. Proton-detected solid-state NMR spectroscopy of fully protonated proteins at 40 kHz magic-angle spinning. J Am Chem Soc. 2007; 129: 11791–11801. https://doi.org/10.1021/ja073462m PMID: 17725352

52. Linser R, Fink U, Reif B. Proton-detected scalar coupling based assignment strategies in MAS solid-state NMR spectroscopy applied to perdeuterated proteins. J Magn Reson. 2008; 193: 89–93. https://doi.org/10.1016/j.jmr.2008.04.021 PMID: 18462963

53. Zhou DH, Nieuwkoop AJ, Berthold DA, Comellas G, Sperling LJ, Tang M, et al. Solid-state NMR analysis of membrane proteins and protein aggregates by proton detected spectroscopy. J Biomol NMR. 2012; 54: 291–305. https://doi.org/10.1007/s10858-012-9672-z PMID: 22986689

54. Barbet-Massin E, Pell AJ, Retel JS, Andreas LB, Jaudzems K, Franks WT, et al. Rapid proton-detected NMR assignment for proteins with fast magic angle spinning. J Am Chem Soc. 2014; 136: 12489–12497. https://doi.org/10.1021/ja507382j PMID: 25102442

55. Lalli D, Idso MN, Andreas LB, Hussain S, Baxter N, et al. Proton-based structural analysis of a heptahelical transmembrane protein in lipid bilayers. J Am Chem Soc. 2017; 139: 13006–13012. https://doi.org/10.1021/jacs.7b05269 PMID: 28724288

56. Struppe J, Quinn CM, Lu M, Wang M, Hou G, Lu X, et al. Expanding the horizons for structural analysis of fully protonated protein assemblies by NMR spectroscopy at MAS frequencies above 100 kHz. Solid State Nucl Magn Reson. 2017; 87: 117–125. https://doi.org/10.1016/j.ssnmr.2017.07.001 PMID: 28732673

57. Stanek J, Andreas LB, Jaudzems K, Cala D, Lalli D, Bertarello A, et al. NMR spectroscopic assignment of backbone and side-chain protons in fully protonated proteins: microcrystals, sedimented assemblies, and amyloid fibrils. Angew Chem Int Ed. 2016; 55: 15504–15509.

58. Böckmann A, Gardiennet C, Verel R, Hunkeler A, Loquet A, Pintacuda G, et al. Characterization of different water pools in solid-state NMR protein samples. J Biomol NMR. 2009; 45: 319–327. https://doi.org/10.1007/s10858-009-9374-3 PMID: 19779834

59. Gardiennet C, Schütz AK, Hunkeler A, Kunert B, Terradot L, Böckmann A, et al. A sedimented sample of a 59 kDa dodecameric helicase yields high-resolution solid-state NMR spectra. Angew Chem Int Ed. 2012; 51: 7855–7858.

60. Andreas LB, Jaudzems K, Stanek J, Lalli D, Bertarello A, Le Marchand T, et al. Structure of fully protonated proteins by proton-detected magic-angle spinning NMR. Proc Natl Acad Sci USA. 2016; 113: 9187–9192. https://doi.org/10.1073/pnas.1602248113 PMID: 27489348

61. Penzel S, Smith AA, Agarwal V, Hunkeler A, Org ML, Samoson A, et al. Protein resonance assignment at MAS frequencies approaching 100 kHz: a quantitative comparison of J-coupling and dipolar-coupling-based transfer methods. J Biomol NMR. 2015; 63: 165–186. https://doi.org/10.1007/s10858-015-9975-y PMID: 26267840

62. Agarwal V, Penzel S, Szekely K, Cadalbert R, Testori E, Oss A, et al. De novo 3D structure determination from sub-milligram protein samples by solid-state 100 kHz MAS NMR spectroscopy. Angew Chem Int Ed. 2014; 53: 12253–12256.

63. Beerbaum M, Ballaschk M, Erdmann N, Schnick C, Diehl A, Uchanska-Ziegler B, et al. NMR spectroscopy reveals unexpected structural variation at the protein–protein interface in MHC class I molecules. J Biomol NMR. 2013; 57: 167–178. https://doi.org/10.1007/s10858-013-9777-z PMID: 24006098

64. Smith AA, Ravotti F, Testori E, Cadalbert R, Ernst M, Böckmann A, et al. Partially-deuterated samples of HET-s (218–289) fibrils: assignment and deuterium isotope effect. J Biomol NMR. 2017; 67: 109–119. https://doi.org/10.1007/s10858-016-0087-0 PMID: 28074361

65. Lorimer D, Raymond A, Walchli J, Mixon M, Barrow A, Wallace E, et al. Gene Composer: database software for protein construct design, codon engineering, and gene synthesis. BMC Biotechnol. 2009; 9: 36–58. https://doi.org/10.1186/1472-6750-9-36 PMID: 19383142

66. Wasilko DJ, Lee SE, Stutzman-Engwall KJ, Reitz BA, Emmons TL, Mathis KJ, et al. The titerless infected-cells preservation and scale-up (TIPS) method for large-scale production of NO-sensitive human soluble guanylate cyclase (sGC) from insect cells infected with recombinant baculovirus. Protein Expr Purif. 2009; 65: 122–132. https://doi.org/10.1016/j.pep.2009.01.002 PMID: 19174191

67. Newman J, Egan D, Walter TS, Meged R, Berry I, Ben Jelloul M, et al. Towards rationalization of crystallization screening for small- to medium-sized academic laboratories: the PACT/JCSG+ strategy. Acta Cryst Section D. 2005; 61: 1426–1431.

68. Kabsch W. XDS. Acta Cryst Section D. 2010; 66: 125–132.

69. Adams PD, Afonine PV, Bunkoczi G, Chen VB, Davis IW, Echols N, et al. PHENIX: a comprehensive Python-based system for macromolecular structure solution. Acta Cryst Section D. 2010; 66: 213–221.

70. Emsley P, Lohkamp B, Scott WG, Cowtan K. Features and development of Coot. Acta Cryst Section D. 2010; 66: 486–501.

71. Chen VB, Arendall WB, Headd JJ, Keedy DA, Immormino RM, Kapral GJ, et al. MolProbity: all-atom structure validation for macromolecular crystallography. Acta Cryst Section D. 2010; 66: 12–21.

72. Berman H, Henrick K, Nakamura H. Announcing the worldwide protein data bank. Nat Struct Biol. 2003; 10: 980. https://doi.org/10.1038/nsb1203-980 PMID: 14634627

73. Berman HM, Westbrook J, Feng Z, Gilliland G, Bhat TN, Weissig H, et al. The protein data bank. Nucleic Acids Res. 2000; 28: 235–242. PMID: 10592235

74. Van Der Spoel D, Lindahl E, Hess B, Groenhof G, Mark AE, Berendsen HJC. GROMACS: fast, flexible, and free. J Comput Chem. 2005; 26: 1701–1718. https://doi.org/10.1002/jcc.20291 PMID: 16211538

75. Pines A, Gibby MG, Waugh JS. Proton-enhanced nuclear induction spectroscopy: a method for high resolution NMR of dilute spins in solids. J Chem Phys. 1972; 56: 1776–1777.

76. Verel R, Ernst M, Meier BH. Adiabatic dipolar recoupling in solid-state NMR: the DREAM scheme. J Magn Reson. 2001; 150: 81–99. https://doi.org/10.1006/jmre.2001.2310 PMID: 11330986

77. Stevens TJ, Fogh RH, Boucher W, Higman VA, Eisenmenger F, Bardiaux B, et al. A software framework for analysing solid-state MAS NMR data. J Biomol NMR. 2011; 51: 437–447. https://doi.org/10.1007/s10858-011-9569-2 PMID: 21953355

78. Schuck P. Size-distribution analysis of macromolecules by sedimentation velocity ultracentrifugation and Lamm equation modeling. Biophysj. 2000; 78: 1606–1619.

5

TEMPERATURE DEPENDENCE OF CROSS-EFFECT DYNAMIC NUCLEAR POLARIZATION IN ROTATING SOLIDS: ADVANTAGES OF ELEVATED TEMPERATURES

5.1 Synopsis

As introduced in chapter 1, DNP is a powerful method to increase the inherently low sensitivity in NMR spectroscopy. In protonation dynamics studies, the structural properties of protein sites with low experimental accessibility are of particular interest, e.g. the structural features of chromophores in photosensitive proteins. In the current and following chapters, DNP is further developed to facilitate protonation dynamics investigations, and it is subsequently applied in such studies.

The DNP effect, i.e. the NMR signal enhancement, is most efficient at low temperature. In practice, usually sample temperatures around 100 K are used to perform DNP-enhanced solid-state MAS NMR experiments. However, spectral resolution is then significantly reduced as described in chapter 1. Therefore, it is desirable to improve the efficacy of biradicals and thereby the DNP performance at higher temperatures. For studies of protonation dynamics, it is especially important to make efficient DNP measurements at high temperatures possible. At low temperatures, motional processes are decelerated and therefore interpretation of protonation dynamics events might be hampered. In the current chapter, different TOTAPOL isotopologues with varying degree of methyl group deuteration are used to improve the DNP performance at a temperature towards 190 – 200 K. The electron spin relaxation properties, enhancement factors and longitudinal ^{1}H relaxation times of four different TOTAPOL versions and the gold-standard biradical AMUPol are systematically characterized using proline and the SH3 domain as standard samples. As we show, the loss of enhancement at higher temperatures can be partially compensated by faster repetition rates of the NMR experiment resulting in a 15-fold advantage of DNP-enhanced over conventional MAS NMR measurements at 200 K. This is a very promising result in the context of protonation dynamics studies, making DNP suitable in the temperature range of 100 – 200 K, depending on the system investigated. Another improvement is a gain in spectral resolution. At 200 K, reasonable linewidths for the SH3 sample are observed making three-dimensional experiments such as (H)NCACX and (H)NCOCX feasible. This shows the potential for performing resonance assignments using DNP-enhanced MAS NMR. It may facilitate site-specific investigations of samples with low accessibility in future studies of protonation dynamics. In addition, it allows solid-state MAS NMR protonation dynamics investigations at temperatures up to 200 K with increased S/N.

5.2 Personal contribution

In this study, I was involved in preparation of proline and SH3 samples for DNP experiments, I recorded NMR spectra, analyzed NMR data and was involved in writing of the paper. I did not perform protein expression and purification, and organic synthesis.

Michel-Andreas Geiger, Marcella Orwick-Rydmark, Katharina Märker, Edgar Specker, Marc Nazaré, Barth-Jan van Rossum, Fabien Aussenac, Thomas Prisner and Hartmut Oschkinat designed the study; Michel-Andreas Geiger, Marcella Orwick-Rydmark, Katharina Märker, W. Trent Franks, Dmitry Akhmetzyanov, Daniel Stöppler, Maximilian Zinke, Anne Diehl and Ümit Akbey performed research; Michel-Andreas Geiger, Marcella Orwick-Rydmark, Katharina Märker, W. Trent Franks, Dmitry Akhmetzyanov, Daniel Stöppler, Barth-Jan van Rossum, Thomas Prisner and Hartmut Oschkinat analyzed data; Michel-Andreas Geiger, Marcella Orwick-Rydmark, Katharina Märker, Barth-Jan van Rossum and Hartmut Oschkinat wrote the paper with contributions from W. Trent Franks, Dmitry Akhmetzyanov, Daniel Stöppler, Thomas Prisner and Ümit Akbey.

5.3 Original Publication and Supplementary Information

Reproduced from (with permission from the PCCP Owner Societies):

Michel-Andreas Geiger,[#] Marcella Orwick-Rydmark,[#] Katharina Märker, W. Trent Franks, Dmitry Akhmetzyanov, **Daniel Stöppler**, Maximilian Zinke, Edgar Specker, Marc Nazaré, Anne Diehl, Barth-Jan van Rossum, Fabien Aussenac, Thomas Prisner, Ümit Akbey, and Hartmut Oschkinat:
'Temperature dependence of cross-effect dynamic nuclear polarization in rotating solids: advantages of elevated temperatures', *Physical Chemistry Chemical Physics*, 2016, 18, pp 30696–30704
[#] ***Equal contribution***

The article and all additional supplementary files are available at https://doi.org/10.1039/C6CP06154K

6

LIGHT–DARK ADAPTATION OF CHANNELRHODOPSIN INVOLVES PHOTOCONVERSION BETWEEN THE ALL-TRANS AND 13-CIS RETINAL ISOMERS

6.1 Synopsis

Even though DNP-enhanced MAS NMR experiments usually have limited spectral resolution at temperatures around 100 K, some structure-related questions in the context of protonation dynamics can be addressed under such conditions. In the current chapter, the application of DNP to the channelrhodopsin (ChR) chimera C1C2 is presented. ChRs are light-gated unselective cation channels for H^+, Na^+, K^+ and Ca^{2+}. They are used as model proteins to study protonation dynamics, and they are employed in optogenetics to control neuronal cells with light. To engineer existing ChRs towards optimized application in neurobiology, it is desirable to understand the molecular mechanism. We addressed the determination of the retinal configuration during the ChR photocycle as it is an important structural feature to enable the cation conducting function.

In order to investigate the retinal configuration in dark-adapted ChR, we employed NMR spectroscopy. Using a specifically ^{13}C-labeled retinal (^{13}C–[12,15,20]), magnetization transfers based on dipolar couplings reporting on distances could be used to identify the retinal configuration. As we show, it was crucial to apply DNP to this problem as only insufficient S/N could be obtained for observation of the expected cross peaks with conventional solid-state MAS NMR. Our DNP-enhanced solid-state MAS NMR spectra unequivocally prove that retinal consists solely of the all-*trans* isomer in the initial-dark adapted state of ChR. This result served as the basis to propose a new two-state photocycle in conjunction with Resonance Raman and UV-vis spectroscopy measurements. In the context of protonation dynamics, this study is an important step towards deciphering the structural dynamics of the ChR chromophore during H^+ channeling and conductance of other cations.

Methodologically, it was interesting to see that already the conventional TOTAPOL, i.e. the non-deuterated version, gives rise to a 10-fold enhancement of the ^{13}C-labeled retinal reconstituted in the membrane-embedded C1C2 at 100 K. Compared to room temperature measurements, the DNP experiment certainly profits from increased S/N according to Boltzmann and from deceleration of motional conformational processes in the protein. The latter leads to reduced mobility of dynamic parts and thereby increases the efficiency of magnetization transfers based on dipolar couplings such as CP or DARR mixing. Therefore, the enhanced S/N in this case is not only attributed to the exploitation of high electron polarization through DNP, but also through the low

temperatures applied. A second aspect worth of mentioning is that this investigation profits from the selective labeling. It leads to fully resolved signals, especially by utilizing the large ^{13}C spectral width and the high dispersion of the aromatic-^{13}C and methyl-^{13}C resonances in retinal. Using such specific labeling patterns is a powerful approach in DNP-enhanced solid-state MAS NMR studies as it circumvents the unfavorably broadened lines and allows the observation of fully resolved signals.

6.2 Personal contribution

I prepared C1C2 samples for DNP-enhanced MAS NMR and solution-state NMR measurements, recorded NMR experiments, analyzed data and was involved in writing the paper. C1C2 was expressed and purified by Anne Diehl and Katja Stehfest.

Dirk Trauner, Peter Hegemann, Hartmut Oschkinat, Peter Hildebrandt and Katja Stehfest designed the study; Sara Bruun, Daniel Stöppler, Anke Keidel, Uwe Kuhlmann, Meike Luck, Anne Diehl, Michel-Andreas Geiger, David Woodmansee and Katja Stehfest performed research; Sara Bruun, Daniel Stöppler, Dirk Trauner, Peter Hegemann, Hartmut Oschkinat, Peter Hildebrandt and Katja Stehfest analyzed data; Sara Bruun, Daniel Stöppler, Peter Hegemann, Hartmut Oschkinat, Peter Hildebrandt and Katja Stehfest wrote the paper.

6.3 Original Publication and Supplementary Information

Sara Bruun,[#] **Daniel Stoeppler**,[#] Anke Keidel, Uwe Kuhlmann, Meike Luck, Anne Diehl, Michel-Andreas Geiger, David Woodmansee, Dirk Trauner, Peter Hegemann, Hartmut Oschkinat, Peter Hildebrandt, and Katja Stehfest:
'Light−Dark Adaptation of Channelrhodopsin Involves Photoconversion between the all-*trans* and 13-*cis* Retinal Isomers', *Biochemistry*, 2015, 54 (35), pp 5389–5400
[#]***Equal contribution***

The article and all additional supplementary files are available at https://doi.org/10.1021/acs.biochem.5b00597

7

bcTol: A Highly Water-Soluble Biradical for Efficient Dynamic Nuclear Polarization of Biomolecules

7.1 Synopsis

Chapters 5 and 6 showed the great potential of DNP experiments at higher temperature and in the context of protonation dynamics studies, respectively. The efficiency of this method, however, needs to be further improved to make investigations of a variety of proteins feasible. In cross-effect DNP, the high polarization of unpaired electrons in stable biradicals is exploited to enhance the NMR signals of nuclei of interest. Since such biradicals are usually of rather hydrophobic character and biomolecules require an aqueous environment, it is desirable to design biradicals with high water-solubility. In addition, this would lead to a more equal distribution of the biradical in the sample and to minimized potential non-covalent interactions between the biradical and the protein, thereby reducing PRE-effects. Water-soluble biradicals would also facilitate DNP-enhanced NMR studies of soluble proteins, which can be accomplished under solid-state MAS conditions since the sample is frozen.

For these reasons, the optimized highly water-soluble biradical bcTol is introduced in the current chapter. It helps to further improve the DNP measurement conditions towards studies of protonation dynamics and structural biology in general. Using proline and SH3 as standard samples, the DNP performance of bcTol is characterized comprehensively. It shows high enhancement factors of approximately 240 at 110 K and still 40 at around 180 K for the SH3 sample. It is also tested for the C1C2 sample embedded in lipid vesicles, yielding an enhancement of 36 corresponding to a 4-fold improvement over TOTAPOL (see chapter 6).

In summary, the presented new biradical bcTol has the great potential for improved DNP measurements of biological macromolecules. This provides an important basis to further apply DNP in protonation dynamics studies as it allows investigations under MAS conditions without size limitation of the protein; especially its applicability to soluble, large proteins is of high interest.

7.2 Personal contribution

In this study, I prepared proline, SH3 and C1C2 samples for DNP measurements, recorded NMR experiments, analyzed NMR data and was involved in writing the paper. I did not perform protein expression and purification and organic synthesis.

Anil P. Jagtap, Michel-Andreas Geiger, Daniel Stöppler, Hartmut Oschkinat and Snorri Th. Sigurdsson designed the study; Anil P. Jagtap, Michel-Andreas Geiger and Daniel Stöppler performed research; Anil P. Jagtap, Michel-Andreas Geiger, Daniel Stöppler, Hartmut Oschkinat and Snorri Th. Sigurdsson analyzed data; Michel-Andreas Geiger, Daniel Stöppler, Hartmut Oschkinat and Snorri Th. Sigurdsson wrote the paper with contributions from Anil P. Jagtap and Marcella Orwick-Rydmark.

7.3 Original Publication and Supplementary Information

Reproduced from (with permission from The Royal Society of Chemistry):

Anil P. Jagtap, Michel-Andreas Geiger, **Daniel Stöppler**, Marcella Orwick-Rydmark, Hartmut Oschkinat, and Snorri Th. Sigurdsson:
'bcTol: a highly water-soluble biradical for efficient dynamic nuclear polarization of biomolecules', *Chemical Communications*, 2016, 52, pp 7020–7023

The article and all additional supplementary files are available at https://doi.org/10.1039/C6CC01813K

8

DYNAMIC NUCLEAR POLARIZATION PROVIDES NEW INSIGHTS INTO CHROMOPHORE STRUCTURE IN PHYTOCHROME PHOTORECEPTORS

8.1 Synopsis

In the previous chapter, the new highly water-soluble biradical bcTol was introduced. Based on the results of chapters 5 and 6, it became clear that further optimization of biradicals and the DNP performance is required to study various aspects of protonation dynamics. In the current chapter, the promising performance of bcTol in biological DNP-enhanced solid-state MAS NMR is utilized in a protonation dynamics investigation of the phytochrome photoreceptor Cph1.

We use the functional photosensory module of Cph1 (Cph1Δ2, 58 kDa), which serves as a model protein in phytochrome research. Phytochromes are red/far-red photochromic photoreceptors and act as master regulators in development of plants and cyanobacteria, thereby controlling transcription of about 20% of all genes. It has been shown that the chromophore changes its protonation state during the phytochrome photocycle. This change and the high biological relevance of phytochromes makes them excellent model systems to investigate the molecular mechanisms of protonation dynamics in detail. One important biophysical question is the localization of the positive charge in the phycocyanobilin chromophore of Cph1 as it may influence the structural events connected to protonation state changes in the Pr → Pfr and Pfr → Pr photointermediate-transitions. Herein, we employ DNP-enhanced MAS NMR to analyze the charge localization for the first time experimentally. In general, chemical shifts can be used as probes to localize charges. In the present case, the chromophore ^{15}N chemical shifts may be utilized for such analysis. Previous investigations using solution-state and conventional solid-state MAS NMR have not revealed an unambiguous assignment of the four ^{15}N chemical shifts. As we show in this study, the sensitivity enhancement through DNP was crucial to record a two-dimensional ^{15}N–^{13}C–^{13}C correlation spectrum, employing DARR mixing between the carbon spins. Using this experiment, the ^{15}N chemical shifts could now be assigned unequivocally. This enabled us to conclude on the localization of the positive charge. In addition, we could detect the proximities of water molecules in the chromophore binding pocket. This helps to further investigate potential proton exchange pathways and the hydrogen bonding network by NMR.

As described above, the application of bcTol in this study was instrumental. Cph1Δ2 is a soluble protein and it was therefore required to use this highly water-soluble

biradical. We could obtain a reasonable enhancement of around 40 at 100 K, making the acquisition of the insensitive (H)NCC experiment possible.

8.2 Personal contribution

I prepared the Cph1Δ2 sample for the DNP experiments, recorded all NMR spectra, analyzed the data and was involved in writing the paper. The protein was expressed and purified by Christina Lang.

Daniel Stöppler, Chen Song, Snorri Th. Sigurdsson, Jörg Matysik, Jon Hughes and Hartmut Oschkinat designed the study; Daniel Stöppler, Barth-Jan van Rossum, Michel-Andreas Geiger, Christina Lang, Maria-Andrea Mroginski and Anil P. Jagtap performed research; Daniel Stöppler, Chen Song, Barth-Jan van Rossum, Maria-Andrea Mroginski, Jörg Matysik, Jon Hughes and Hartmut Oschkinat analyzed data; Daniel Stöppler, Jon Hughes and Hartmut Oschkinat wrote the paper with contributions from Chen Song, Maria-Andrea Mroginski and Jörg Matysik.

8.3 Original Publication and Supplementary Information

Daniel Stöppler, Chen Song, Barth-Jan van Rossum, Michel-Andreas Geiger, Christina Lang, Maria-Andrea Mroginski, Anil P. Jagtap, Snorri Th. Sigurdsson, Jörg Matysik, Jon Hughes, and Hartmut Oschkinat:
'Dynamic Nuclear Polarization Provides New Insights into Chromophore Structure in Phytochrome Photoreceptors', *Angewandte Chemie International Edition*, 2016, 55 (52), pp 16017–16020

The article and all additional supplementary files are available at https://doi.org/10.1002/anie.201608119

9

GENERAL DISCUSSION AND CONCLUSION

This work is intended to apply advanced MAS NMR as a structural biology approach to study protonation dynamics in complex proteins; the two methods employed are proton detection combined with fast MAS and DNP-enhanced MAS NMR. After introducing protonation dynamics and the NMR methods in the first chapter, some of the presented projects deal with development of the methods applied (chapters 2, 5 and 7). In these studies, mainly standard samples such as proline and the SH3 domain were used. In the remainder chapters, structure-related questions in the context of protonation dynamics were investigated in different proteins: in the light-driven proton pump bacteriorhodopsin in its native membrane (chapter 3), in the soluble extra-cellular domain of the neonatal Fc receptor (chapter 4), in the membrane-embedded channelrhodopsin C1C2 (chapter 6) and in the soluble phytochrome photoreceptor Cph1 (chapter 8). The results of each chapter are discussed therein, and only a few remarks are given now on the obtained results in this 'General Discussion and Conclusion' chapter. In addition, possible future perspectives are briefly discussed.

9.1 Discussion and Conclusion

In comparison to other structural biology methods and spectroscopies, a general advantage of NMR is the possibility to detect protons directly. Hence, it provides spatial information on structure-related questions in protonation dynamics, and it can be also applied to obtain kinetic data on proton relocation processes. To make use of proton detection not only for spectroscopic reasons, i.e. increase in sensitivity compared to ^{13}C- and ^{15}N-detection and improvement in spectral resolution through introducing an additional dimension, we propose a proton-detected solid-state MAS NMR experiment in chapter 2. It allows the observation of hydrogen bonds as shown for the SH3 model protein. In the future, the experiment may be applied to investigate hydrogen bonds in different conformational states of proteins, thereby enabling the detailed characterization of protonation dynamics features.

To test proton detection in solid-state MAS NMR as a method to investigate protonation dynamics, we performed a pilot study on the light-driven proton pump bacteriorhodopsin, presented in chapter 3. We used ^{2}H,^{13}C,^{15}N-labeled native purple membrane of BR and reintroduced protons at exchangeable sites during illumination.

The idea is that under these conditions functional amino acid side chains are reprotonated and the respective protons can be detected. As we show, in addition to such side chains also some amides in the protein backbone can exchange as long as they are solvent-accessible. This has been seen also in other proton-detected solid-state MAS NMR investigations on membrane proteins (180, 208, 209). More interestingly, signals could be observed for delocalized protons at the carboxylic moieties of D85 and D96 and at the guanidinium group of R82. These protons show chemical exchange with H_2O as measured by ^1H–^1H exchange spectroscopy at 40 kHz MAS. The observed proton exchange processes are highly relevant for the functional role of the amino acids under investigation, especially in the case of R82 and D85. Our findings suggest that R82 is involved in the proton transport pathway and a proton is shifting within a hydrogen bond between the D85 carboxyl group and water. The NMR results have been corroborated by *ab initio* simulations in collaboration with the group of Roland R. Netz (Free University of Berlin). This study introduces proton-detected solid-state MAS NMR as a powerful tool to investigate protonation dynamics in proteins, and it may be applied to other proteins to help establishing protonation dynamics as a fundamental principle in protein function.

As described in the introduction (chapter 1), it is important to extend the spectrum of protein classes under investigation to further accumulate evidence for the importance of protonation dynamics. Therefore, we selected a disease-relevant protein-protein interaction that is based on interactions between protonatable amino acid side chains and aimed to modulate this interaction with a small molecule inhibitor. The neonatal Fc receptor (FcRn) is a clinically validated drug target in autoimmune diseases; it regulates protein homeostasis of IgG and serum albumin. In chapter 4, we develop a small molecule that binds to the extra-cellular domain of this receptor ($FcRn_{ECD}$) with low μM affinity in an evolutionarily conserved cavity. We characterized the interaction by x-ray crystallography; however, no structural changes could be observed in the crystal structures with and without ligand. Therefore, we approached the observation of potential structural alterations by NMR spectroscopy. Unfortunately, the soluble $FcRn_{ECD}$ could not be produced in deuterated form. For this reason and due to its size of 42 kDa, triple-resonance experiments in solution-state NMR involving $^{13}C\beta$ and $^{13}C\alpha$ are not possible with sufficient S/N. To resolve this issue, we present an innovative strategy employing sedimentation of the soluble protein directly into a

0.7 mm MAS rotor followed by proton-detected triple-resonance MAS NMR at 100 kHz on the fully protonated ^{13}C,^{15}N-labeled receptor. The obtained spectral quality is remarkably high, and it allowed us to observe chemical shift perturbations reporting on structural changes in the small molecule binding site and in protein regions distant to it. These observations indicate allosteric effects that can be achieved by ligand binding. However, no structural changes in the IgG binding site could be found; thus, an interference with the protein-protein interaction based on protonation dynamics with the identified compound is unlikely. In addition, some of the detected changes in the albumin binding area coincidence with a potential interface of $FcRn_{ECD}$ diprotomers formed under the experimental conditions, and thus cannot be reliably interpreted. Still, the 100 kHz MAS NMR experiments suggest that an allosteric modulation of FcRn could be achieved by using an optimized ligand. This investigation establishes a size-independent NMR approach to study fully protonated soluble proteins that can be produced in any expression host. It therefore may serve as the basis for future investigations, in protonation dynamics studies and beyond.

In chapter 5, it is shown that increasing the measurement temperature in DNP-enhanced solid-state MAS NMR studies can improve the spectral resolution to some degree. It was elaborated using the model protein SH3 and the amino acid proline. As an important result, we find that the sensitivity at 200 K is higher by a factor of 15 with DNP enhancement compared to solid-state MAS NMR without DNP at this temperature. However, the obtained S/N with DNP at 200 K should be compared to an optimized experiment without biradical in a conventional solid-state 3.2 mm MAS NMR probe at room temperature. Such a comparison would allow estimation of the increase in sensitivity using DNP in structural biology studies, especially when recording multidimensional experiments which are anticipated to be affected by differences in T_2. Still, the achieved improvement in DNP enhancement may facilitate NMR studies of protonation dynamics in the future, because it makes a temperature range between 100 K and 200 K accessible for NMR measurements with increased sensitivity. It allows to elucidate the dynamic behavior of proteins as a function of temperature without limitations in molecular weight and physical state of the protein under investigation. Moreover, only small protein amounts are required, profiting from the gain in sensitivity. It may be envisaged that questions like proton transfer relocation processes are now experimentally accessible in a variety of proteins,

especially in cases when the underlying exchange mechanism is too fast for NMR detection at room temperature.

Using DNP, some structural features in proteins related to protonation dynamics can be also investigated at 100 K; in chapter 6, such an application is presented. It was still under debate which configuration the retinal chromophore adopts in the dark-adapted state of the channelrhodopsin photocycle. As seen in other rhodopsins, a mixture of the all-*trans* and 13-*cis* isomers was conceivable, and initial experiments using FTIR, UV-vis and RR spectroscopy, and chemical extraction followed by HPLC analysis suggested a 70%:30% distribution (210-212). We addressed this issue by applying DNP-enhanced solid-state MAS NMR to the membrane-embedded channelrhodopsin chimera C1C2, reconstituted with isotopically enriched retinal, selectively ^{13}C-labeled in the carbon positions 12, 15 and 20. We employed the DARR mixing scheme, making use of through space magnetization transfers based on dipolar couplings between these three ^{13}C spins. This allowed us to unequivocally prove that only the all-*trans* isomer exists in the initial dark-adapted state of ChR. As an important result, it helps to establish the sequence of conformational changes in the photocycle required for proton conductance through the pore of the protein. This finding was also shown independently by the group of Clemens Glaubitz, in a similar DNP-enhanced solid-state MAS NMR investigation (76). Under the experimental conditions of DNP, however, motional processes are decelerated and the protein is somewhat rigidified, making magnetization transfers based on dipolar couplings more efficient. Therefore, the obtained results have to be attributed to some degree to an improvement in CP and DARR mixing efficiency due to lower temperature, and not only to the DNP-effect. In addition, the sensitivity at 100 K is improved by a factor of ~3 compared to room temperature, due to the temperature-dependent Boltzmann distribution.

To further optimize the DNP efficiency in biological solid-state MAS NMR, we introduced the new biradical bcTol. A detailed characterization is presented in chapter 7, highlighting its remarkable performance when investigating the proline and SH3 standard samples. bcTol is highly water-soluble and therefore easy-to-handle in structural biology studies. In addition, it features reduced PRE-effects in proteins due to an optimized distribution throughout the aqueous sample. This leads to a somewhat improved spectral resolution compared to the standard biradical AMUPol.

In chapter 8, the great potential of bcTol is exploited in an application of DNP-enhanced solid-state MAS NMR to the phytochrome photoreceptor Cph1. We used the photosensory module Cph1Δ2 to investigate the structure of the phycocyanobilin chromophore, which was ^{13}C,^{15}N-labeled, whereas the protein remained unlabeled. This allowed us to unambiguously assign the chromophore ^{15}N chemical shifts, which is helpful in the context of protonation dynamics studies. Using these chemical shifts, we can conclude on the protonation states at these sites. This is important since they change in the Pr → Pfr transition. In addition, the proximities of water molecules to the chromophore can be estimated based on DNP-enhanced ^{15}N-detected, Lee-Goldburg decoupled ^{1}H-^{15}N correlation spectra. This may help in analysis of potential proton exchange pathways during the photocycle of phytochrome photoreceptors. Furthermore, the ^{15}N chemical shifts are used as probes for charge localization. In phycocyanobilin, the localization of the positive charge could not be shown experimentally so far. The obtained chemical shifts indicate a charge localization mainly at the rings B and C in the Pr state. Since it has been shown that N24 deprotonates during the photocycle and the positive charge is subsequently localized at ring D in the Pfr form, the positive charge must move during the transition between the photointermediates.

In summary, both proton detection and DNP could be used to investigate protonation dynamics in various proteins in this thesis. Applications on two membrane-embedded proteins, channelrhodopsin and bacteriorhodopsin, and two large soluble proteins, phytochrome and $FcRn_{ECD}$, could be successfully performed. It became also clear that a combination with other techniques helps to gain detailed insight into the addressed questions. For example, resonance Raman spectroscopy facilitated the study of C1C2 photointermediates in chapter 6. Similarly, *ab initio* simulations on proton delocalization and exchange processes helped to corroborate the observed NMR signals in chapter 3. The most successful methodological combination is shown in chapter 4. X-ray crystallography, computational methods, NMR-based fragment screening, solution-state NMR, proton-detected NMR at 100 kHz MAS and other biophysical tools were used to develop a small molecule and to characterize its potential as an allosteric inhibitor of the FcRn–IgG and FcRn–albumin interactions. Such combination with other methods to study protonation dynamics should be further

strengthened as it allows more reliable conclusions on the molecular mechanisms under investigation.

9.2 Future Perspectives

Based on the presented approach to study protonation dynamics by both proton-detected and DNP-enhanced solid-state MAS NMR, further investigations can now be pursued.

The experiment presented in chapter 2, for example, should be tested further on an α-helical protein, to demonstrate the possibility to detect characteristic α-helical hydrogen bond patterns. In addition, the experiment could be applied to other proteins, for example to the phytochrome photoreceptor Cph1. In a modified form, e.g. as an (H)N(H)COH experiment, it could be useful in a detailed elucidation of hydrogen bonds in the chromophore binding pocket of Cph1. A number of such interactions is of great interest, for example between arginine side chains, e.g. R222 and R254, and the carboxylic groups of the phycocyanobilin propionic moieties (44, 65, 213). It could be also applied to detect potential hydrogen bond changes between R472 and the D297 carboxyl group during the Pr → Pfr transition (214). For such a scientific venture, *in situ* light irradiation in a fast MAS probe offering a wide range of experimental temperatures is required. With additional resources now available in the second funding period of the CRC1078, such a probe was co-financed and purchased. As a DNP probe, it can be used in a temperature range between 100 K and 295 K with *in situ* light irradiation during the experiments, and at MAS frequencies up to 40 kHz with 1.9 mm MAS rotors, making the above-mentioned studies possible.

To provide further insight into the mechanism of molecular action of phytochromes, the protonation state changes in phycocyanobilin and amino acid side chains during photoconversion should be investigated. Based on chapter 8, chemical shift information on phycocyanobilin are now available, providing the possibility of studying the flip of ring D and the changes of its interactions with the protein and local water molecules (65, 215). In general, the binding pocket residues including H290, H260, Y176 and Y203 of Cph1 need to be studied further to complete the

understanding of chromophore function (214, 216). As a main goal, detected changes in the chromophore and its surrounding residues should be linked to the secondary structure rearrangement in the tongue-region from β-sheet (Pr state) to α-helix (Pfr state) proposed by x-ray crystallography (45, 81, 217, 218). In addition, the order of events during photoconversion may be subject to follow-up studies. These events include light absorption, chromophore isomerization, charge movement, protonation state changes, conformational changes of amino acid side chains and secondary structure rearrangement (46, 65, 68, 71, 202, 217, 219-223). Another aim could be to test the idea of PHY domain movement in phytochromes upon Pr → Pfr transition, which has been suggested by small angle x-ray scattering measurements (SAXS) (45). This could be addressed by using cryo-EM or EPR, or a combination of the two.

With the new probe available, proton-detected solid-state MAS NMR experiments can be performed in a large range of temperatures. This facilitates observation of proton exchange processes by varying the temperature, thereby modulating the corresponding kinetic exchange rate. Such an experiment needs to be performed in the studies on bacteriorhodopsin. Recently, the retinal Schiff base proton could be observed for the first time (224). However, this was only possible at 100 K, whereby this proton is not detectable at room temperature. This indicates a proton delocalization which could lead to disappearance of the NMR signal caused by exchange processes. The underlying dynamic process may be revealed by employing ^{15}N-^{1}H correlation experiments at varying temperature. This potentially provides insight into the proton relocation process at this site in BR.

The study performed in chapter 6 opened up the possibility to apply DNP-enhanced solid-state MAS NMR to channelrhodopsin. A number of open structure-related questions can now be addressed. Firstly, structural changes between the closed and open states in the inner gate (residues Y109, E121, E122, H173, H304 and R307) should be investigated. This could be achieved by using amino acid selective labeled and deuterated C1C2 samples. To facilitate measurements of the open state, a slow cycling variant of the iC++ channelrhodopsin could be useful (225). Secondly, the hydrogen bond network in the access channel (E129, K132, E136 and E140) needs to be investigated further, again by observing changes between the closed and open states. In such a study, the above-mentioned fast MAS probe might prove useful since it allows proton detection at low temperatures. Thirdly, the role of D195 and C167

(DC gate) in proton transport is still under debate; potentially these two residues are mainly relevant to ensure α-helix stability (226). This could be studied by using fully protonated, unlabeled protein and uniformly ^{13}C-labeled retinal and by comparing the influence on retinal chemical shifts in C1C2 wildtype, C1C2 D195N and C1C2 C167V. If a mutation-induced change in retinal chemical shifts can be observed, it is very likely that these residues are involved in the molecular action of ChR, i.e. proton and cation conductance.

In a method development oriented project line, it would be still interesting to further optimize the DNP performance towards room temperature. A possible approach could be to test new agents for creating a glassy matrix in the sample at temperatures above 200 K, which needs to be elucidated systematically. A good starting point could be trehalose, a cryo-protectant used in nature, for example by tardigrades (*Milnesium tardigradum*). However, its unique feature is under debate as it has been shown recently that intrinsically disordered proteins are involved in maintenance of vitrified state conditions, providing a general desiccation tolerance to these animals (227-229). In addition, further efforts have to be undertaken to make DNP more efficient at higher magnetic fields, e.g. 800 MHz, to profit from increase in spectral resolution (230, 231). This requires the design of new radicals that are suitable for this magnetic field.

Towards future protonation dynamics investigations, chapter 4 provides a perspective to study new protein classes by MAS NMR. In principle, proteins of any size and physical state can be targeted with the introduced approach, as long as they are large enough to be sedimented by ultracentrifugation. However, the presented case of $FcRn_{ECD}$ is probably rather favorable since the spectra quality indicates that the protein is a well-behaving rigid system. More dynamic proteins may not yield such well-resolved spectra and detailed studies may therefore be difficult. Still, the possibility to study fully protonated proteins by proton detection at 100 kHz MAS is certainly very promising in the context of protonation dynamics as it makes new proteins accessible. Assuming proton-detected spectra are fully resolved, all protons in the protein can be studied with this approach. In particular, large soluble proteins such as phytochrome photoreceptors could be investigated with 100 kHz MAS NMR upon sedimentation by ultracentrifugation.

Another prospect is the use of solution-state NMR. In fact, an investigation was started already on the photosystem II-related PsbO protein (232-235). Its crystal structure

determined at 100 K revealed a number of water molecules and carboxylate clusters at the surface, which are discussed as possible proton antenna for photosystem II (236). In this context, the pKa values of these carboxylates are highly relevant. Using solution-state NMR and pH titration experiments, pKa values of carboxylates can be determined, which potentially reveals possible proton exchange pathways at the PsbO surface (236-240). Similarly, solution-state NMR may be used to investigate the side chain mobility of the functionally-relevant aspartate and glutamate residues in PsbO (241, 242). Generally, solution-state NMR may be applicable to other large proteins, e.g. Cph1Δ2, through methyl labeling approaches and the use of the methyl-TROSY technique (104, 115, 117, 243, 244). This might prove useful in resolving the issue of the proposed PHY domain movement during the phytochrome photocycle. As mentioned above, cryo-EM and EPR would be additional suitable methods for this question and could be combined with NMR (45).

BIBLIOGRAPHY

This list contains references for chapter 1 (Introduction) and chapter 9 (General Discussion and Conclusion). The chapters 2 – 8 have individual bibliographies.

1. Ziarek JJ, Baptista D, Wagner G (2018) Recent developments in solution nuclear magnetic resonance (NMR)-based molecular biology. *Journal of Molecular Medicine* 96(1):1–8.

2. Cuniasse P, Tavares P, Orlova EV, Zinn-Justin S (2017) Structures of biomolecular complexes by combination of NMR and cryoEM methods. *Curr Opin Struct Biol* 43:104–113.

3. Quinn CM, Polenova T (2017) Structural Biology of Supramolecular Assemblies by Magic Angle Spinning NMR Spectroscopy. *Quart Rev Biophys* 50:e1.

4. Vénien-Bryan C, Li Z, Vuillard L, Boutin JA (2017) Cryo-electron microscopy and X-ray crystallography: complementary approaches to structural biology and drug discovery. *Acta Crystallographica Section F* 73(4):174–183.

5. Orlov I, et al. (2016) The integrative role of cryo electron microscopy in molecular and cellular structural biology. *Biol Cell* 109(2):81–93.

6. Kendrew JC, et al. (1958) A Three-Dimensional Model of the Myoglobin Molecule Obtained by X-Ray Analysis. *Nature* 181:662–666.

7. Bonomi M, Heller GT, Camilloni C, Vendruscolo M (2017) Principles of protein structural ensemble determination. *Curr Opin Struct Biol* 42:106–116.

8. Shoemaker SC, Ando N (2018) X-rays in the Cryo-Electron Microscopy Era: Structural Biology's Dynamic Future. *Biochemistry* 57(3):277–285.

9. Borgia A, et al. (2018) Extreme disorder in an ultrahigh-affinity protein complex. *Nature* 555:61–66.

10. Karplus M, Kuriyan J (2005) Molecular dynamics and protein function. *Proc Natl Acad Sci USA* 102(19):6679–6685.

11. Wright PE, Dyson HJ (2015) Intrinsically Disordered Proteins in Cellular Signaling and Regulation. *Nat Rev Mol Cell Biol* 16(1):18–29.

12. Murray DT, et al. (2017) Structure of FUS Protein Fibrils and Its Relevance to Self-Assembly and Phase Separation of Low- Complexity Domains. *Cell* 171(3):615–620.

13. Babu M, Forman-Kay J, Kriwacki RW (2018) Illuminating the Dark Proteome. *Cell* 166(5):1074–1077.

14. Qin S, Zhou H-X (2017) Protein folding, binding, and droplet formation in cell-like conditions. *Curr Opin Struct Biol* 43:28–37.

15. Larson AG, et al. (2017) Liquid droplet formation by HP1. *Nature* 547(7662):236–240.

16. Mitrea DM, Kriwacki RW (2016) Phase separation in biology; functional organization of a higher order. *Cell Communication and Signaling* 14:1–20.

17. Beck M, Hurt E (2017) The nuclear pore complex: understanding its function through structural insight. *Nat Rev Mol Cell Biol* 18:73–89.

18. Plitzko JM, Schuler B, Selenko P (2017) Structural Biology outside the box—inside the cell. *Curr Opin Struct Biol* 46:110–121.

19. Freedberg DI, Selenko P (2014) Live cell NMR. *Annu Rev Biophys* 43:171–192.

20. Watson JD, Crick FHC (1953) Molecular Structure of Nucleic Acids: A Structure for Deoxyribose Nucleic Acid. *Nature* 171:737–738.

21. Loll B, Kern J, Saenger W, Zouni A, Biesiadka J (2005) Towards complete cofactor arrangement in the 3.0 Å resolution structure of photosystem II. *Nature* 438(7070):1040–1044.

22. Cramer P, et al. (2000) Architecture of RNA Polymerase II and Implications for the Transcription Mechanism. *Science* 288(5466):640–649.

23. Anfinsen CB (1972) The formation and stabilization of protein structure. *Biochem J* 128(4):737–749.

24. Jackson RJ, Hellen CUT, Pestova TV (2010) The mechanism of eukaryotic translation initiation and principles of its regulation. *Nat Rev Mol Cell Biol* 10:113–127.

25. Masai H, Matsumoto S, You Z, Yoshizawa-Sugata N, Oda M (2010) Eukaryotic Chromosome DNA Replication: Where, When, and How? *Annu Rev Biochem* 79(1):89–130.

26. Koshland DE (1958) Application of a Theory of Enzyme Specificity to Protein Synthesis. *Proc Natl Acad Sci USA* 44(2):98.

27. Fischer E (1894) Einfluss der Configuration auf die Wirkung der Enzyme. *Berichte der deutschen chemischen Gesellschaft* 27(3):2985–2993.

28. Benkovic SJ, Hammes-Schiffer S (2003) A Perspective on Enzyme Catalysis. *Science* 301(5637):1196–1202.

29. Murray JE, Laurieri N, Delgoda R (2017) Chapter 24 - Proteins. *Pharmacognosy (Academic Press, Boston)* pp 477–494.

30. Keskin O, Tuncbag N, Gursoy A (2016) Predicting Protein–Protein Interactions from the Molecular to the Proteome Level. *Chem Rev* 116(8):4884–4909.

31. Janin J, Bahadur RP, Chakrabarti P (2008) Protein–protein interaction and quaternary structure. *Quart Rev Biophys* 41(2):133–180.

32. Joyce AP, Zhang C, Bradley P, Havranek JJ (2015) Structure-based modeling of protein: DNA specificity. *Briefings in Functional Genomics* 14(1):39–49.

33. Re A, Kulberkyte E, Joshi T, Workman CT (2014) RNA–Protein Interactions: An Overview. *RNA Sequence, Structure, and Function: Computational and Bioinformatic Methods* pp 491–521.

34. Lee AG (2003) Lipid–protein interactions in biological membranes: a structural perspective. *Biochimica et Biophysica Acta (BBA) - Biomembranes* 1612(1):1–40.

35. Dobson CM (2003) Protein folding and misfolding. *Nature* 426(6968):884–890.

36. Rayment I, et al. (1993) Structure of the actin-myosin complex and its implications for muscle contraction. *Science* 261(5117):58–65.

37. Prabakaran S, Lippens G, Steen H, Gunawardena J (2012) Post-translational modification: nature's escape from genetic imprisonment and the basis for dynamic information encoding. *Wiley interdisciplinary reviews Systems biology and medicine* 4(6):565–583.

38. Mahadevi AS, Sastry GN (2016) Cooperativity in Noncovalent Interactions. *Chem Rev* 116(5):2775–2825.

39. Pace CN, et al. (2014) Contribution of hydrogen bonds to protein stability. *Protein Science* 23(5):652–661.

40. Jeffrey GA (1997) An Introduction to Hydrogen Bonding.

41. Englander SW, Kallenbach NR (1983) Hydrogen exchange and structural dynamics of proteins and nucleic acids. *Quart Rev Biophys* 16(4):521–655.

42. Englander SW, Sosnick TR, Englander JJ, Mayne L (1996) Mechanisms and uses of hydrogen exchange. *Curr Opin Struct Biol* 6(1):18–23.

43. Gerwert K, Freier E, Wolf S (2014) The role of protein-bound water molecules in microbial rhodopsins. *BBA - Bioenergetics* 1837(5):606–613.

44. Velazquez Escobar F, et al. (2017) Protonation-Dependent Structural Heterogeneity in the Chromophore Binding Site of Cyanobacterial Phytochrome Cph1. *J Phys Chem B* 121(1):47–57.

45. Takala H, et al. (2014) Signal amplification and transduction in phytochrome photosensors. *Nature* 509(7499):245–248.

46. Velazquez Escobar F, et al. (2015) Conformational heterogeneity of the Pfr chromophore in plant and cyanobacterial phytochromes. *Front Mol Biosci* 2(37):1–13.

47. Johnson MP (2016) Photosynthesis. *Essays Biochem* 60(3):255–273.

48. Oesterhelt D, Schuhmann L (1974) Reconstitution of bacteriorhodopsin. *FEBS Letters* 44(3):262–265.

49. Ehrenberg B, Lewis A, Porta TK, Nagle JF, Stoeckenius W (1980) Exchange kinetics of the Schiff base proton in bacteriorhodopsin. *Proc Natl Acad Sci USA* 77(11):6571–6573.

50. Braiman M, Mathies R (1980) Resonance Raman evidence for an all-trans to 13-cis isomerization in the proton-pumping cycle of bacteriorhodopsin. *Biochemistry* 19(23):5421–5428.

51. Harbison GS, et al. (1984) Dark-adapted bacteriorhodopsin contains 13-cis, 15-syn and all-trans, 15-anti retinal Schiff bases. *Proc Natl Acad Sci USA* 81(6):1706–1709.

52. Eisenstein L, et al. (1987) FTIR difference studies on apoproteins. Protonation states of aspartic and glutamic acid residues during the photocycle of bacteriorhodopsin. *J Am Chem Soc* 109(22):6860–6862.

53. Luecke H, Schobert B, Richter HT, Cartailler JP, Lanyi JK (1999) Structure of bacteriorhodopsin at 1.55 A resolution. *Journal of Molecular Biology* 291(4):899–911.

54. Kandori H (2000) Role of internal water molecules in bacteriorhodopsin. *Biochim Biophys Acta* 1460(1):177–191.

55. Lanyi JK (2004) Bacteriorhodopsin. *Annu Rev Physiol* 66(1):665–688.

56. Neutze R, et al. (2002) Bacteriorhodopsin: a high-resolution structural view of vectorial proton transport. *Biochim Biophys Acta* 1565(2):144–167.

57. Henderson R, et al. (1990) Model for the structure of bacteriorhodopsin based on high-resolution electron cryo-microscopy. *Journal of Molecular Biology* 213(4):899–929.

58. Subramaniam S, Henderson R (2000) Molecular mechanism of vectorial proton translocation by bacteriorhodopsin. *Nature* 406:653–657.

59. Kühlbrandt W (2000) Bacteriorhodopsin–the movie. *Nature* 406(6796):569–570.

60. Lanyi JK (1997) Mechanism of ion transport across membranes. Bacteriorhodopsin as a prototype for proton pumps. *J Biol Chem* 272(50):31209–31212.

61. Luecke H, Schobert B, Richter HT, Cartailler JP, Lanyi JK (1999) Structural changes in bacteriorhodopsin during ion transport at 2 angstrom resolution. *Science* 286(5438):255–261.

62. Luecke H (2000) Atomic resolution structures of bacteriorhodopsin photocycle intermediates: the role of discrete water molecules in the function of this light-driven ion pump. *Biochim Biophys Acta* 1460(1):133–156.

63. Nango E, et al. (2016) A three-dimensional movie of structural changes in bacteriorhodopsin. *Science* 354(6319):1552–1557.

64. Freier E, Wolf S, Gerwert K (2011) Proton transfer via a transient linear water-molecule chain in a membrane protein. *Proc Natl Acad Sci USA* 108(28):11435–11439.

65. Song C, et al. (2011) Two ground state isoforms and a chromophore D-ring photoflip triggering extensive intramolecular changes in a canonical phytochrome. *Proc Natl Acad Sci USA* 108(10):3842–3847.

66. Mroginski MA, et al. (2009) Chromophore Structure of Cyanobacterial Phytochrome Cph1 in the Pr State: Reconciling Structural and Spectroscopic Data by QM/MM Calculations. *Biophysj* 96(10):4153–4163.

67. Rohmer T, et al. (2008) Light-induced chromophore activity and signal transduction in phytochromes observed by ^{13}C and ^{15}N magic-angle spinning NMR. *Proc Natl Acad Sci USA* 105(40):15229–15234.

68. van Thor JJ, et al. (2001) Light-induced proton release and proton uptake reactions in the cyanobacterial phytochrome Cph1. *Biochemistry* 40(38):11460–11471.

69. Stojković EA, et al. (2014) FTIR Spectroscopy Revealing Light-Dependent Refolding of the Conserved Tongue Region of Bacteriophytochrome. *J Phys Chem Lett* 5(15):2512–2515.

70. van Thor JJ, Ronayne KL, Towrie M (2007) Formation of the Early Photoproduct Lumi-R of Cyanobacterial Phytochrome Cph1 Observed by Ultrafast Mid-Infrared Spectroscopy. *J Am Chem Soc* 129(1):126–132.

71. Velazquez Escobar F, et al. (2015) A protonation-coupled feedback mechanism controls the signalling process in bathy phytochromes. *Nature chemistry* 7(5):423–430.

72. Haumann M, et al. (2005) Photosynthetic O_2 Formation Tracked by Time-Resolved X-ray Experiments. *Science* 310(5750):1019–1021.

73. Haumann M, et al. (2005) Structural and Oxidation State Changes of the Photosystem II Manganese Complex in Four Transitions of the Water Oxidation Cycle (S0 → S1, S1 → S2, S2 → S3, and S3,4 → S0) Characterized by X-ray Absorption Spectroscopy at 20 K and Room Temperature. *Biochemistry* 44(6):1894–1908.

74. Cox N, Pantazis DA, Neese F, Lubitz W (2013) Biological Water Oxidation. *Acc Chem Res* 46(7):1588–1596.

75. Garczarek F, Gerwert K (2005) Functional waters in intraprotein proton transfer monitored by FTIR difference spectroscopy. *Nature* 439(7072):109–112.

76. Becker-Baldus J, et al. (2015) Enlightening the photoactive site of channelrhodopsin-2 by DNP-enhanced solid-state NMR spectroscopy. *Proc Natl Acad Sci USA* 112(32):9896–9901.

77. Kato HE, et al. (2012) Crystal structure of the channelrhodopsin light-gated cation channel. *Nature* 482(7385):369–374.

78. Lórenz-Fonfría VA, Heberle J (2014) Channelrhodopsin unchained: Structure and mechanism of a light-gated cation channel. *BBA - Bioenergetics* 1837(5):626–642.

79. Lórenz-Fonfría VA, et al. (2013) Transient protonation changes in channelrhodopsin-2 and their relevance to channel gating. *Proc Natl Acad Sci USA* 110(14):1273–81.

80. Daldrop JO, et al. (2018) Orientation of non-spherical protonated water clusters revealed by infrared absorption dichroism. *Nat Commun* 9(1):311–318.

81. Burgie ES, Bussell AN, Walker JM, Dubiel K, Vierstra RD (2014) Crystal structure of the photosensing module from a red/far-red light-absorbing plant phytochrome. *Proc Natl Acad Sci USA* 111(28):10179–10184.

82. Yang Y, et al. (2012) Real-Time Tracking of Phytochrome's Orientational Changes During Pr Photoisomerization. *J Am Chem Soc* 134(3):1408–1411.

83. Ernst OP, et al. (2008) Photoactivation of Channelrhodopsin. *Journal of Biological Chemistry* 283(3):1637–1643.

84. Harrison C, Traynor JR (2003) The [^{35}S]GTPγS binding assay: approaches and applications in pharmacology. *Life Sciences* 74(4):489–508.

85. Bagshaw CR (2001) ATP analogues at a glance. *J Cell Sci* 114(3):459–460.

86. Liljas A, Liljas L, Piskur J, Nissen P, Kjeldgaard M (2009) Textbook of structural biology.

87. Spence JCH (2017) XFELs for structure and dynamics in biology. *IUCrJ* 4(4):322–339.

88. Kühlbrandt W (2014) Cryo-EM enters a new era. *Elife* 3:e03678.

89. Bai X-C, McMullan G, Scheres SHW (2015) How cryo-EM is revolutionizing structural biology. *Trends in Biochemical Sciences* 40(1):49–57.

90. Cressey D, Callaway E (2017) Cryo-electron microscopy wins chemistry Nobel. *Nature News* 550(7675):167.

91. Marion D (2013) An Introduction to Biological NMR Spectroscopy. *Mol Cell Proteomics* 12(11):3006–3025.

92. Theillet F-X, et al. (2016) Structural disorder of monomeric. *Nature* 530(7588):45–50.

93. Mylona A, et al. (2016) Opposing effects of Elk-1 multisite phosphorylation shape its response to ERK activation. *Science* 354(6309):233–237.

94. Selenko P, Wagner G (2006) NMR mapping of protein interactions in living cells. *Nat Methods* 3(2):80–81.

95. Jensen MR, Ruigrok RW, Blackledge M (2013) Describing intrinsically disordered proteins at atomic resolution by NMR. *Curr Opin Struct Biol* 23(3):426–435.

96. Schanda P, Forge V, Brutscher B (2007) Protein folding and unfolding studied at atomic resolution by fast two-dimensional NMR spectroscopy. *Proc Natl Acad Sci USA* 104(27):11257–11262.

97. Selenko P, et al. (2008) In situ observation of protein phosphorylation by high-resolution NMR spectroscopy. *Nat Struct Mol Biol* 15(3):321–329.

98. Kleckner IR, Foster MP (2011) An introduction to NMR-based approaches for measuring protein dynamics. *Biochim Biophys Acta* 1814(8):942–968.

99. Cohn M, Hu A (1978) Isotopic (^{18}O) shift in ^{31}P nuclear magnetic resonance applied to a study of enzyme-catalyzed phosphate—phosphate exchange and phosphate (oxygen)—water exchange reactions. *Proc Natl Acad Sci USA* 75(1):200–203.

100. Henzler-Wildman KA, et al. (2007) Intrinsic motions along an enzymatic reaction trajectory. *Nature* 450(7171):838–844.

101. Fawzi NL, Ying J, Ghirlando R, Torchia DA, Clore GM (2011) Atomic-resolution dynamics on the surface of amyloid-b protofibrils probed by solution NMR. *Nature* 480(7376):268–272.

102. Fawzi NL, Ying J, Torchia DA, Clore GM (2012) Probing exchange kinetics and atomic resolution dynamics in high-molecular-weight complexes using dark-state exchange saturation transfer NMR spectroscopy. *Nat Protoc* 7(8):1523–1533.

103. Eisenmesser EZ, et al. (2005) Intrinsic dynamics of an enzyme underlies catalysis. *Nature* 438(7064):117–121.

104. Sprangers R, Kay LE (2007) Quantitative dynamics and binding studies of the 20S proteasome by NMR. *Nature* 445(7128):618–622.

105. Fiaux J, Bertelsen EB, Horwich AL, Wuthrich K (2002) NMR analysis of a 900K GroEL–GroES complex. *Nature* 418(6894):207–211.

106. Gardiennet C, et al. (2012) A Sedimented Sample of a 59 kDa Dodecameric Helicase Yields High-Resolution Solid-State NMR Spectra. *Angew Chem Int Ed* 51(31):7855–7858.

107. Varani G, Aboul-ela F, Allain FHT (1996) NMR investigation of RNA structure. *Progress in Nuclear Magnetic Resonance Spectroscopy* 29(1):51–127.

108. Varani L, et al. (2000) The NMR structure of the 38 kDa U1A protein–PIE RNA complex reveals the basis of cooperativity in regulation of polyadenylation by human U1A protein. *Nat Struct Mol Biol* 7(4):329–335.

109. Asami S, Rakwalska-Bange M, Carlomagno T, Reif B (2013) Protein-RNA interfaces probed by 1H-detected MAS solid-state NMR spectroscopy. *Angew Chem Int Ed Engl* 52(8):2345–2349.

110. Amarasinghe GK, et al. (2000) NMR structure of the HIV-1 nucleocapsid protein bound to stem-loop SL2 of the Ψ-RNA packaging signal. Implications for genome recognition 1. *Journal of Molecular Biology* 301(2):491–511.

111. Wemmer DE, Chou SH, Hare DR, Reid BR (1985) Duplex-hairpin transitions in DNA: NMR studies on CGCGTATACGCG. *Nucleic Acids Res* 13(10):3755–3772.

112. Marius Clore G, Gronenborn AM (1994) Structures of larger proteins, protein-ligand and protein-DNA complexes by multi-dimensional heteronuclear NMR. *Progress in Biophysics and Molecular Biology* 62(2):153–184.

113. Wright PE, Dyson HJ (2009) Linking folding and binding. *Curr Opin Struct Biol* 19(1):31–38.

114. Dedmon MM, Lindorff-Larsen K, Christodoulou J, Vendruscolo M, Dobson CM (2005) Mapping Long-Range Interactions in α-Synuclein using Spin-Label NMR and Ensemble Molecular Dynamics Simulations. *J Am Chem Soc* 127(2):476–477.

115. Tugarinov V, Kanelis V, Kay LE (2006) Isotope labeling strategies for the study of high-molecular-weight proteins by solution NMR spectroscopy. *Nat Protoc* 1(2):749–754.

116. Pervushin K, Riek R, Wider G, Wüthrich K (1997) Attenuated T2 relaxation by mutual cancellation of dipole-dipole coupling and chemical shift anisotropy indicates an avenue to NMR structures of very large biological macromolecules in solution. *Proc Natl Acad Sci USA* 94(23):12366–12371.

117. Ollerenshaw JE, Tugarinov V, Kay LE (2003) Methyl TROSY: explanation and experimental verification. *Magn Reson Chem* 41(10):843–852.

118. Retel JS, et al. (2017) Structure of outer membrane protein G in lipid bilayers. *Nat Commun* 8(2073):1–10.

119. Petkova AT, et al. (2002) A structural model for Alzheimer's beta -amyloid fibrils based on experimental constraints from solid state NMR. *Proc Natl Acad Sci USA* 99(26):16742–16747.

120. Castellani F, et al. (2002) Structure of a protein determined by solid-state magic-angle-spinning NMR spectroscopy. *Nature* 420(6911):98–102.

121. Loquet A, et al. (2013) Atomic model of the type III secretion system needle. *Nature* 486(7402):276–279.

122. Wasmer C, et al. (2008) Amyloid fibrils of the HET-s(218-289) prion form a beta solenoid with a triangular hydrophobic core. *Science* 319(5869):1523–1526.

123. Frederick KK, et al. (2015) Sensitivity-Enhanced NMR Reveals Alterations in Protein Structure by Cellular Milieus. *Cell* 163(3):620–628.

124. Kaplan M, et al. (2015) Probing a cell-embedded megadalton protein complex by DNP-supported solid-state NMR. *Nat Methods* 12(7):649–654.

125. Lange S, et al. (2016) Structural analysis of a signal peptide inside the ribosome tunnel by DNP MAS NMR. *Science Advances* 2(8):e1600379–e1600379.

126. Agarwal V, et al. (2014) De Novo 3D Structure Determination from Sub-milligram Protein Samples by Solid-State 100 kHz MAS NMR Spectroscopy. *Angew Chem Int Ed Engl* 53(45):12253–12256.

127. Linser R, et al. (2011) Proton-detected solid-state NMR spectroscopy of fibrillar and membrane proteins. *Angew Chem Int Ed Engl* 50(19):4508–4512.

128. Bersch B, Dörr JM, Hessel A, Killian JA, Schanda P (2017) Proton-Detected Solid-State NMR Spectroscopy of a Zinc Diffusion Facilitator Protein in Native Nanodiscs. *Angew Chem Int Ed Engl* 56(9):2508–2512.

129. Levitt MH (2013) *Spin Dynamics* (John Wiley & Sons).

130. Keeler J (2011) Understanding NMR spectroscopy.

131. Duer MJ (2005) Introduction to solid-state NMR spectroscopy.

132. Laws DD, Bitter H-ML, Jerschow A (2002) Solid-state NMR spectroscopic methods in chemistry. *Angew Chem Int Ed Engl* 41(17):3096–3129.

133. Aue WP, Bartholdi E, Ernst RR (1976) Two-dimensional spectroscopy. Application to nuclear magnetic resonance. *J Chem Phys* 64(5):2229–2246.

134. Pines A (1972) Proton-Enhanced Nuclear Induction Spectroscopy. A Method for High Resolution NMR of Dilute Spins in Solids. *J Chem Phys* 56(4):1776–1777.

135. Hartmann SR, Hahn EL (1962) Nuclear double resonance in the rotating frame. *Phys Rev* 128(5):2042–2053.

136. Verardi R, Traaseth NJ, Masterson LR, Vostrikov VV, Veglia G (2012) Isotope Labeling for Solution and Solid-State NMR Spectroscopy of Membrane Proteins. *Advances in Experimental Medicine and Biology* 992:35–62.

137. LeMaster DM, Kushlan DM (1996) Dynamical Mapping of E. coliThioredoxin via ^{13}C NMR Relaxation Analysis. *J Am Chem Soc* 118(39):9255–9264.

138. Hong M, Jakes K (1999) Selective and extensive ^{13}C labeling of a membrane protein for solid-state NMR investigations. *J Biomol NMR* 14(1):71–74.

139. Higman VA, et al. (2009) Assigning large proteins in the solid state: a MAS NMR resonance assignment strategy using selectively and extensively ^{13}C-labelled proteins. *J Biomol NMR* 44(4):245–260.

140. Slichter CP (2014) The discovery and renaissance of dynamic nuclear polarization. *Reports on Progress in Physics* 77(7):1–15.

141. Carver TR, Slichter CP (1956) Experimental Verification of the Overhauser Nuclear Polarization Effect. *Phys Rev* 102(4):975–980.

142. Becerra LR, Gerfen GJ, Temkin RJ, Singel DJ, Griffin RG (1993) Dynamic nuclear polarization with a cyclotron resonance maser at 5 T. *Phys Rev Lett* 71(21):3561–3564.

143. Becerra LR, et al. (1995) A Spectrometer for Dynamic Nuclear Polarization and Electron Paramagnetic Resonance at High Frequencies. *Journal of Magnetic Resonance, Series A* 117(1):28–40.

144. Griffin RG (2011) Dynamic nuclear polarization at 9T using a novel 250 Gyrotron microwave source. *Journal of Magnetic Resonance* 213(2):410–412.

145. Kaplan M, et al. (2016) EGFR Dynamics Change during Activation in Native Membranes as Revealed by NMR. *Cell* 167(5):1241–1251.

146. Barnes AB, et al. (2008) High-Field Dynamic Nuclear Polarization for Solid and Solution Biological NMR. *Appl Magn Reson* 34(3-4):237–263.

147. Bajaj VS, Mak-Jurkauskas ML, Belenky M, Herzfeld J, Griffin RG (2009) Functional and shunt states of bacteriorhodopsin resolved by 250 GHz dynamic nuclear polarization-enhanced solid-state NMR. *Proc Natl Acad Sci USA* 106(23):9244–9249.

148. Akbey U, Oschkinat H (2016) Structural biology applications of solid state MAS DNP NMR. *Journal of Magnetic Resonance* 269:213–224.

149. Linden AH, et al. (2011) Neurotoxin II bound to acetylcholine receptors in native membranes studied by dynamic nuclear polarization NMR. *J Am Chem Soc* 133(48):19266–19269.

150. Jacso T, et al. (2012) Characterization of membrane proteins in isolated native cellular membranes by dynamic nuclear polarization solid-state NMR spectroscopy without purification and reconstitution. *Angew Chem Int Ed Engl* 51(2):432–435.

151. Mak-Jurkauskas ML, et al. (2008) Energy transformations early in the bacteriorhodopsin photocycle revealed by DNP-enhanced solid-state NMR. *Proc Natl Acad Sci USA* 105(3):883–888.

152. Märker K, et al. (2015) A New Tool for NMR Crystallography: Complete $^{13}C/^{15}N$ Assignment of Organic Molecules at Natural Isotopic Abundance Using DNP-Enhanced Solid-State NMR. *J Am Chem Soc* 137(43):13796–13799.

153. Thankamony ASL, Wittmann JJ, Kaushik M, Corzilius B (2017) Progress in Nuclear Magnetic Resonance Spectroscopy. *Progress in Nuclear Magnetic Resonance Spectroscopy* 102-103:120–195.

154. Song C, Hu K-N, Joo C-G, Swager TM, Griffin RG (2006) TOTAPOL: A Biradical Polarizing Agent for Dynamic Nuclear Polarization Experiments in Aqueous Media. *J Am Chem Soc* 128(35):11385–11390.

155. Sauvée C, et al. (2013) Highly efficient, water-soluble polarizing agents for dynamic nuclear polarization at high frequency. *Angew Chem Int Ed Engl* 52(41):10858–10861.

156. Akbey U, et al. (2010) Dynamic nuclear polarization of deuterated proteins. *Angew Chem Int Ed Engl* 49(42):7803–7806.

157. Lee D, Hediger S, De Paëpe G (2015) Is solid-state NMR enhanced by dynamic nuclear polarization? *Solid State Nuclear Magnetic Resonance* 66-67:6–20.

158. Mentink-Vigier F, et al. (2015) Nuclear depolarization and absolute sensitivity in magic-angle spinning cross effect dynamic nuclear polarization. *Phys Chem Chem Phys* 17(34):21824–21836.

159. Akbey U, Linden AH, Oschkinat H (2012) High-Temperature Dynamic Nuclear Polarization Enhanced Magic-Angle-Spinning NMR. *Appl Magn Reson* 43(1-2):81–90.

160. Lelli M, et al. (2015) Solid-State Dynamic Nuclear Polarization at 9.4 and 18.8 T from 100 K to Room Temperature. *J Am Chem Soc* 137(46):14558–14561.

161. Linden AH, et al. (2011) Cryogenic temperature effects and resolution upon slow cooling of protein preparations in solid state NMR. *J Biomol NMR* 51(3):283–292.

162. Mentink-Vigier F, Akbey U, Oschkinat H, Vega S, Feintuch A (2015) Journal of Magnetic Resonance. *Journal of Magnetic Resonance* 258(C):102–120.

163. Reif B (2012) Ultra-high resolution in MAS solid-state NMR of perdeuterated proteins: Implications for structure and dynamics. *Journal of Magnetic Resonance* 216:1–12.

164. Akbey U, et al. (2010) Optimum levels of exchangeable protons in perdeuterated proteins for proton detection in MAS solid-state NMR spectroscopy. *J Biomol NMR* 46(1):67–73.

165. Chevelkov V, Rehbein K, Diehl A, Reif B (2006) Ultrahigh resolution in proton solid-state NMR spectroscopy at high levels of deuteration. *Angew Chem Int Ed Engl* 45(23):3878–3881.

166. Zhou DH, et al. (2007) Proton-Detected Solid-State NMR Spectroscopy of Fully Protonated Proteins at 40 kHz Magic-Angle Spinning. *J Am Chem Soc* 129(38):11791–11801.

167. Zhou DH, et al. (2007) Solid-State Protein-Structure Determination with Proton-Detected Triple-Resonance 3D Magic-Angle-Spinning NMR Spectroscopy. *Angew Chem Int Ed* 46(44):8380–8383.

168. Böckmann A, Ernst M, Meier BH (2015) Spinning proteins, the faster, the better? *J Magn Reson* 253:71–79.

169. Chevelkov V, et al. (2003) ^{1}H detection in MAS solid-state NMR spectroscopy of biomacromolecules employing pulsed field gradients for residual solvent suppression. *J Am Chem Soc* 125(26):7788–7789.

170. Barbet-Massin E, et al. (2014) Rapid Proton-Detected NMR Assignment for Proteins with Fast Magic Angle Spinning. *J Am Chem Soc* 136(35):12489–12497.

171. Knight MJ, et al. (2011) Fast Resonance Assignment and Fold Determination of Human Superoxide Dismutase by High-Resolution Proton-Detected Solid-State MAS NMR Spectroscopy. 50(49):11697–11701.

172. Barbet-Massin E, Huang C-T, Daebel V, Hsu S-TD, Reif B (2015) Site-specific solid-state NMR studies of "trigger factor" in complex with the large ribosomal subunit 50S. *Angew Chem Int Ed Engl* 54(14):4367–4369.

173. Beeby M, Bobik TA, Yeates TO (2014) Atomic Model of a Cell-Wall Cross-Linking Enzyme in Complex with an Intact Bacterial Peptidoglycan. *J Am Chem Soc* 136(51):17852–17860.

174. Zhou DH, et al. (2012) Solid-state NMR analysis of membrane proteins and protein aggregates by proton detected spectroscopy. *J Biomol NMR* 54(3):291–305.

175. Tang M, Comellas G, Rienstra CM (2013) Advanced solid-state NMR approaches for structure determination of membrane proteins and amyloid fibrils. *Acc Chem Res* 46(9):2080–2088.

176. Andreas LB, et al. (2016) Structure of fully protonated proteins by proton-detected magic-angle spinning NMR. *Proc Natl Acad Sci USA* 113(33):9187–9192.

177. Struppe J, et al. (2017) Expanding the horizons for structural analysis of fully protonated protein assemblies by NMR spectroscopy at MAS frequencies above 100 kHz. *Solid State Nuclear Magnetic Resonance* 87:117–125.

178. Jan S, et al. (2016) NMR Spectroscopic Assignment of Backbone and Side-Chain Protons in Fully Protonated Proteins: Microcrystals, Sedimented Assemblies, and Amyloid Fibrils. *Angew Chem Int Ed* 55(50):15504–15509.

179. Penzel S, et al. (2015) Protein resonance assignment at MAS frequencies approaching 100 kHz: a quantitative comparison of J-coupling and dipolar-coupling-based transfer methods. *J Biomol NMR* 63(2):165–186.

180. Lalli D, et al. (2017) Proton-Based Structural Analysis of a Heptahelical Transmembrane Protein in Lipid Bilayers. *J Am Chem Soc* 139(37):13006–13012.

181. Xue K, et al. (2017) Limits of Resolution and Sensitivity of Proton Detected MAS Solid-State NMR Experiments at 111 kHz in Deuterated and Protonated Proteins. *Sci Rep* 7(7444):1–7.

182. Linser R, Fink U, Reif B (2008) Proton-detected scalar coupling based assignment strategies in MAS solid-state NMR spectroscopy applied to perdeuterated proteins. *Journal of Magnetic Resonance* 193(1):89–93.

183. Morris GA, Freeman R (1979) Enhancement of nuclear magnetic resonance signals by polarization transfer. *J Am Chem Soc* 101(3):760–762.

184. Barbet-Massin E, et al. (2013) Out-and-back ^{13}C–^{13}C scalar transfers in protein resonance assignment by proton-detected solid-state NMR under ultra-fast MAS. *J Biomol NMR* 56(4):379–386.

185. Fricke P, et al. (2016) Backbone assignment of perdeuterated proteins by solid-state NMR using proton detection and ultrafast magic-angle spinning. *Nat Protoc* 12(4):764–782.

186. Daviso E, Eddy MT, Andreas LB, Griffin RG, Herzfeld J (2013) Efficient resonance assignment of proteins in MAS NMR by simultaneous intra- and inter-residue 3D correlation spectroscopy. *J Biomol NMR* 55(3):257–265.

187. Sperling LJ, Berthold DA, Sasser TL, Jeisy-Scott V, Rienstra CM (2010) Assignment Strategies for Large Proteins by Magic-Angle Spinning NMR: The 21-kDa Disulfide-Bond-Forming Enzyme DsbA. *Journal of Molecular Biology* 399(2):268–282.

188. Böckmann A (2008) 3D Protein Structures by Solid-State NMR Spectroscopy: Ready for High Resolution. *Angew Chem Int Ed* 47(33):6110–6113.

189. Takegoshi K, Nakamura S, Terao T (2003) ^{13}C–^{1}H dipolar-driven ^{13}C–^{13}C recoupling without ^{13}C rf irradiation in nuclear magnetic resonance of rotating solids. *J Chem Phys* 118(5):2325–2341.

190. Takegoshi K, Nakamura S, Terao T (2001) ^{13}C–^{1}H dipolar-assisted rotational resonance in magic-angle spinning NMR. *Chemical Physics Letters* 344(5):631–637.

191. Renault M, Cukkemane A, Baldus M (2010) Solid-state NMR spectroscopy on complex biomolecules. *Angew Chem Int Ed Engl* 49(45):8346–8357.

192. Szeverenyi NM, Sullivan MJ, Maciel GE (1982) Observation of spin exchange by two-dimensional Fourier transform ^{13}C cross polarization-magic-angle spinning. *Journal of Magnetic Resonance (1969)* 47(3):462–475.

193. Jain MG, et al. (2017) Selective ^{1}H–^{1}H Distance Restraints in Fully Protonated Proteins by Very Fast Magic-Angle Spinning Solid-State NMR. *J Phys Chem Lett* 8(11):2399–2405.

194. Hardy EH, Detken A, Meier BH (2003) Fast-MAS total through-bond correlation spectroscopy using adiabatic pulses. *Journal of Magnetic Resonance* 165(2):208–218.

195. Nagel G, et al. (2002) Channelrhodopsin-1: a light-gated proton channel in green algae. *Science* 296(5577):2395–2398.

196. Nagel G, et al. (2003) Channelrhodopsin-2, a directly light-gated cation-selective membrane channel. *Proc Natl Acad Sci USA* 100(24):13940–13945.

197. Boyden ES, Zhang F, Bamberg E, Nagel G, Deisseroth K (2005) Millisecond-timescale, genetically targeted optical control of neural activity. *Nat Neurosci* 8(9):1263–1268.

198. Hegemann P, Möglich A (2010) Channelrhodopsin engineering and exploration of new optogenetic tools. *Nat Methods* 8(1):39–42.

199. Hegemann P, Nagel G (2013) From channelrhodopsins to optogenetics. *EMBO Mol Med* 5(2):173–176.

200. Britt JP, McDevitt RA, Bonci A (2012) Use of channelrhodopsin for activation of CNS neurons. *Current protocols in neuroscience* 58(1):1–19.

201. Rohmer T, et al. (2006) ^{15}N MAS NMR studies of cph1 phytochrome: Chromophore dynamics and intramolecular signal transduction. *J Phys Chem B* 110(41):20580–20585.

202. Song C, et al. (2011) Exploring Chromophore-Binding Pocket: High-Resolution Solid-State ^{1}H–^{13}C Interfacial Correlation NMR Spectra with Windowed PMLG Scheme. *Appl Magn Reson* 42(1):79–88.

203. Song C, Essen L-O, Gärtner W, Hughes J, Matysik J (2012) Solid-State NMR Spectroscopic Study of Chromophore–Protein Interactions in the Pr Ground State of Plant Phytochrome A. *Molecular Plant* 5(3):698–715.

204. Hahn J, Strauss HM, Schmieder P (2008) Heteronuclear NMR Investigation on the Structure and Dynamics of the Chromophore Binding Pocket of the Cyanobacterial Phytochrome Cph1. *J Am Chem Soc* 130(33):11170–11178.

205. Janina H, Ronald K, Peter S (2007) Solution-State ^{15}N NMR Spectroscopic Study of α-C-Phycocyanin: Implications for the Structure of the Chromophore-Binding Pocket of the Cyanobacterial Phytochrome Cph1. *Chembiochem* 8(18):2249–2255.

206. Strauss HM, Hughes J, Schmieder P (2005) Heteronuclear solution-state NMR studies of the chromophore in cyanobacterial phytochrome Cph1. *Biochemistry* 44(23):8244–8250.

207. Röben M, et al. (2010) NMR spectroscopic investigation of mobility and hydrogen bonding of the chromophore in the binding pocket of phytochrome proteins. *Chemphyschem* 11(6):1248–1257.

208. Ward ME, et al. (2011) Proton-Detected Solid-State NMR Reveals Intramembrane Polar Networks in a Seven-Helical Transmembrane Protein Proteorhodopsin. *J Am Chem Soc* 133(43):17434–17443.

209. Wang S, Shi L, Kawamura I, Brown LS, Ladizhansky V (2011) Site-specific solid-state NMR detection of hydrogen-deuterium exchange reveals conformational changes in a 7-helical transmembrane protein. *Biophys J* 101(3):23–5.

210. Nack M, Radu I, Bamann C, Bamberg E, Heberle J (2009) The retinal structure of channelrhodopsin2 assessed by resonance Raman spectroscopy. *FEBS Letters* 583(22):3676–3680.

211. Stehfest K, Ritter E, Berndt A, Bartl F, Hegemann P (2010) The branched photocycle of the slow-cycling channelrhodopsin-2 mutant C128T. *Journal of Molecular Biology* 398(5):690–702.

212. Ritter E, Piwowarski P, Hegemann P, Bartl FJ (2013) Light-dark Adaptation of Channelrhodopsin C128T Mutant. *Journal of Biological Chemistry* 288(15):10451–10458.

213. Essen L-O, Mailliet J, Hughes J (2008) The structure of a complete phytochrome sensory module in the Pr ground state. *Proc Natl Acad Sci USA* 105(38):14709–14714.

214. Song C, et al. (2013) Solid-State NMR Spectroscopy to Probe Photoactivation in Canonical Phytochromes. *Photochem Photobiol* 89(2):259–273.

215. Song C, et al. (2014) The D-ring, not the A-ring, rotates in Synechococcus OS-B' phytochrome. *Journal of Biological Chemistry* 289(5):2552–2562.

216. Song C, et al. (2011) On the Collective Nature of Phytochrome Photoactivation. *Biochemistry* 50(51):10987–10989.

217. Burgie ES, Zhang J, Vierstra RD (2016) Crystal Structure of Deinococcus Phytochrome in the Photoactivated State Reveals a Cascade of Structural Rearrangements during Photoconversion. *Structure* 24(3):448–457.

218. Burgie ES, et al. (2014) Crystallographic and electron microscopic analyses of a bacterial phytochrome reveal local and global rearrangements during photoconversion. *Journal of Biological Chemistry* 289(35):24573–24587.

219. Mailliet J, et al. (2011) Spectroscopy and a high-resolution crystal structure of Tyr263 mutants of cyanobacterial phytochrome Cph1. *Journal of Molecular Biology* 413(1):115–127.

220. Wang H, Wang H (2015) Phytochrome signaling: time to tighten up the loose ends. *Molecular Plant* 8(4):540–551.

221. Yang X, et al. (2015) Light Signaling Mechanism of Two Tandem Bacteriophytochromes. *Structure* 23(7):1179–1189.

222. Nagano S, et al. (2016) The Crystal Structures of the N-Terminal Photosensory Core Module of Agrobacterium Phytochrome Agp1 as Parallel and Anti-Parallel Dimers. *Journal of Biological Chemistry* 291:20674–20691.

223. Yang X, Ren Z, Kuk J, Moffat K (2011) Temperature-scan cryocrystallography reveals reaction intermediates in bacteriophytochrome. *Nature* 479(7373):428–432.

224. Ni QZ, et al. (2018) Primary Transfer Step in the Light-Driven Ion Pump Bacteriorhodopsin: An Irreversible U-Turn Revealed by Dynamic Nuclear Polarization-Enhanced Magic Angle Spinning NMR. *J Am Chem Soc* 140(11):4085–4091.

225. Berndt A, et al. (2016) Structural foundations of optogenetics: Determinants of channelrhodopsin ion selectivity. *Proc Natl Acad Sci USA* 113(4):822–829.

226. Nack M, et al. (2010) The DC gate in Channelrhodopsin-2: crucial hydrogen bonding interaction between C128 and D156. *Photochemical & Photobiological Sciences* 9(2):194–198.

227. Westh P, Ramløv H (2005) Trehalose accumulation in the tardigrade Adorybiotus coronifer during anhydrobiosis. *J Exp Zool* 258(3):303–311.

228. Boothby TC, et al. (2017) Tardigrades Use Intrinsically Disordered Proteins to Survive Desiccation. *Molecular Cell* 65(6):975–984.

229. Hengherr S, Heyer AG, Köhler H-R, Schill RO (2007) Trehalose and anhydrobiosis in tardigrades - evidence for divergence in responses to dehydration. *FEBS J* 275(2):281–288.

230. Fricke P, et al. (2016) High resolution observed in 800 MHz DNP spectra of extremely rigid type III secretion needles. *J Biomol NMR* 65(3):121–126.

231. Jaudzems K, et al. (2018) Dynamic nuclear polarization enhanced biomolecular NMR spectroscopy at high magnetic field with fast magic-angle spinning. *Angew Chem Int Ed*. doi:10.1002/anie.201801016.

232. Popelkova H, Yocum CF (2011) PsbO, the manganese-stabilizing protein: Analysis of the structure–function relations that provide insights into its role in photosystem II. *Journal of Photochemistry and Photobiology B: Biology* 104(1):179–190.

233. Ifuku K, Noguchi T (2016) Structural Coupling of Extrinsic Proteins with the Oxygen-Evolving Center in Photosystem II. *Front Plant Sci* 7(84):1–11.

234. Roose JL, Wegener KM, Pakrasi HB (2007) The extrinsic proteins of Photosystem II. *Photosynth Res* 92(3):369–387.

235. Las Rivas De J, Barber J (2004) Analysis of the Structure of the PsbO Protein and its Implications. *Photosynth Res* 81(3):329–343.

236. Bommer M, Bondar A-N, Zouni A, Dobbek H, Dau H (2016) Crystallographic and Computational Analysis of the Barrel Part of the PsbO Protein of Photosystem II: Carboxylate–Water Clusters as Putative Proton Transfer Relays and Structural Switches. *Biochemistry* 55(33):4626–4635.

237. Tollinger M, Forman-Kay JD, Kay LE (2002) Measurement of Side-Chain Carboxyl pKa Values of Glutamate and Aspartate Residues in an Unfolded Protein by Multinuclear NMR Spectroscopy. *J Am Chem Soc* 124(20):5714–5717.

238. Handloser CS, Chakrabarty MR, Mosher MW (1973) Experimental determination of pKa values by use of NMR chemical shift. *J Chem Educ* 50(7):510–511.

239. Everill P, Sudmeier JL, Bachovchin WW (2012) Direct NMR Observation and pKa Determination of the Asp102 Side Chain in a Serine Protease. *J Am Chem Soc* 134(4):2348–2354.

240. Bondar A-N, Dau H (2012) Extended protein/water H-bond networks in photosynthetic water oxidation. *BBA - Bioenergetics* 1817(8):1177–1190.

241. Berjanskii MV, Wishart DS (2013) A Simple Method to Measure Protein Side-Chain Mobility Using NMR Chemical Shifts. *J Am Chem Soc* 135(39):14536–14539.

242. Hansen AL, Lundström P, Velyvis A, Kay LE (2012) Quantifying Millisecond Exchange Dynamics in Proteins by CPMG Relaxation Dispersion NMR Using Side-Chain 1H Probes. *J Am Chem Soc* 134(6):3178–3189.

243. Schuetz AK, Kay LE (2016) A Dynamic molecular basis for malfunction in disease mutants of p97/VCP. *Elife* 5. doi:10.7554/eLife.20143.

244. Religa TL, Sprangers R, Kay LE (2010) Dynamic regulation of archaeal proteasome gate opening as studied by TROSY NMR. *Science* 328(5974):98–102.

CURRICULUM VITAE

For reasons of data protection, the curriculum vitae is not included in the online version.

HONORS AND AWARDS

2018 Selected for participation and poster presentation at the 68th Lindau Nobel Laureate Meeting

2017 Prize for the best talk, FMP/MDC PhD Symposium, Schorfheide, Germany

2017 Young Scientist Award of the International Society of Magnetic Resonance

2017 Travel Scholarship, 20th Meeting of the International Society of Magnetic Resonance, Québec City, Canada

2017 Travel Scholarship, Frontiers of NMR in Life Sciences, Keystone, Colorado USA

2016 Travel Scholarship, 57th Experimental Nuclear Magnetic Resonance Conference, Pittsburgh, Pennsylvania USA

2015 Prize for the best talk, FMP/MDC PhD Symposium, Bad Saarow, Germany

2015 Travel Scholarship, 9th Alpine on Solid-state NMR, Chamonix, France

2015 Prize for the best talk, 3rd Annual SFB1078 Retreat, Goslar, Germany

2014 Diploma in Biochemistry (equivalent to Master of Science) with honors and best grades possible, Free University of Berlin, Germany

RESEARCH PRESENTATIONS

34) Poster presentation, 68th Lindau Nobel Laureate Meeting, Lindau, Germany, *June 2018*

33) **Selected Talk**, PostDoc Day 2018, Max-Delbrück Center for Molecular Medicine Berlin, Germany, *June 2018*

32) Poster presentation, 59th Experimental Nuclear Magnetic Resonance Conference, Orlando, Florida USA, *April 2018*

31) **Selected Talk** and Poster presentation, 6th Annual SFB1078 Retreat, Schloss Rauischholzhausen, Germany, *March 2018*

30) **Invited Talk**, Department of Pharmaceutical Chemistry, University of California San Francisco, USA, *November 2017*

29) **Invited Talk**, Department of Chemistry, University of Southern California, Santa Cruz, California USA, *November 2017*

28) **Invited Talk**, Department of Chemistry, Stanford University, Stanford, California USA, *November 2017*

27) **Selected Talk** and Poster presentation, 5th Annual SFB1078 Retreat, Elstal, Germany*, October 2017*

26) **Selected Talk**, FMP/MDC PhD Symposium, Schorfheide, Germany, *September 2017*

25) **Invited Talk**, Department of Biochemistry, Brandeis University, Waltham, Massachusetts USA, *August 2017*

24) **Invited Talk**, Department of Molecular and Cellular Biology, Harvard University, Cambridge, Massachusetts USA, *August 2017*

23) **Invited Talk**, Dana-Farber Cancer Institute, Harvard Medical School, Boston, Massachusetts USA, *August 2017*

22) **Invited Lecture**, Department of Biology and Chemistry, University of Giessen, Germany, *July 2017*

21) **Selected Talk** and Poster presentation, 20th Meeting of the International Society of Magnetic Resonance, Québec City, Canada, *July 2017*

20) **Invited Talk**, *Institut de Biologie et Chimie des Protéines*, University of Lyon, France, *June 2017*

19) **Invited Talk**, *Institut de Biologie Structurale*, Grenoble, France, *June 2017*

18) Poster presentation, 2nd iNEXT Annual User Meeting, Brno, Czech Republic, *May 2017*

17) **Selected Talk** and Poster presentation, Frontiers of NMR in Life Sciences, Keystone, Colorado USA, *March 2017*

16) Poster presentation, Ampere Biological Solid–state NMR School, Palma de Mallorca, Spain, *October 2016*

15) **Invited Talk**, EMBO Conference on Retinal Proteins, Potsdam, Germany, *October 2016*

14) Poster presentation, FMP/MDC PhD Symposium, Joachmisthal, Germany, *September 2016*

13) Poster presentation, 57th Experimental Nuclear Magnetic Resonance Conference, Pittsburgh, Pennsylvania USA, *April 2016*

12) Poster presentation, 4th Annual SFB1078 Retreat, Schmöckwitz, Germany, *March 2016*

11) **Invited Lecture**, SFB1078 Graduate Research Seminar, Berlin, Germany, *October 2015*

10) **Invited Talk**, 6th Joint MX-Day, Berlin, Germany, *September 2015*

9) **Selected Talk**, FMP/MDC PhD Symposium, Bad Saarow, Germany, *September 2015*

8) Poster presentation, 9th Alpine Conference on Solid–state NMR, Chamonix, France, *September 2015*

7) Poster presentation, Hyperpolarized Magnetic Resonance International DNP Symposium, Eegmond aan Zee, Netherlands, *August 2015*

6) **Selected Talk** and Poster presentation, 3rd Annual SFB1078 Retreat, Goslar, Germany, *March 2015*

5) Poster presentation, EBSA Solid–State NMR School, Munich, Germany, *November 2014*

4) Poster presentation, 36th Discussion Meeting of the GDCh Division, 'Magnetic Resonance', Berlin, Germany, *September 2014*

3) Poster presentation, EMBO Practical Course Multidimensional NMR in Structural Biology, Joachmisthal, Germany, *August 2014*

2) Poster presentation, EUROMAR, Zürich, Switzerland, *July 2014*

1) Poster presentation, 2nd Annual SFB1078 Retreat, Goslar, Germany, *March 2014*

LIST OF PUBLICATIONS

11. Lisa Gerland, **Daniel Friedrich**, Joachim Snellings, Linus Hopf, Eavan Donovan, Anne Diehl, Peter Schmieder, Holger Dau, and Hartmut Oschkinat:
'pKa measurements of carboxyl groups offer first insights into protonation dynamics of PsbO', *in preparation*

10. Andrew J. Nieuwkoop,[#] **Daniel Friedrich**,[#] and Hartmut Oschkinat:
'Exploring Long-range Contacts and Hydrogen Bonds in Proteins by Proton-detected Solid-state Magic Angle Spinning NMR', *in preparation*
[#] ***Equal contribution***

9. **Daniel Friedrich**, Andrew J. Nieuwkoop, Florian Brünig, Roland R. Netz, Peter Hegemann, and Hartmut Oschkinat:
'Direct Observation of Proton Exchange in a Proton Pump', *in preparation*

8. **Daniel Stöppler**,[#] Alex Macpherson,[#] Susanne Smith-Penzel, Nicolas Basse, Fabien Lecomte, Hervé Deboves, Richard D. Taylor, Tim Norman, John Porter, Lorna C. Waters, Marta Westwood, Ben Cossins, Katharine Cain, James White, Robert Griffin, Christine Prosser, Sebastian Kelm, Amy H. Sullivan, David Fox III, Mark D. Carr, Alistair Henry, Richard Taylor, Beat H. Meier, Hartmut Oschkinat, and Alastair Lawson:
'Insight into Small Molecule Binding to the Neonatal Fc Receptor by X-ray Crystallography and 100 kHz Magic-Angle-Spinning NMR', *PLOS Biology*, 2018, (16):5, e2006192
[#] ***Equal contribution***

7. Michel-Andreas Geiger,[#] Anil P. Jagtap,[#] Monu Kaushik,[#] Han Sun, **Daniel Stöppler**, Snorri Th. Sigurdsson, Björn Corzilius, and Hartmut Oschkinat:
'Efficiency of water-soluble nitroxide biradicals for dynamic nuclear polarization in rotating solids at 9.4 T: bcTol-M and cyolyl-TOTAPOL as new polarizing agents', *Chemistry – A European Journal*, 2018, 24(51), pp 13485–13494
[#] ***Equal contribution***

6. Anne Diehl,[#] Yvette Roske,[#] Linda Ball, Anup Chowdhury, Matthias Hiller, Noel Molière, Regina Kramer, **Daniel Stöppler**, Catherine L. Worth, Brigitte Schlegel, Martina Leidert, Nils Cremer, Natalja Erdmann, Daniel Lopez, Heike Stephanowitz, Eberhard Krause, Barth-Jan van Rossum, Peter Schmieder, Udo Heinemann, Kürşad Turgay, Ümit Akbey, and Hartmut Oschkinat:
'Structural changes of TasA in biofilm formation of *Bacillus subtilis*', *Proceedings of the National Academy of Sciences USA*, 2018, 115(13), pp 3237–3242
[#] ***Equal contribution***

5. Wolfgang Blenau, **Daniel Stöppler**, Sabine Balfanz, Markus Thamm, and Arnd Baumann:
'Dm5-HT_{2B}: Pharmacological Characterization of the Fifth Serotonin Receptor Subtype of Drosophila melanogaster', *Frontiers in Systems Neuroscience*, 2017, 11 (28), pp 1–11

4. **Daniel Stöppler**, Chen Song, Barth-Jan van Rossum, Michel-Andreas Geiger, Christina Lang, Maria-Andrea Mroginski, Anil P. Jagtap, Snorri Th. Sigurdsson, Jörg Matysik, Jon Hughes, and Hartmut Oschkinat:
'Dynamic Nuclear Polarization Provides New Insights into Chromophore Structure in Phytochrome Photoreceptors', *Angewandte Chemie International Edition*, 2016, 55 (52), pp 16017–16020

3. Michel-Andreas Geiger,[#] Marcella Orwick-Rydmark,[#] Katharina Märker, W. Trent Franks, Dmitry Akhmetzyanov, **Daniel Stöppler**, Maximilian Zinke, Edgar Specker, Marc Nazaré, Anne Diehl, Barth-Jan van Rossum, Fabien Aussenac, Thomas Prisner, Ümit Akbey, and Hartmut Oschkinat:
'Temperature dependence of cross-effect dynamic nuclear polarization in rotating solids: advantages of elevated temperatures', *Physical Chemistry Chemical Physics*, 2016, 18, pp 30696–30704
[#] ***Equal contribution***

2. Anil P. Jagtap, Michel-Andreas Geiger, **Daniel Stöppler**, Marcella Orwick-Rydmark, Hartmut Oschkinat, and Snorri Th. Sigurdsson:
'bcTol: a highly water-soluble biradical for efficient dynamic nuclear polarization of biomolecules', *Chemical Communications*, 2016, 52, pp 7020–7023

1. Sara Bruun,[#] **Daniel Stoeppler**,[#] Anke Keidel, Uwe Kuhlmann, Meike Luck, Anne Diehl, Michel-Andreas Geiger, David Woodmansee, Dirk Trauner, Peter Hegemann, Hartmut Oschkinat, Peter Hildebrandt, and Katja Stehfest:
'Light−Dark Adaptation of Channelrhodopsin Involves Photoconversion between the all-*trans* and 13-*cis* Retinal Isomers', *Biochemistry*, 2015, 54 (35), pp 5389–5400
[#] ***Equal contribution***

DECLARATION

Herewith I affirm that I have written this thesis entitled "ESTABLISHING ADVANCED MAS NMR METHODS TO INVESTIGATE PROTONATION DYNAMICS IN PROTEINS" on my own. All references to the literature are marked and listed at the end of the thesis.

The work was not submitted previously in same or similar form to another examination committee and was not yet published, unless stated in chapters 4, 5, 6, 7 and 8.

Daniel Friedrich